Experimental study on the intermittent flow phenomena in a turbulent jet and a boundary layer

TERASHIMA Osamu

Experimental study on the intermittent flow phenomena in a turbulent jet and a boundary layer
(乱流噴流と境界層における間欠的な流動現象に関する実験的研究)

by
TERASHIMA Osamu

DEPARTMENT OF MECHANICAL SCIENCE AND ENGINEERING
NAGOYA UNIVERSITY
NAGOYA, JAPAN

Contents

Nomenclature

Chapter 2

f_h	:	Frequency of Helmholtz resonance
f_o	:	Frequency of organ-pipe resonance
d_1	:	Inner diameter of conduit pipe of pressure probe
d_2	:	Diameter of space in flare of pressure probe
c_0	:	Speed of sound
l_1	:	Length of conduit pipe of pressure probe
l_2	:	Thickness of gap between surface of microphone and edge of conduit pipe
M	:	Amplitude ratio
ϕ	:	Phase difference
p_1	:	Amplitude of pressure signal of reference microphone
ϕ_1	:	Phase difference of pressure signal of reference microphone
p_2	:	Amplitude of pressure signal of microphone in pressure probe
ϕ_2	:	Phase difference of microphone in pressure probe
$C_n^{(\mathrm{m})}$	:	nth complex Fourier coefficients
f_n	:	Frequency of nth Fourier component
j	:	Imaginary unit
M_n	:	Amplitude ratio obtained by the test of frequency response
ϕ_n	:	Phase difference obtained by the test of frequency response
$p^{(\mathrm{ref})}$	:	Amplitude of pressure signal of reference microphone
$\phi^{(\mathrm{ref})}$	:	Phase difference of pressure signal of reference microphone
$p^{(\mathrm{m})}$	:	Amplitude of pressure signal of microphone in pressure probe
$\phi^{(\mathrm{m})}$	:	Phase difference of microphone in pressure probe
$()_{f=f_n}$	:	Value when f is f_n (subscript)
U_0	:	Mean streamwise velocity at nozzle exit
α	:	Yaw angle of pressure probe to flow direction (streamwise direction)
P_α	:	Mean static pressure when yaw angle is α
C_p	:	Pressure coefficient
p_0	:	Mean static pressure when yaw angle is 0
ρ	:	Density of air

p_{f}	:	Measured pressure fluctuation in dynamic calibration
u_{f}	:	Measured streamwise velocity fluctuation in dynamic calibration
u_{c}	:	Convection velocity of disturbance in dynamic calibration
d_{c}	:	Diameter of a circular cylinder in dynamic calibration
x_1	:	Axial (streamwise) coordinate
x_2	:	Vertical (cross-streamwise) coordinate
x_3	:	Spanwise coordinate
U	:	Streamwise velocity
V	:	Cross-streamwise velocity
W	:	Spanwise velocity
u	:	Streamwise velocity fluctuation
v	:	Cross-streamwise velocity fluctuation
w	:	Spanwise velocity fluctuation
d	:	Height of skimmer exit of a plane jet
l	:	Width of skimmer exit of a plane jet
ν	:	Kinematic viscosity
s_1	:	Gap between hot-wire and side wall of pressure probe
s_2	:	Gap between hot-wire and tip of pressure probe
b	:	Half-width of cross-streamwise profile of mean streamwise velocity
τ	:	Time delay
E_{**}	:	Power spectrum of fluctuating value *
k_1	:	Axial wavenumber
η	:	Kolmogorov microscale
ϵ	:	Turbulent energy dissipation
$E(k)$	:	Three-dimensional power spectrum of u
$E_1(k_1)$	:	One-dimensional power spectrum of u
k	:	Turbulent energy
$D(t)$	:	Discriminant function
$\hat{D}(t)$	:	Criterion function
$I(t)$	:	Intermittency function
T_{uI}	:	Integral time scale of streamwise velocity u
R_{vp}	:	Velocity-pressure cross-correlation coefficient
$*\dot{*}$	:	First-order time derivative of **
$*\ddot{*}$	:	Second-order time derivative of **
$\overline{**}$	:	Mean (time averaged) value of **
$**'$	:	RMS value of fluctuating signal ** (superscript)
$**_{\mathrm{c}}$	:	Value of ** at jet centerline (subscript)

Chapter 3

x_1	:	Axial (streamwise) coordinate
x_2	:	Vertical (cross-streamwise) coordinate
x_3	:	Spanwise coordinate
U	:	Streamwise velocity
V	:	Cross-streamwise velocity
W	:	Spanwise velocity
u	:	Streamwise velocity fluctuation
v	:	Cross-streamwise velocity fluctuation
w	:	Spanwise velocity fluctuation
d	:	Height of skimmer exit of a plane jet
l	:	Width of skimmer exit of a plane jet
b	:	Half-width of cross-streamwise profile of mean streamwise velocity
ν	:	Kinematic viscosity
γ	:	Intermittency factor
$I(t)$	:	Intermittency function
T^{ν}_{kij}	:	Viscous diffusion term
T^{p}_{kij}	:	Pressure diffusion term
T^{u}_{kij}	:	Turbulent diffusion term
C_{sDH}	:	Model constant of Daly & Harlow model
C_{sSH}	:	Model constant of Shir model
ϵ	:	Turbulent energy dissipation
k	:	Turbulent energy
T^{p}_{S}	:	Slow term in pressure diffusion term
T^{p}_{R}	:	Rapid term in pressure diffusion term
l_{m}	:	Length scale vector
$\gamma^{\mathrm{nl}}_{\mathrm{m}}$	:	third lank tensor
$\overline{**}$	:	Mean (time averaged) value of **
$**'$	:	RMS value of fluctuating signal ** (superscript)
$**_{\mathrm{T}}$	:	Value of ** when flow state is turbulent (subscript)
$**_{\mathrm{NT}}$	:	Value of ** when flow state is non-turbulent (subscript)

Chapter 4

x_1	:	Axial (streamwise) coordinate
x_2	:	Vertical (cross-streamwise) coordinate
x_3	:	Spanwise coordinate
U	:	Streamwise velocity
V	:	Cross-streamwise velocity
W	:	Spanwise velocity
u	:	Streamwise velocity fluctuation
v	:	Cross-streamwise velocity fluctuation
w	:	Spanwise velocity fluctuation
d	:	Height of skimmer exit of a plane jet
b	:	Half-width of cross-streamwise profile of mean streamwise velocity
l	:	Width of skimmer exit of a plane jet
ν	:	Kinematic viscosity
γ	:	Intermittency factor
$I(t)$	:	Intermittency function
$I_{\mathrm{d}}(t)$	:	Intermittency function of detector
$I_{\mathrm{c}}(t)$	:	Intermittency function of combined probe
t_{d}	:	Time when detector detects the interface
ϵ	:	Turbulent energy dissipation
k	:	Turbulent energy
$\overline{**}$	:	Mean (time averaged) value of **
$**'$	:	RMS value of fluctuating signal ** (superscript)
$**_{\mathrm{con}}$	:	Value of ** at t_{d} (subscript)

Chapter 5

U_∞	:	Free stream velocity in test section
u_{R}	:	RMS value of the streamwise velocity fluctuation
x	:	Axial (streamwise) coordinate
y	:	Vertical (cross-streamwise) coordinate
z	:	Spanwise coordinate
δ_{99}	:	Laminar boundary layer thickness
δ^*	:	Displacement thickness of boundary layer
$\hat{u}(t)$	:	Random component
$\hat{u}_{\mathrm{R}}(t)$	:	Intensity of random component
$U(t)$	:	Instantaneous streamwise velocity
$\overline{U}$	:	Time-averaged streamwise velocity
$\tilde{U}(t)$	:	Ensemble-averaged streamwise velocity
$\tilde{u}(t)$	:	Periodic streamwise velocity fluctuation
N	:	Number of realizations in the ensemble-averaging
C_{p}	:	Pressure coefficient
P	:	Static pressure at each streamwise location
P_0	:	Static pressure at $x = 0$
ρ	:	Density of fluid
η	:	Normalized height from a flat plate based on laminar boundary layer thickness
y^+	:	Normalized height from a flat plate based on turbulent boundary layer thickness
ν	:	Kinematic viscosity
T	:	Actuator activating period
U_{int}	:	Traveling speed of the interface
U_τ	:	Averaged friction velocity

Chapter 6

x_1	:	Axial (streamwise) coordinate
x_2	:	Vertical (cross-streamwise) coordinate
x_3	:	Spanwise coordinate
U	:	Streamwise velocity
$\hat{U}$	:	Phase-averaged streamwise velocity
V	:	Cross-streamwise velocity
W	:	Spanwise velocity
u	:	Streamwise velocity fluctuation
$\hat{u}$	:	Phase-averaged streamwise velocity fluctuation
v	:	Cross-streamwise velocity fluctuation
$\hat{v}$	:	Phase-averaged cross-streamwise velocity fluctuation
w	:	Spanwise velocity fluctuation
p	:	Pressure fluctuation
$\hat{p}$	:	Phase-averaged pressure fluctuation
d	:	Height of skimmer exit of a plane jet
l	:	Width of skimmer exit of a plane jet
b	:	Half-width of cross-streamwise profile of mean streamwise velocity
ν	:	Kinematic viscosity
ϵ	:	Turbulent energy dissipation
k	:	Turbulent energy
f_{p}	:	Frequency of flapping motion
S_t	:	Strouhal number
$w_*(t)$	:	Real parts of wavelet component
$D(t)$	:	Detection function
$I(t)$	:	Intermittency function
$I_{\mathrm{f}}(t)$	:	Flapping intermittency function
T_{p}	:	Flapping period
α	:	Scale parameter
β	:	Time parameter
$s(t)$	:	Time series signal
i	:	Imaginary unit
$\phi(t)$	:	Gabor function
σ	:	Parameter to decide the frequency resolution and the time resolution
$\overline{**}$	:	Mean (time averaged) value of **
$**'$	:	RMS value of fluctuating signal ** (superscript)
$**_{\mathrm{con}}$	:	Value of ** at t_{d} (subscript)

Chapter 1

Introduction

1.1 Background and purpose

The understanding and controlling of turbulent flows are a long-held dream of many researchers all over the world because turbulent flows are strongly related to the fluid machinery, transport machinery, oceanographic science, meteorology, chemical engineering, construction engineering, and so on. Here, take a fluid machinery as an example: the unsteady turbulent flow pattern caused by vortices around the tip (as shown in Figure 1.1) influences the efficiency of the machine [1]. Further, take a transport machinery also as an example: fluctuating velocity by turbulent flow behind the tail vehicle (as shown in Figure 1.2) causes its lateral and vertical vibrations [2]. Therefore, the achievement of the understanding and controlling of turbulent flows is needed and very useful for the developing of these engineerings and sciences.

From this background, many experimental studies on turbulent flows have been widely conducted up to date. In these studies, various themes were set as the target of the study, and a lot of quantities (e.g., velocity, temperature, concentration and pressure) were investigated with the development of measurement techniques to understand the turbulent flow. In particular, the development of the hot-wire anemometer [3][4] made a big impact on the study of turbulent flow and it gave us the progressing of the understanding of turbulent flow because the hot-wire anemometer has a large dynamic response by very small thermal inertia of hot-wire and its compensation of the circuit in the anemometer [5], and it enabled us to measure the velocity fluctuation accurately in a turbulent flow whose characteristics are unsteadiness, randomness, and irregularity.

There are various subjects in the experimental study related to turbulence even in the basic turbulent flows. The examples are as follows; (1): mixing and diffusion, (2): entrainment, (3): turbulent transition and re-laminarization, (4): separation and re-attachment. In this study, from many turbulent phenomena related to the targets described above, the

following three subjects, which can be observed in a turbulent jet and a boundary layer, are focused on and experimentally investigated.

(a) Turbulent/non-turbulent intermittency

(b) Interface between turbulent/non-turbulent region

(c) Large-scale coherent vortex structure

In the subject (a), for the more understanding of the flow characteristics in the turbulent/non-turbulent intermittent region, the entrainment process and the validity of the turbulence models for the pressure diffusion process in the intermittent region of a plane jet are investigated by the simultaneous measurement of the velocity and pressure. Firstly, a new combined probe for the simultaneous measurement of the velocity and pressure in turbulent flows is developed. Then the simultaneous measurement of them in a plane jet is performed and the results are discussed, mainly placing the focus on those of the intermittent region. Further, the entrainment process of the jet is discussed on the basis of the turbulent energy budget and the time variation of the velocity-pressure cross-correlation coefficients in the entrainment or ejection process. In addition, the validity of turbulence models is investigated, using the data obtained by the simultaneous measurement.

In the subject (b), to clarify and understand the flow phenomena near the interface between the turbulent and the non-turbulent (laminar) region, the velocity and pressure fields near the cross-streamwise interface of a plane jet, and the velocity field near the streamwise interfaces of an isolated turbulent region excited into a laminar boundary layer are measured and discussed. The velocity and pressure field near the cross-streamwise interface of a plane jet are measured by means of a combined probe described above. The velocity fields near the streamwise interfaces of an isolated turbulent region are measured by using a single-type hot-wire probe and a rake with six individual hot-wire probes. The measurement data are analyzed by using an ensemble-averaging technique, and the ensemble-averaged data near the interface are discussed.

In the subject (c), the characteristics of the flapping phenomenon, which is one of the large-scale vortex coherent structures in a plane jet and can be observed intermittently in the self-preserving region, are investigated by the simultaneous measurement of the velocity and pressure. The simultaneous measurement is also performed by means of a combined probe described above. The measurement data are analyzed by using a conditional sampling technique and the ensemble-averaging technique, on the basis of an intermittency function, which determines whether the jet is in the flapping motion or not.

This intermittency function is obtained by performing a continuous wavelet transform to the measurement results of two hot-wire probes set in the opposite side of the self-preserving region of the jet which is symmetrical to the jet centerline.

In the following, these three phenomena are called "Intermittent flow phenomena," collectively.

1.2 Previous studies related to the thesis

In this section, previous studies related to the intermittent flow phenomena are described.

Firstly, previous studies related to the turbulent/non-turbulent intermittency and interface (related to the subjects (a) and (b)) are shown in particular placing focus on the wall-free shear flow and the wall-bounded shear flow. Secondly, the studies on the turbulence models (related to the subject (a)) for the pressure diffusion term in the Reynolds-stress transport equation are described mainly about the gradient-diffusion-model and the model of rapid/slow term. Thirdly, the studies on the simultaneous measurement of the velocity and pressure (related to subjects (a), (b), and (c)) are shown. Fourthly, the studies on the large-scale coherent vortex structure are shown especially placing the focus on that observed in a plane jet (related to the subject (c)).

1.2.1 Turbulent/non-turbulent intermittency and interface

Nearly parallel shear flows are divided into two classes: wall-free shear flows and wall-bounded shear flows [6]. For the former flows, such as jet, wake and separated flows, the flow phenomena, characteristics, entrainment process and vortex structures in the intermittent region and the interface between the turbulent/non-turbulent region have been investigated experimentally and numerically. For the latter flows, such as turbulent boundary layer and turbulent spot, the flow phenomena, characteristics, growth/decay mechanism of turbulent region and vortex structures in the intermittent region and near the interface of turbulent/non-turbulent region have been also investigated in various ways.

Wall-free shear flow

At the interface between the turbulent/non-turbulent region in the wall-free shear flow observed in jets and wakes, the entrainment of the non-turbulent fluid into the turbulent

region and the sticking out (nibbling) of the turbulent region into the ambient non-turbulent region arise. These phenomena are very interesting from academic and industrial viewpoints because they are related to the mixing and diffusion processes of the fluid and scalar.

The first study involving the interface of the turbulent and the non-turbulent region in the wall-free turbulent flow was conducted by Corssin et al. [7]. From the experimental results of turbulent round jet, it was found that there was a thin layer referred to as "laminar super layer," which is shown in Figure 1.3, between the turbulent and the non-turbulent region, and the thickness of this layer was almost the same as the Kolmogorov microscale of the turbulent region. It was also found that the laminar super layer was involved in the propagation of the vorticity into the potential field.

The vortex structure in the intermittent region of a self-preserving round free jet was investigated by Komori et al. [8]. From the measurement results of Laser Doppler Velocimetry (LDV), they showed the existence of large-scale coherent vortex structures in the intermittent region that were similar to the coherent vortex structures observed by Yule [9] near the jet exit which is shown in Figure 1.4.

Koso et al. [10] investigated the shape of the interface between the turbulent and the non-turbulent region in a co-flowing turbulent free jet through the multi-point simultaneous measurement of the interface using a rake of hot-wire probes. They indicated that the tip of the turbulent edge bulge moved slower than the co-flowing free stream; this effect was attributed to the large-scale eddy motions in the intermittent region.

In recent researches, the interface between the turbulent and the non-turbulent region was investigated from another point of view. Westerweel et al. [11] indicated that the turbulent/non-turbulent interface was very sharp and that the physical quantities such as the mean streamwise velocity, the Reynolds stress and the temperature, sharply changed at the interface; these findings were based on combined LIF (Laser Induced Fluorescence)/PIV (Particle Image Velocimetry) measurements in the far field of a submerged self-similar turbulent jet. It was also found that a layer of irrotational velocity fluctuations exists outside the turbulent region.

In association with the study by Westerweel et al. [11], Bisset et al. [12] investigated the turbulent/non-turbulent interface in the velocity fields of a turbulent wake behind a flat plate obtained from direct numerical simulations (DNS). They indicated that the thickness of the continuous interface which exhibited rapidly changing physical quantities, shown by the experiment of Westerweel et al. [11] was less than 0.1 times the half-width of the wake and was almost the same as the Taylor's microscale in the turbulent region.

In addition, Silva, et al. [13] performed DNS to investigate the invariants of the velocity gradient, rate-of-strain and rate-of-rotation tensors across the turbulent/non-turbulent interface of the jet.

Wall-bounded shear flow

The interface between the turbulent and the non-turbulent region was also investigated with regard to the turbulent boundary layer. In association with the study by Corssin et al. [7], Imaki investigated the intermittent turbulent region near the outer edge of a turbulent boundary layer with zero pressure gradient using constant temperature linearized hot-wire anemometers [14]. The author presented momentary pictures of the super layer obtained by recording signals, and the passing time of a turbulent lump was measured.

Ichimiya et al. experimentally investigated the time-averaged structure at the interface of the turbulent and the non-turbulent region of the turbulent wedge generated by a small rod [15]. Based on the time-averaged data obtained by the hot-wire anemometers, they found that a pair of streamwise vortices existed at the interface.

Inasawa et al. investigated the flow structure at the spanwise edge of the spreading turbulent region in a laminar flat-plate boundary layer generated by bi-morph type piezo-ceramic actuators set on the flat plate [16]. They found that the turbulent region was constantly sticking out into the laminar region at the middle height of the boundary layer, and a pair of streamwise vortices aligned in the wall-normal direction were found at the interface as shown in Figure 1.5. They also found that the flow induced by these vortices pushed turbulent fluid into the laminar region, and the mechanism by which the turbulent region expands in the spanwise direction was demonstrated.

Then, the studies on a turbulent spot are described. Turbulent spot was first observed experimentally in a boundary layer undergoing the transition process by Emmons [17]. It has been investigated by many researchers to understand the flow phenomena, gowth/shrink mechanisms, and structures near the interface between the turbulent and the non-turbulent region.

Schbauer et al. [18] introduced turbulent spots intermittently into a laminar boundary layer and measured the velocity signals and celerities associated with the spot. They reported the existence of a so-called calmed region that immediately follows the turbulent spot and that was more stable than the surrounding flow.

Coles et al. [19] investigated the velocity field around the turbulent spot by conditional sampling techniques. They focused on the streamline pattern in the center plane of the

spot and suggested that the spot grows not only by entraining laminar fluid from the free stream, but also by entraining fluid from the ambient laminar boundary layer.

Wygnanski et al. [20] also used the conditional sampling technique to investigate the average shape of turbulent spots and the mean flow field in its vicinity. They showed that the fluid deep in the laminar boundary layer travelled faster than the rear interface of the turbulent spot and it was entrained into the spot. Conversely, the fluid outside the boundary layer was passed by the ridge of the spot and was entrained through the leading interface.

In their experiment using a heated rod, Gad-el-hak et al. [21] demonstrated that the growth rate of the turbulent wedge in the spanwise direction was an order of magnitude greater than that in the wall-normal direction, and they concluded that a process other than entrainment contributes to the spanwise growth. They refer to this other process as the destabilization process. Here, a figure of a turbulent spot visualized by them is shown in Figure 1.6.

These researches mentioned above indicated how the turbulent region expanded into the laminar region. Further, it was also revealed that the entrainment process occurring at the leading edge of the turbulent spot plays an important role for the expansion of the turbulent region.

In recent years, a turbulent spot under particular flow conditions have been also investigated by many researchers.

Katz et al. [22] investigated a turbulent spot in an accelerating laminar boundary layer flow. From the measured data, they pointed out that the growth rate of the spot was significantly decreased by the favorable pressure gradients in all three directions (streamwise, wall-normal, and spanwise). They also pointed out that the turbulent spot became much shorter and narrower in comparison with similar spots generated in a Blasius boundary layer at comparable distances from its origin and at comparable Reynolds numbers.

Seifert et al. [23] experimentally investigated the characteristics of a turbulent spot propagating in a laminar boundary layer subjected to a self-similar adverse pressure gradient. They indicated that the rate of spanwise spreading of the spot was affected most significantly by the pressure gradient. They also indicated that the interaction of the spot with the wave packet existing beyond its tip was enhanced by the adverse pressure gradient, because the Reynolds number of the surrounding boundary layer was supercritical everywhere. In addition, they concluded that the maximum linear amplification rate in their case was approximately four times greater than that in a Blasius flow.

Some experiments have been performed by focusing on the leading or trailing edge

of the turbulent spot. Using a rake of miniature thermocouples, Gutmark et al. [24] experimentally investigated a turbulent spot generated artificially in a heated boundary layer. They indicated that the length of the leading edge of the spot increased linearly with the downstream distance. They also indicated that the overhanging region of the leading edge was caused by the upstream turbulence initially closer to the wall but eventually ejected into the free stream. This description was consistent with the study by Smith [25].

Further, the trailing or calmed region of the spot has been investigated by many researchers, and the presence of higher momentum fluid near the wall was revealed (e.g. Antonia et al. [26], Gostelow et al. [27] and Chong et al. [28]). In addition, this characteristic was captured by a theoretical model that was proposed by Brown et al. [29].

In related studies, Schröder et al. [30] investigated the trailing edge of a turbulent spot by using multi-plane stereo particle image velocimetry. They indicated that low-speed streaks in a spot, which were extended into the calmed region, were closely related to hairpin vortices. They also pointed out that these hairpin vortices were most active at the interface between the body and the calmed region of the spot and that this was the main mechanism for turbulence generation at the interface.

1.2.2 Turbulence models for pressure diffusion process

The numerical simulations of turbulent flows are requisite to understand the flow phenomena in detail because it gives us the enormous temporal and spatial information of the flow field. Therefore, many simulation methods have been proposed and a lot of simulations have been performed up to date. Since Reynolds-Averaged Navier-Stokes (RANS) involves the solution of the Reynolds equations to determine the mean velocity field, it is one of the useful methods to simulate the flow field [31]. The Reynolds stresses, which appear as the unknown in the Reynolds equations, are determined by a turbulence model, either via the turbulent-viscosity hypothesis or more directly from the modeled Reynolds-stress transport equations. The former is reffered to as the turbulent-viscosity model, and the latter Reynolds-stress model.

Turbulent viscosity models are based on the turbulent-viscosity hypothesis. The most famous turbulent viscosity model is the k-ϵ model. This model belongs to the class of two-equation models, in which model transport equations are solved for two turbulence quantities k and ϵ. This model is the most widely used complete turbulence model, and it is incorporated in most commercial CFD codes. As is the case with all turbulence models,

both the concepts and the details evolved over time.

Significant earlier studies on the k-ϵ model were conducted by Davidov [32], Harlow et al. [33], Hanjalić [34] and others cited by Launder et al. [35]. After their earlier contributions, Jones et al. [36] developed the standard k-ϵ model and Launder et al. [37] provided improved values of their model constants.

In Reynolds-stress models, model transport equations are solved for the individual Reynolds stress $\overline{u_\mathrm{i} u_\mathrm{j}}$ and for the dissipation ϵ (or for another quantity). Therefore, the turbulent-viscosity hypothesis is not needed; thus one of the major defects of the turbulent-viscosity models is eliminated in this model.

The exact transport equation for the Reynolds stresses is obtained from the Navier-Stokes equations and expressed as follows.

$$\frac{\mathrm{D}}{\mathrm{D}t}\overline{u_\mathrm{i} u_\mathrm{j}} + \frac{\partial}{\partial x_\mathrm{k}} T_\mathrm{kij} = P_\mathrm{ij} + R_\mathrm{ij} - \epsilon_\mathrm{ij} \tag{1.1}$$

where, T_kij is the Reynolds-stress-flux, P_ij the production tensor, R_ij the pressure-rate-of-strain tensor, and ϵ_ij the dissipation tensor. Reynolds-stress-flux T_kij is expressed as follows.

$$T_\mathrm{kij} = T^{\nu}_\mathrm{kij} + T^{p}_\mathrm{kij} + T^{u}_\mathrm{kij} \tag{1.2}$$

Here, T^{ν}_kij, T^{p}_kij, and T^{u}_kij are the viscous diffusion term, the pressure diffusion term, and the turbulent diffusion term, respectively. In the Reynolds-stress model, ϵ_ij, R_ij, and T_kij are required. Consequently, some models of these terms were proposed in previous studies. However, the validity of these models related to the pressure fluctuation in turbulent flows is neither clarified nor understood up to date because the measurement of pressure fluctuations in turbulent flows is not easy. Further, recently, it was shown in some studies [38] that the contribution of the pressure diffusion in the turbulent energy diffusion process was significant and could not be neglected. From this background, to investigate the validity of the proposed models including the pressure diffusion term, the simultaneous measurement of the velocity and pressure is performed in a plane jet in this study. In the following, some models related to the pressure diffusion term are described.

The fluctuating pressure appears in the Reynolds-stress equation most directly as the velocity-pressure-gradient tensor as follows.

$$\Pi_\mathrm{ij} \equiv -\frac{1}{\rho}\left\langle u_\mathrm{i}\frac{\partial p}{\partial x_\mathrm{j}} + u_\mathrm{j}\frac{\partial p}{\partial x_\mathrm{i}}\right\rangle \tag{1.3}$$

Equation (1.3) can be decomposed into the pressure diffusion term PDT and the pressure-rate-of-strain tensor R_ij as follows.

$$\mathrm{PDT} = \frac{\partial T^{p}_\mathrm{kij}}{\partial x_\mathrm{k}} \tag{1.4}$$

$$R_{ij} \equiv \left\langle \frac{p}{\rho}\left(\frac{\partial u_i}{\partial x_j} + \frac{\partial u_j}{\partial x_i}\right)\right\rangle \tag{1.5}$$

As observed by Lumley [39], the decomposition of the velocity-pressure-gradient tensor Π_{ij} into a redistribution term and a transport term is not unique. For example, an alternative decomposition is expressed as follows.

$$\Pi_{ij} = R^a_{ij} - \frac{\partial}{\partial x_l}\left(\frac{2}{3}\delta_{ij}T^p_l\right) \tag{1.6}$$

where, R^a_{ij} and T^p_l are defined as follows.

$$R^a_{ij} \equiv \Pi_{ij} - \frac{1}{3}\Pi_{ll}\delta_{ij} \tag{1.7}$$

$$T^p_l \equiv \overline{u_l p}/\rho \tag{1.8}$$

With the velocity-pressure-gradient tensor Π_{ij} decomposed according to Equations (1.3) and (1.6), the exact equation for the evolution of Reynolds stress is expressed as follows.

$$\frac{\mathrm{D}}{\mathrm{D}t}\overline{u_i u_j} + \frac{\partial}{\partial x_k}\left(T^\nu_{kij} + T^p_{kij} + T^u_{kij}\right) = P_{ij} + R^a_{ij} - \epsilon_{ij} \tag{1.9}$$

where, T^ν_{kij}, T^p_{kij}, and T^u_{kij} are the viscous diffusion term, the pressure diffusion term, and the turbulent diffusion term, respectively, and defined as follows.

$$T^\nu_{kij} = -\nu\frac{\partial\overline{u_i u_j}}{\partial x_k} \tag{1.10}$$

$$T^p_{kij} = \frac{2}{3}\delta_{ij}\overline{u_k p}/\rho \tag{1.11}$$

$$T^u_{kij} = \overline{u_i u_j u_k} \tag{1.12}$$

It should be noted that the viscous diffusion term T^ν_{kij} is negligible except in the viscous wall region.

In the following, we focus on the models related to the pressure diffusion term T^p_{kij} named "Gradient-diffusion-model" and the model for the rapid/slow term in the pressure diffusion term, which are described in detail.

Gradient-diffusion-model

The simplest gradient-diffusion-model for $T'_{kij} = T^u_{kij} + T^p_{kij}$ is proposed by Shir [40] and expressed as follows.

$$T'_{kij} = -C_s\frac{k^2}{\epsilon}\frac{\partial\overline{u_i u_j}}{\partial x_k} \tag{1.13}$$

Here, C_s is a model constant. Shir developed this model to study an atmospheric turbulence in the planetary boundary layer. Shir indicated that the turbulent and pressure diffusion terms which transport the turbulent stresses from one place to another were usually small near the solid surface, but became prominent away from the surface. Then these two terms were treated together and assumed to be of the "gradient-diffusion type" described earlier. It had been argued that the turbulent and pressure diffusion terms should be of hyperbolic type due to the diffusion by large eddies (called "hyperbolic-diffusion type") [41]. In a neutral flow, both approaches ("gradient-diffusion type" or "hyperbolic-diffusion type") may be equally realistic. However, the effective diffusion velocity of the large eddy motion used in the hyperbolic-diffusion type approach should be determined empirically. Further, it was valuable that a more complex approach which calculates the turbulent and pressure diffusion terms by the dynamic equation of triple correlation was not necessary in this case. Therefore, the gradient-diffusion type was adopted for his calculation.

Daly et al. [42] developed a model in general use, which uses the generalized gradient diffusion hypothesis for the triple correlation as follows.

$$T'_{kij} = -C_s \frac{k}{\epsilon} \overline{u_k u_l} \frac{\partial \overline{u_i u_j}}{\partial x_l} \tag{1.14}$$

They derived the transport equations, which describe the dynamics of transient flow of an incompressible fluid in arbitrary geometry so as to incorporate the principles of invariance and universality. Then, applicability of the equations was demonstrated by comparing their solutions with experiments on turbulence distortion on the turbulence in the flow between flat plates. In their model, the pressure-diffusion term was modeled by a simple form with reference to the model proposed by Donaldson [43]. However, eventually they neglected the modeled-pressure diffusion term and assumed that it could be modeled into the turbulent diffusion term, which was modeled as an expression shown in Equation (1.14). Regarding this model, Launder [44] suggests the value of C_s equals to 0.22.

In most Reynolds-stress models, the pressure diffusion term is either neglected or modeled together with the turbulent diffusion term, as described above, because the contribution of the pressure diffusion term is considered to be small and it is difficult to model the pressure diffusion term accurately due to the lack of the measurement data of pressure fluctuation in turbulent flows.

Model of rapid/slow term in pressure diffusion process

In the models described in the previous section, there were no models which include the model for the pressure diffusion process explicitly; its effects were considered to be able to be modeled altogether with the turbulent diffusion process. Consequently, these models were usually calibrated empirically, so that the pressure diffusion may be effectively included. However, on the basis of an analysis of nearly homogeneous turbulence, Lumley [45] proposed separate models for each process: pressure diffusion, and turbulent diffusion. Lumley's pressure diffusion model was derived from considering realizability conditions to a part of the pressure diffusion including the triple moment expressed as follows.

$$\frac{1}{\rho}\overline{u_i p} = -\frac{1}{5}\overline{u_i u_j u_k} \tag{1.15}$$

This model was called a "slow part" of the pressure diffusion process. This slow pressure diffusion process can be modeled as a sub-process of the turbulent diffusion. On the other hand, the pressure diffusion term includes another part consisting of mean strain which is called a "rapid part".

In related to the studies on pressure diffusion process, Demuren et al. [46] examined the rapid term and slow term in pressure diffusion separately by using DNS data and proposed models for each term. Further, Straatman et al. [47] evaluated the models for the diffusion process in zero-mean-shear turbulence and the validity of Lumley's model (the slow part of pressure diffusion term) was confirmed. This was because the zero-mean-shear flow has no mean shear and the rapid term could be neglected.

In the previous studies described above, the slow part in the pressure diffusion process was mainly focused on. However, recently, the effects of mean strain on the pressure-velocity correlation has been discussed, and a model form has been proposed, where the mean shear is explicitly included into the turbulence energy equation [48]. Furthermore, another attempt for the modeling of the rapid part of the pressure-diffusion term by the same modeling strategy as that for constructing the two-component-limit (TCL) realizable second moment closure (SMC) of the UMIST group [49][50] was discussed by Suga [51].

1.2.3 Simultaneous measurement of velocity and pressure

In the present study, the simultaneous measurement of velocity and pressure is performed to investigate the research subjects shown in the previous sections. Here, the previous studies related to the pressure measurement in turbulent flows and the simultaneous measurement of the velocity and pressure are described.

Pressure measurement in turbulent flows

The pioneering experiments to measure the joint statistics of velocity and pressure in a turbulent flow were performed by Kobashi [52] and Kobashi et al. [53]. In these experiments, the pressure fluctuations behind a circular cylinder set in a flow were measured by using a condenser microphone as a pressure sensor. The schematic view of the pressure pick-up developed by Kobashi [52] is shown in Figure 1.7.

Pressure fluctuations that occur within the turbulent flow of the lower atmospheric boundary layer were measured by Elliott [54]. This measurement was performed using an instrument called the "University of British Columbia system", developed by him. This instrument consists of a thin streamlined circular disk at the end of a long stem, which was developed empirically through wind tunnel studies. From the measured results such as power spectra, cross-spectra, coherence, and phase, it was found that the pressure spectra has a well-defined shape that is independent of the height above the surface, while the spectra exhibited a power law behavior with a mean slope of -1.7 at higher frequencies.

Fuchs [55] discussed the possibilities and limitations on direct measurements of the pressure fluctuations in turbulent flows. He analytically investigated several measurement error mechanisms caused by the insertion of a pressure probe into a flow. The experiments using standard condenser microphones in the potential core of circular air jets were performed. They concluded that ordinary condenser microphones with suitably shaped nose curvatures could be used for the measurement of the fluctuating pressure in a turbulent jet. In addition, together with Siddon's important contribution [56] to this problem, it seemed to be well established that the knowledge of turbulence structure in various flows could be extended by employing static pressure devices as a supplement to the widely used hot-wire technique.

Jones et al. [57] measured one-dimensional power spectra for turbulent pressure fluctuations in the driven mixing layer of a circular subsonic jet and then examined them for evidence of spectral similarity. When a large-scale flow on the centerline of the mixing layer is self-preserving, spectral similarity is obtained at a low wavenumber range. In addition, the similarity laws for the power spectra of the turbulent pressure fluctuations were investigated by application of dimensional analysis in the limit of a large turbulent Reynolds number.

George et al. [58] developed spectral models for turbulent pressure fluctuations by direct Fourier transformation of the integral solution into the Poisson equation for a homogeneous constant mean shear flow. From the models they developed and the results measured in the mixing layer of an axisymmetric jet, it was found that the interaction

of turbulence with turbulence obeyed the seven-thirds power law in the inertial subrange and dominated in the high wavenumber region. It was also found that the contribution of turbulence to the mean shear was dominant in the energy containing range and fell off as the eleven-thirds power law in the inertial subrange.

On the basis of the techniques developed by Kobashi [52] and Kobashi et al. [53], Toyoda et al. [59] developed a more advanced type of pressure probe. This probe had a sharp conical tip for reducing the cross-flow error (the error in the measurement which arises when the pressure probe has some attack angle.) and a smaller condenser microphone (0.25-inch diamter) as a pressure sensor as shown in Figure 1.8.

In recent years, techniques for the measurement of pressure in turbulent flows are still being developed and many important data are being collected. A new type of very small pressure probe was developed by Kupferschmied et al. [60] using the new technologies derived from microelectronics and micromechanics. The diameter of the tip of this new probe was 0.84 mm or 1.80 mm with one sensor or three sensors, respectively. These probes were tested in full-sized turbomachinery under industrial conditions and confirmed the potential of the probes was confirmed. Further, the pressure fluctuations between the blades of a sirocco fan in a car air-conditioning system were measured by Sakai et al. [61]. In order to measure the pressure fluctuations between the narrow blades of the sirocco fan, another new type of pressure probe was developed that comprised an L-type pressure probe (with 0.5 mm outer diameter and 0.34 mm inner diameter) and a semiconductor transducer. From the measured results and the formula of Ribner [62][63], the intensity of the sound source was determined from the second derivative of the phase-averaged pressure fluctuation signals.

Simultaneous measurement of velocity and pressure in turbulent flows

A simultaneous measurement of the fluctuating velocity and pressure in a turbulent mixing layer was performed by Naka et al. [64] using an X-type hot-wire probe together with a pressure probe, which is similar to that developed by Toyoda et al. [59]. The diameter of the static pressure probe was 1.0 mm, and it had four static holes (each with a diameter of 0.4 mm). A condenser microphone was used as a pressure sensor. Employing this instrument, the velocity-pressure correlation in a turbulent mixing layer was investigated.

Tsuji et al. [65] investigated the pressure statistics and their scaling in turbulent boundary layer at a large Reynolds number by simultaneous measurements of velocity and pres-

sure. The measurement of pressure was again performed with a pressure probe, which is similar to that developed by Toyoda et al. [59]. However, a small piezoresistive transducer, whose frequency response was from DC to 150 kHz, was used as a pressure sensor, in addition to the condenser microphone used in the previous studies, because the condenser microphone was unable to measure low-frequency pressure fluctuations with high accuracy.

A simultaneous measurement of velocity and pressure in a plane jet was performed by Sakai et al. [66] using an I-type hot-wire probe together with a static pressure probe, which was similar to that used by Naka et al. [64]. The pressure probe had eight static holes on its sidewall and a piezoresistive transducer was used as its pressure sensor. Moreover, the characteristics of the frequency response and cross-flow error of this pressure probe were carefully investigated. The results of the simultaneous measurement were almost the same as those measured separately using hot-wire probe or the pressure probe. From these results, the validity of the simultaneous measurement was confirmed. In addition, the vortex coherent structures in a self-preserving region of the jet were determined from the velocity-pressure cross-correlation.

The simultaneous measurement of velocity and pressure in a wing-tip vortex was performed by Naka et al. [67] using an X-type hot-wire probe together with the pressure probe used in their previous study (Naka et al. [64]). The X-type hot-wire probe and the pressure probe were set downstream of a half wing to measure velocity and pressure data. From the measured results, it was found that the velocity-pressure correlation profiles had distinct peaks near the vortex center. Moreover, it was also found that the gradient of the velocity-pressure correlation contributes significantly to the balance of the turbulence properties.

It should be noted here that a non-intrusive (i.e., without the intrusion of a measurement probe in flow) technique for measuring the instantaneous spatial pressure distribution over a simple area in a flow field were developed by Liu et al. [68]. They used a four-exposure PIV system for measuring the distribution of material acceleration by comparing the velocities of the same group of particles at different times and then integrating them to obtain the pressure distribution. Their validation tests of principles of the technique using synthetic images of rotating and stagnation point flows showed that the standard deviation of the measured pressure from the exact value is about 1.0 %. Further, they measured the instantaneous pressure and acceleration distributions of a two-dimensional cavity water flow field and results were shown.

1.2.4 Coherent structure

In this study, the characteristics of a flapping phenomenon, which is one of the coherent structures in a plane jet as well as an intermittent phenomenon, are investigated by simultaneous measurement of velocity and pressure in a plane jet.

The coherent structure is defined as the large-scale identifiable structure of a turbulent event, which depends on the type of flow. These structures are deduced from spatial correlation measurements, a certain amount of imagination, and plenty of flow visualization results. Many studies on the coherent structure were conducted after the visualization of the near-wall structure in a turbulent boundary layer with usage of hydrogen bubbles by Kline et al., which is shown in Figure 1.9 [69]. They showed that the inner part of the wall layer in the range $5 \leq y^+ \leq 70$ was not at all passive, as one might think.

In the following, the previous studies related to the coherent structure of a plane jet will be described.

Coherent structure in the near field of a plane jet

A jet is a basic shear flow and its characteristics have been investigated by many researchers to date [70][71][72]. Based on the previous researches, the flow field of a plane jet is separated into two main regions. One is the region near the nozzle exit, while the other the region far from the exit. They are called the "near field" and the "far field", respectively. First at all, here, the previous studies related to a coherent structure in the near filed of a plane jet are described.

In the near field of a plane jet, mixing layers and two-dimensional vortex structures are formed on both sides of the shear layer, and the sign of vorticity of these two-dimensional vortex structures becomes opposite. The dependence of their evolution on the velocity profile at the nozzle exit was investigated by Sato [73], Rockwell et al. [74], and Thomas et al. [75]. Their experimental results were consistent with the linear-stability-analysis by Mattingly et al. [76].

These two shear layers gradually spread with the entrainment of the ambient fluid and their interaction arises about four to five times the height of nozzle exit downstream of the jet exit. Hussain [77] indicated that these interactions arose at the edge of the potential core of the jet. Consequently, in general, the near field of a plane jet is also separated to two fields and discussed. One is the region where these interactions arise which called "Interaction region", and the other is the region where the potential core remains which called "Potential-core region".

Weir et al. [78] investigated the structural changes that occur when two shear layers interact in the potential-core region of a plane jet as shown in Figure 1.10. Their experimental results showed that significant changes in turbulence structure occurred, at least in the region near the center-line where the interaction between the two mixing layers was strongest and the triple products (correlations) were most affected in contrast to the situation in a plane duct [79]. However, mainly because the shear stress near the center-line was small, the results of calculations using a method optimized for a single mixing layer in the "time-sharing" superposition analysis proposed by Bradshaw et al. [80] were fairly satisfactory even for large distances from the nozzle.

Browne, et al. [81] measured all three velocity fluctuations and the temperature fluctuation in a slightly heated turbulent plane jet in the interaction region, which was situated between the location where the two shear layers nominally merged and that which corresponded to approximate self-preservation shown in Figure 1.11. Experimental results showed that the mixing-layer structures were symmetrical with respect to the centerline, and when they met in the interaction region the redistribution of turbulence quantities was dramatic. Moreover, the evolution, on the centerline, of probability density functions of temperature fluctuations and their associated moments, and the streamwise evolution of profiles of the Reynolds shear stress, average heat fluxes, and turbulent Prandtl number indicated a non-monotonic approach to the state of self-preservation.

Coherent structure in the far field of a plane jet

In a far field of a plane jet, the similarity law [71] of the statistical value of the flow field is realized and the region is called "self-preserving region". In the self-preserving region, instantaneous flow structure or vortex structure in a far filed is very complicated. So that, superimposed vortex structures consist of small scale homogeneous vortex structure and large-scale coherent vortex structure can be observed [82].

The first report of the coherent structures in a self-preserving region of a plane jet was conducted by Goldschmidt et al. [83]. They indicated that there was a flapping which may add a new dimension to the interpretation of a plane turbulent jet. The experimental results casted some doubt on those of Wygnanski et al. [84] who suggested that there was no flapping in a plane jet. The term "flapping" was named from the visual image of this phenomenon that the jet flaps as a flag does.

Everitt et al. [85] investigated the structure and development of a plane turbulent jet in still air and moving streams. They indicated that the flapping motion (large-scale vortex

structure) was not revealed in a jet in a moving stream although it could be described in a jet in still air by the correlation measurements.

Cervantes et al. [86] measured four types of correlations in the self-preserving region of a turbulent plane jet. They indicated that the negative correlations were noted between the two halves of the jet and an apparent flapping like motion was exhibited. Further, they showed that the flapping motion was self-preserving and most likely attributed to the presence of large-scale coherent structures.

Oler et al. [87] generated the mean velocity profiles and entrainment rates in the self-preserving region of a plane jet by using a simple superposition of Rankine vortices arranged to represent a vortex street in numerical simulation shown in Figure 1.12. The spacing between the vortex centres, their two-dimensional offsets from the jet centerline, as well as the core radii and circulation strengths, were all governed by similarity relationships and based upon experimental data. The calculated results indicated that the hypothesized structure could be realized of giving virtually exact representations of the velocity decay rate, mean-velocity profiles, and the Reynolds-stress distribution. In addition, it was shown that the key feature of the vortex-street model was the inclusion of the effects of global flow development on locally measured or calculated turbulent flow properties. Further, they indicated that the essential mechanism for the production of Reynolds stress and entrainment appears to be the non-symmetric influence of the upstream and downstream large-scale vortex structures as they diffused and were convected past a particular point of interest.

Antonia et al. [88] performed the measurements of space-time correlations of longitudinal and normal velocity fluctuations and of temperature fluctuations. The experimental results supported that the existence of counter-rotating spanwise structures appearing alternately on opposite sides of the jet centerline in the self-preserving region of the flow. The frequency of these structures closely satisfied the self-preservation. The asymmetric arrangement of the structures was first observed downstream of the position where the jet mixing layers nominally merge but upstream of the onset of self-preservation. Further, closer to the jet exit, the space-time correlations indicated that the existence of spanwise structures that were symmetrical about the centerline.

Mumford [89] measured velocity fluctuations in the fully developed region of a plane turbulent jet by means of arrays of hot-wire anemometers. The measured data was processed to extract information about the structure of the large eddies within the flow. Firstly, they evaluated a selection of the two-point velocity correlation functions, and diagrams of the contours of constant correlation for the streamwise velocity component were

constructed. Then, an iterative procedure similar to the techniques generally described as "pattern recognition and image enhancement" was used to form ensemble averages of the two-dimensional patterns of the streamwise velocity component associated with the large vortex structures. The experimental results showed that the large eddies in the fully developed turbulent region were roller-like structures with aligned approximately either with the direction of the strain associated with the mean-velocity gradient or with the direction of homogeneity combinations.

Thomas et al. [90] investigated the large-scale vortex structural patterns in the self-preserving region of a plane turbulent jet. The experimental results of the two-point correlation and coherence-based measurements obtained from both longitudinal and lateral component velocity fluctuations were supportive of the existence of an antisymmetric array of counterrotating vortices in the region. Further, they indicated that the structural array propagated at 60 % of the mean streamwise velocity on the jet centerline.

In recent years, the statistical analysis, such as POD (Proper Orthogonal Decomposition) analysis, and extracting of the coherent structures in a plane turbulent jet was performed.

Gordeyev et al. [91] investigated the coherent structure in the self-preserving region of the plane turbulent jet experimentally by applying POD. In the measurement, twin cross-stream rakes of X-wire probes were used to take cross-spectral measurements with different spanwise separations between the rakes and at several locations throughout the self-preserving region. The measurement results suggested that the flow supported a planar structure aligned in the spanwise direction as well as an essentially three-dimensional structure with asymmetrical shape in the cross-stream direction and pseudo-periodically distributed in the spanwise direction.

Sakai et al. [92] performed the simultaneous measurement of the main streamwise velocity and the KL (Karhunen-Loève) expansion was applied to the measured data to extract and clarify the coherent structure in a plane turbulent jet. The measurements of the velocity were performed at 21 points in the self-preserving region of a turbulent plane jet by an array of I-type hot-wire probes. They indicated that the low-numbered (energetic) modes represented the large-scale (coherent) structure, the middle-numbered modes represented the finer (small-scale) random structure, and the higher-numbered modes contributed mainly to the intermittent structure in the outer region from the investigation of the random coefficients and the eigen functions (modes). Further, they also showed that there existed a pair of fluid lumps with the positive and negative streamwise velocity fluctuation on the opposite sides of the jet centerline, and the signs of velocity fluctuation for

those fluid lumps changed alternately as time proceeds from the spatio-temporal velocity field reconstructed by the first KL mode. Moreover, these characteristics were consistent with the flapping phenomenon.

1.3 Outline of the thesis

The contents of the thesis consist of seven chapters and two appendixes as outlined below.

Chapter 1 is the present introduction, which describes the background and purpose of the study and the review of previous related studies.

In Chapter 2, the newly developed combined probe for the simultaneous measurement of velocity and pressure in turbulent flows are described. The combined probe consisted of a pressure probe placed between two hot-wires that comprised an X-type hot-wire probe, and the tip of the pressure probe is reduced to a smaller size by reshaping. At first, the measurement accuracy of the pressure fluctuation in turbulent flows is investigated by using the new pressure probe with reference to the previous studies. Then, the effect of the spatial arrangement of the hot-wire probe and the pressure probe is carefully examined in order to decrease the interference between these probes during the simultaneous measurements of velocity and pressure. The measurement accuracy of the new combined probe is also investigated by comparing the data of measurements taken in a plane jet using the new combined probe with those taken using the previous type of combined probe. In addition, the turbulent energy budget and the cross-correlation coefficient of velocity and pressure in the intermittent region of the plane jet are estimated.

In Chapter 3, the results of the simultaneous measurement of velocity and pressure in a plane jet by using a combined probe shown in Chapter 2 are described. In the experiment, firstly, the conditional ensemble-averaged statics are investigated on the basis of the intermittency function obtained from the velocity signal by the hot-wire sensor set in the intermittent region of a plane jet to understand the intermittent flow phenomena. Secondly, the validity of the turbulence models for diffusion process and the models for the rapid/slow part of the pressure diffusion term are discussed by the obtained data mainly placing the focus on the relation between the validity of the models and the intermittency.

In Chapter 4, the flow characteristics and vortex structure near the turbulent/non-turbulent interface in a self-preserving region of a plane jet are shown on the basis of the results of simultaneous measurement of velocity and pressure. The measurements are also performed using a combined probe shown in Chapter 2. The measurement data

are analyzed by the conditional sampling technique and an ensemble-averaging technique on the basis of the intermittency function for the turbulent/non-turbulent decision. In addition, the turbulent energy budget near the turbulent/non-turbulent interface is also discussed.

In Chapter 5, the results of the investigation of the streamwise interfaces of an isolated turbulent region in a flat plate boundary layer are described. The investigation is performed by a wind tunnel experiment. In the experiment, a turbulent region is periodically generated in a laminar boundary layer by periodically activating bimorph-type piezoceramic actuator that raises its trailing end from the wall. For an understanding of the mechanism by which the turbulent region spreads in the streamwise direction, the results are discussed particularly from the perspective of the transport of the turbulent/laminar fluid through the interfaces.

In Chapter 6, the characteristics of a plane jet in the flapping motion, such as the velocity field, pressure field, turbulent energy budget, interval of arising of the flapping, and its duration are investigated and discussed. The measurements are performed by using a combined probe shown in Chapter 2. The measured data are analyzed by using a conditional sampling technique and the ensemble-averaging technique, on the basis of an intermittency function which is used to determine whether the jet is in the flapping or not. The intermittency function is obtained by the newly proposed method using the continuous wavelet transform with the Gabor mother wavelet.

Chapter 7 summarizes the conclusions drawn from each of the previous chapters.

Finally, as an Appendix A, a study on the characteristics of the constant temperature anemometer (CTA) used in this study are shown. Further, as an Appendix B, the influence of the cross-flow on the measurement accuracy of the pressure probe used in this study is also shown.

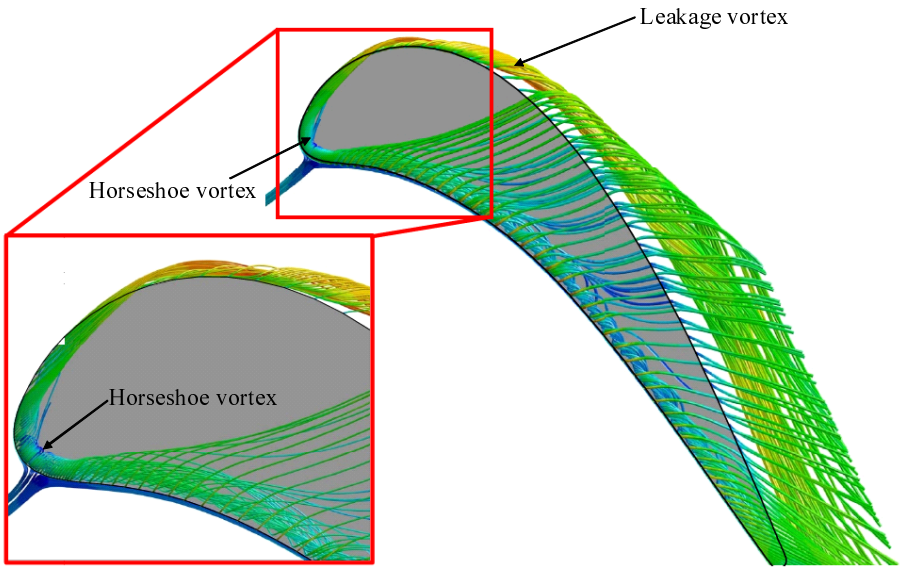

Figure 1.1 Flow pattern and vortices around the tip [1].

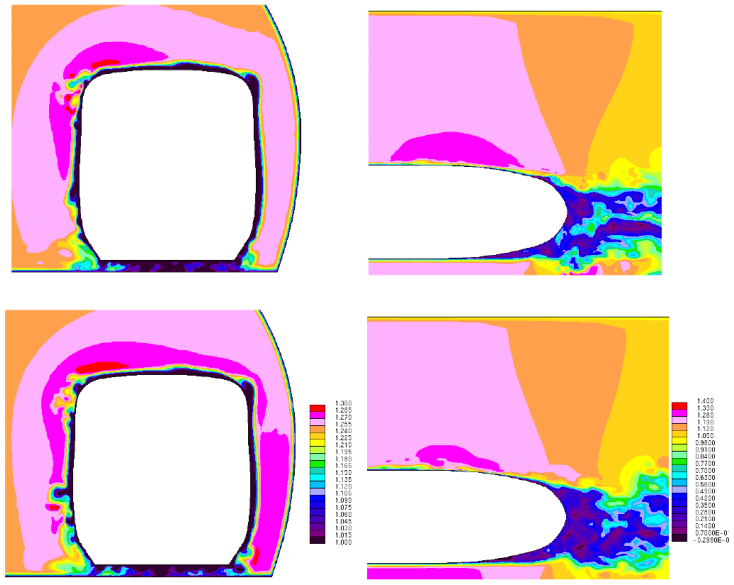

Figure 1.2 Instantaneous velocity magnitude behind the tail car of the *Shinkansen* model [2].

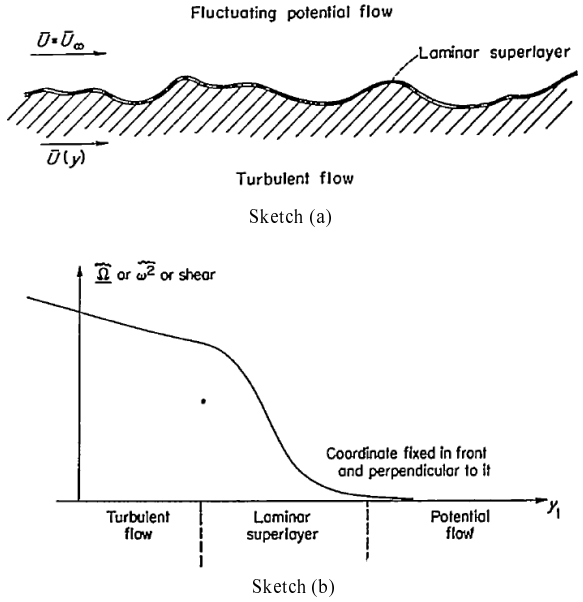

Figure 1.3 Concept of the super layer (Sketch (a)) and the total shear drop from values characteristic of fully turbulent flow to practically zero (Sketch (b)) [7].

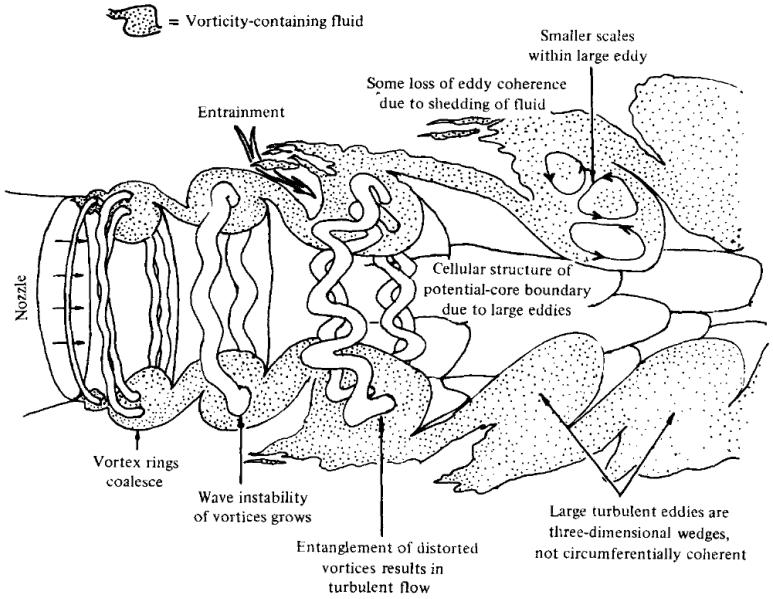

Figure 1.4 Physical structure of a transitional round jet [9].

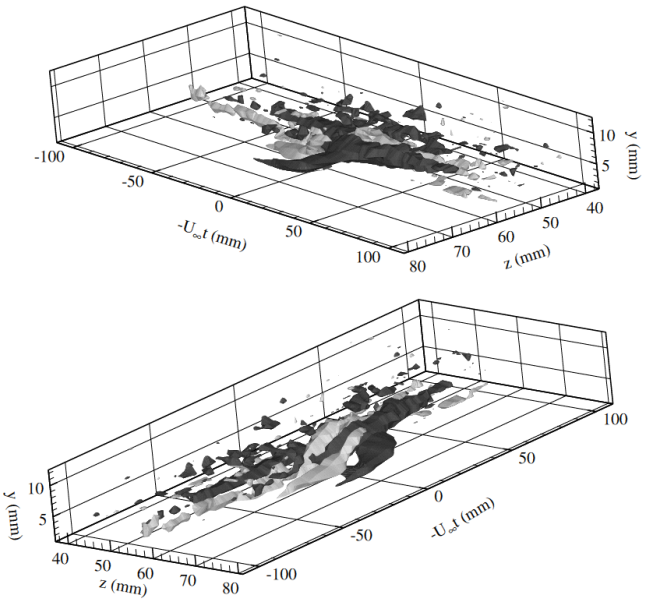

Figure 1.5 Three-dimensional view of iso-surfaces of conditionally averaged streamwise vorticity fluctuations [16].

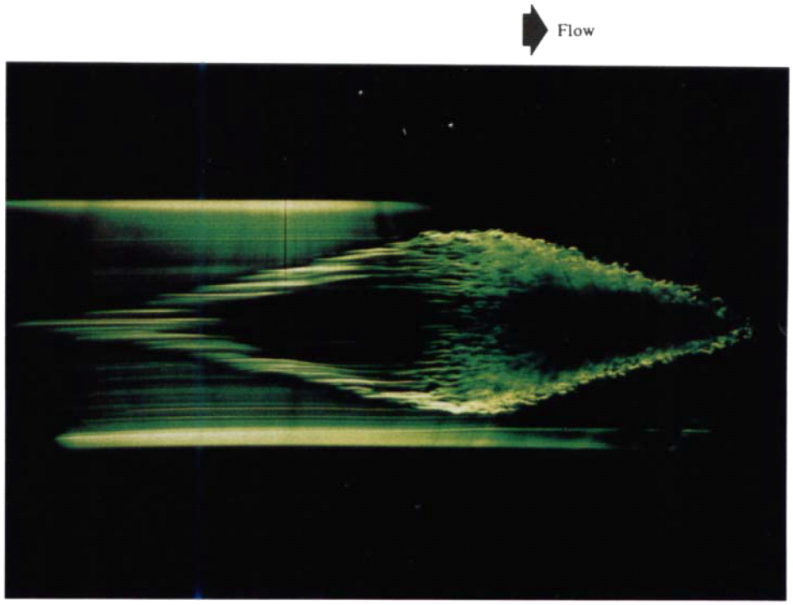

Figure 1.6 A plane view of a turbulent spot [21].

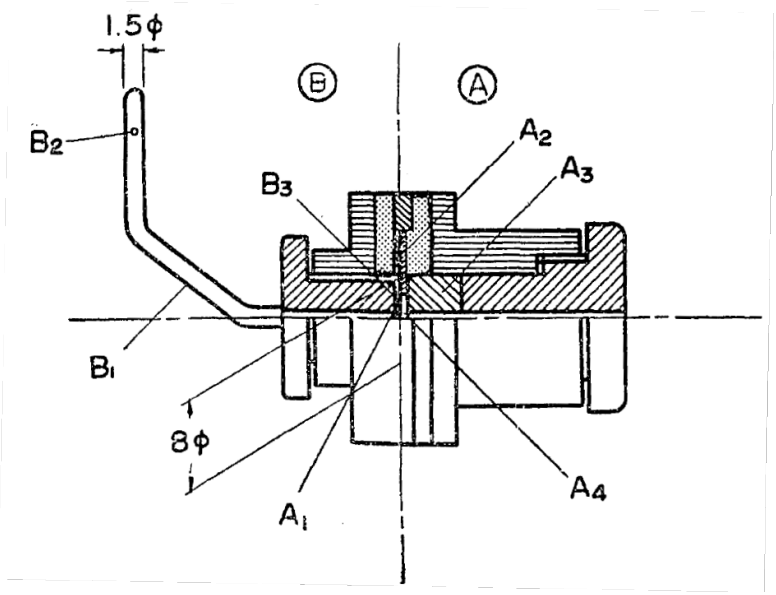

Figure 1.7 Schematic view of pressure pick-up [52]. Part A in the figure is a condenser microphone and Part B the system of pressure duct.

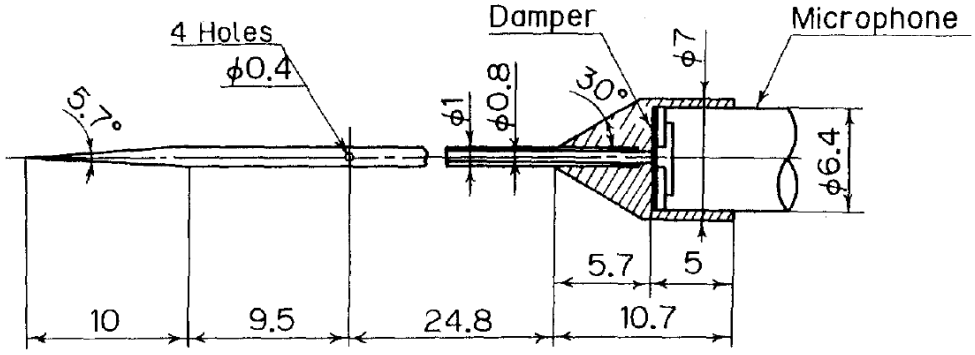

Figure 1.8 Schematic view of the pressure probe with a conical tip [59].

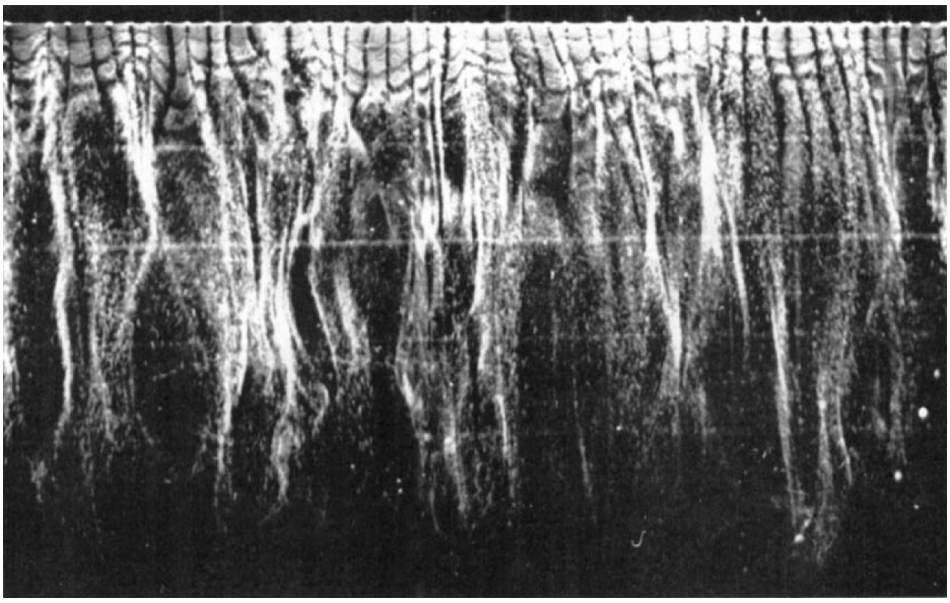

Figure 1.9 Top view of near-wall structure in a turbulent boundary layer [69].

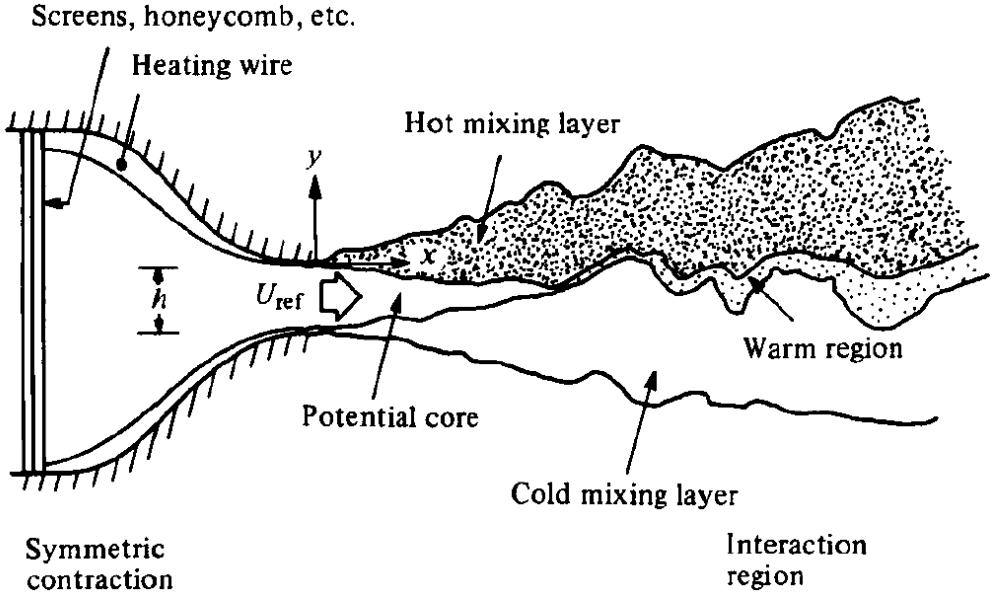

Figure 1.10 Schematic diagram of test region (not to scale) [78].

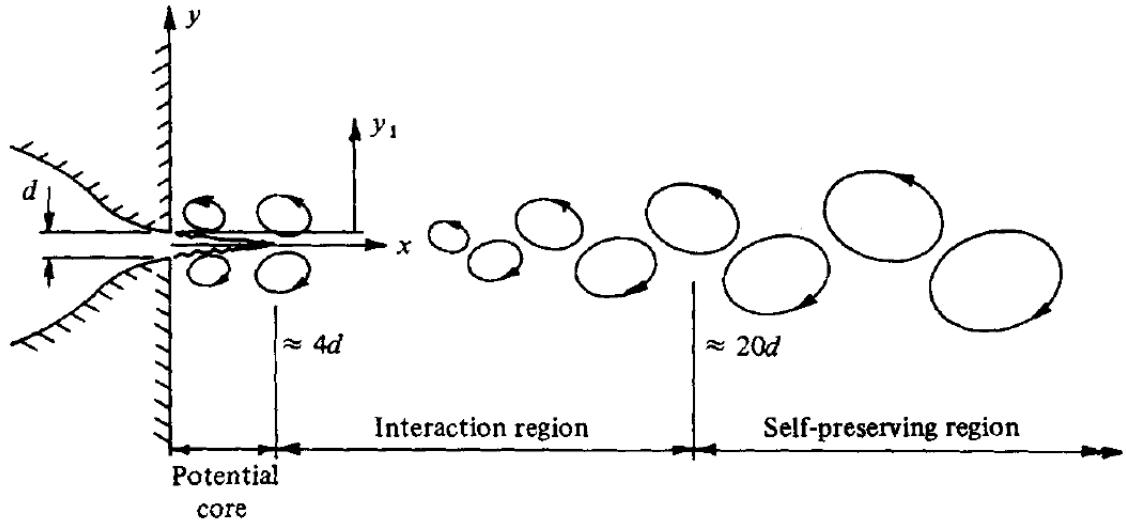

Figure 1.11 Simplified view of the vortex structure in a plane jet [81].

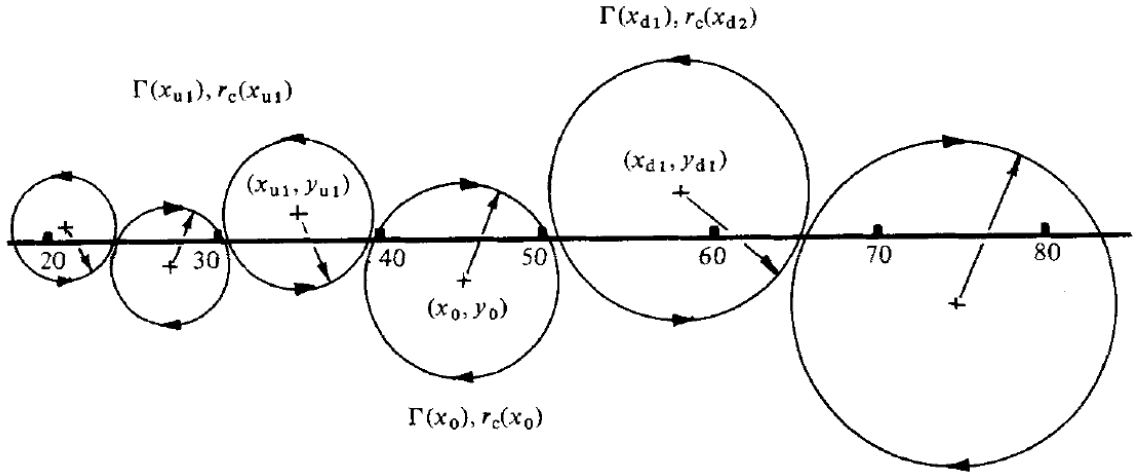

Figure 1.12 A vortex-street representation of a plane jet [87].

Chapter 2

Development of a combined probe
[93][94][95][96]

2.1 Introduction

The experimental study of turbulent flows by the measurement of velocity fluctuation has been actively pursued over the years because the coherent structures in turbulent flows are very closely related to the vibration, aeroacoustic, and mixing enhancements of turbulent flows. However, to understand these physical characteristics, joint statistics for the velocity and pressure are needed, because the fundamental equations that describe turbulent flows (e.g., the incompressible Navier-Stokes equation) contain both the velocity fluctuation and the pressure fluctuation terms. In addition, pressure fluctuations in turbulent flows play a very important role in the behavior of inhomogeneous and anisotropic turbulence [31]. From these points of view, several experiments have been performed so far to measure the pressure statistics or the joint statistics of the velocity and pressure as described in Chapter 1.

In previous studies, the techniques for measuring pressure fluctuation and for simultaneously measuring the velocity and pressure in turbulent flows have been improved or advanced. However, some problems to acquire highly accurate data of simultaneous measurements remain to be solved.

One of such problems is the measurement accuracy of the pressure fluctuation in turbulent flows that is measured using a pressure probe. Therefore, recently a new non-intrusive technique, which does not require the probe installation has been developed for measuring the instantaneous spatial pressure distribution in a simple water flow [68]. The non-intrusive technique seems to be highly prospective but still under development.

Another problem is the spatial arrangement of the hot-wire probe and the pressure probe. In past studies [64][65][66], the hot-wire probe was placed beside the static pressure hole on the sidewall of the pressure probe and the gap between the hot-wire sensor

and the static pressure hole was ranged from 1.0 mm to 2.5 mm. This was because the measurement accuracy of each probe would be reduced by the velocity or pressure disturbances caused by the other probe if the gap was too small. The relative positions of the hot-wire probe and the pressure probe were slightly different for the cross-streamwise (or spanwise) direction, so that no improvement of the spatial resolution of the simultaneous measurement could be expected for such a spatial arrangement.

In the present study, a new combined probe is developed to improve the spatial resolution and measurement accuracy in the simultaneous measurement of the velocity and pressure. The combined probe consists of a pressure probe placed between two hot wires that comprised an X-type hot-wire probe, and the tip of the pressure probe is reduced to a smaller size by reshaping. First, the measurement accuracy of the pressure fluctuation in turbulent flows is investigated by using the new pressure probe with reference to previous studies [55][58][59]. Then, the effect of the spatial arrangement of the hot-wire probe and the pressure probe is carefully examined in order to decrease the interference between these probes during the simultaneous measurements of the velocity and pressure. The measurement accuracy of the new probe is also investigated by comparing the data of measurements taken in a plane jet using the new combined probe with those taken using the previous type of combined probe. In addition, the turbulent energy budget and the velocity-pressure cross-correlation coefficient in the intermittent region of the plane jet are estimated.

2.2 Improvement of the combined probe for simultaneous measurement

2.2.1 Miniaturization of pressure probe

For miniaturization of the pressure probe, the tip shape of the pressure probe is altered. The schematic views of the new pressure probe and the previous pressure probe [97][98] are shown in Figures 2.1 and 2.2, respectively. The shape of the tip of new pressure probe is hemispherical, like that of a pitot tube. The external diameter and the internal diameter of the pressure probe are 0.5 mm and 0.34 mm, respectively. There are eight pressure holes on the sidewall of the pressure probe, and the diameter of each pressure hole is 0.2 mm. As shown in Figure 2.1, four of these holes are located at 0.75 mm from the tip of the pressure probe, whereas the others are located at 1.25 mm from the tip of the pressure probe and are inclined at 45° to the first (tip side) four holes. A 0.1-inch miniature

microphone, which acts as a pressure sensor, is embedded within the flare of the pressure probe. The sensitivity of the microphone is 16 mV/Pa, and it has a flat frequency response from 20 Hz to 10,000 Hz. The modulation of the amplitude and the phase difference of the pressure fluctuation signal, which are caused by the Helmholtz resonance and organ-pipe resonance, arise in the pressure probe. Theoretically, the frequencies of the Helmholtz resonance, f_{h} and organ-pipe resonance, f_{o} are 3,600 Hz and 17,000 Hz, respectively, for this pressure probe. These resonance frequencies were estimated from the equation used in a previous study [66].

$$f_{\mathrm{h}} = \frac{c_0}{2\pi}\frac{d_1}{d_2}\sqrt{\frac{1}{Nl_1l_2}} \tag{2.1}$$

Here, d_1 and d_2 are the inner diameters of the conduit pipe (0.34 mm) and the diameter of the space in the flare where the microphone is embedded (2.6 mm), respectively. Further, c_0 is the sound speed, l_1 is the length of the conduit pipe of the pressure probe (10 mm), and l_2 is the thickness of the gap between the surface of the microphone and the edge of the conduit pipe (assumed to be approximately 0.3 mm and shown by dot-line in Figure 2.1), N is expressed as

$$N = 1 + \frac{8d_1}{3\pi l_1} \tag{2.2}$$

The frequency of the organ-pipe resonance is given by

$$f_{\mathrm{o}} = \frac{c_0}{2l_1} \tag{2.3}$$

The experimental apparatus used in the test of frequency response is shown in Figure 2.3. A new pressure probe (with 0.1-inch microphone) is placed with its pressure holes (first four holes) located approximately at 50 mm away from a speaker, while a similar 0.1-inch (reference) microphone is placed with its sensing surface located at 50 mm from the speaker. A sinusoidal wave in the range from 100 Hz to 10,000 Hz is generated by an oscillator, amplified by an audio-amplifier, and radiated as sound from the speaker. The sound signals measured by the microphone in the pressure probe and the reference microphone are both transformed into voltage signals and stored on the hard disk of a computer via an A/D converter. From the measured data, the amplitude ratio and the phase difference of the signals obtained by these microphones are estimated. The amplitude ratio M and phase difference φ are defined as

$$M \equiv p_2/p_1 \tag{2.4}$$

$$\varphi \equiv \varphi_2 - \varphi_1 \tag{2.5}$$

Here, p_1 and φ_1 are the amplitude and the phase of the signals measured by the reference microphone, respectively. Similarly, p_2 and φ_2 are the amplitude and the phase of the signals measured by the microphone in the pressure probe, respectively.

The amplitude ratio M and the phase difference φ are shown in Figures 2.4 and 2.5, respectively. In the plots shown in these figures, the resonance frequency is observed at approximately 5,500 Hz. This frequency is obtained when gap l_2 in Equation (2.1) is approximately set to 0.13 mm. Note that the difference between the predicted Helmholtz resonance frequency (3,600 Hz) and that measured (5,500 Hz) is caused by the error of assuming firstly the thickness of the gap l_2 to be 0.3 mm.

The Helmholtz resonance frequency (5,500 Hz) of the new pressure probe is less than that of the previous pressure probe (12,000 Hz [66]) because the inner diameter of the pressure probe, d_1 is smaller than that of the previous probe. This means the results of spectral analysis of the pressure fluctuations have errors when the Nyquist frequency is greater than 5,500 Hz (i.e., when the sampling frequency is greater than 11,000 Hz). Therefore, in this study, the modulations of the amplitude and the phase difference are digitally corrected following the previous study [97][98]. The true pressure signal $p(t)$ is obtained as

$$p(t) = \sum_{n=0}^{n_{\max}} \left(\frac{C_n^{(\mathrm{m})}}{M_n} \exp\left\{-j\left(2\pi f_n t - \varphi_n\right)\right\} \right) \tag{2.6}$$

where, $C_n^{(\mathrm{m})}$ denotes the nth complex Fourier coefficients of the signal measured by the pressure probe, f_n is the frequency of the nth Fourier component, and j is the imaginary unit. M_n and φ_n are the amplitude ratio and the phase difference obtained by the test of frequency response. Here, these are expressed as:

$$M_n = \left(p^{(\mathrm{m})}/p^{(\mathrm{ref})}\right)_{f=f_\mathrm{n}} \tag{2.7}$$

$$\varphi_n = \left(\varphi^{(\mathrm{m})}/\varphi^{(\mathrm{ref})}\right)_{f=f_\mathrm{n}} \tag{2.8}$$

where, $p^{(\mathrm{ref})}$ and $\varphi^{(\mathrm{ref})}$ are the amplitude and the phase obtained by the reference microphone whereas $p^{(\mathrm{m})}$ and $\varphi^{(\mathrm{m})}$ are those obtained by the microphone in the pressure probe. The notation $(\ )_{f=f_\mathrm{n}}$ denotes the value when the frequency f is equal to f_n. The corrected pressure signals can be obtained by this modulation method.

The experimental apparatus used to check the cross-flow error of the pressure probe is shown in Figure 2.6. During the experiment, a wind tunnel with a square exit (80 mm $\times$ 80 mm) is used, and the pressure probe is placed in a uniform main stream with a

nozzle exit velocity U_0 of 10 m/s or 20 m/s and with a yaw angle α that ranged from -30° to +30°. The pressure at each yaw angle α is measured by a micromanometer. The measured pressure P_α is normalized by the following equation:

$$C_{\mathrm{p}} = \frac{P_\alpha - P_0}{(\rho U_0^2)/2} \tag{2.9}$$

where, p_0 is the mean pressure at $\alpha = 0°$ and ρ is the density of the air.

Figures 2.7 and 2.8 show the cross-flow error of the pressure probe at $U_0 = 10$ m/s and 20 m/s, respectively. The filled circles show the results measured by the new pressure probe (Figure 2.1), and the open circles show those measured by the previous probe (Figure 2.2). Figures 2.7 and 2.8 also show that the cross-flow error of the new pressure probe is less than approximately 0.05 (5 %) to the dynamic pressure $\rho U_0^2)/2$ at such yaw angles (-10° $\leq \alpha \leq$ +10°), and nearly the same as that of the previous pressure probe. This cross-flow error will be also corrected for the pressure signals on the basis of instantaneous flow angle data as explained later (in section 2.2.2).

2.2.2 Measurement accuracy of new pressure probe

In this study, the pressure probe is installed in a flow to measure pressure fluctuation and this technique has been widely used in previous studies. However, this technique is intrusive because the probe itself has some volume. Therefore, the measurement accuracy of the pressure probe is validated using a calibration by referring to previous studies [55][58][59].

The calibration is performed in the wake of a circular cylinder. The true pressure is predicted with the measured velocity by the following equation [55][59]:

$$p_{\mathrm{f}} = -\rho(\overline{U} - u_{\mathrm{c}})u_{\mathrm{f}} \tag{2.10}$$

where p_{f} and u_{f} are the pressure and streamwise velocity fluctuation, ρ is the density of fluid, $\overline{U}$ is the mean velocity, and u_{c} is the convection velocity of disturbance. Here, it should be noted that Equation (2.10) was deduced from the inviscid momentum equation. Therefore, p_{f} and u_{f} must be measured in the potential flow region outside the Karman vortices behind the circular cylinder.

The apparatus used for the calibration is shown in Figure 2.9. A wind tunnel with a square exit (80 mm × 80 mm) is used. The coordinate system is as follows: the axial (streamwise) coordinate is x_1, the vertical (cross-streamwise) coordinate is x_2, and the origin of the coordinate is set at the center of the nozzle exit. A circular cylinder with

a diameter d_c (0.5, 1.0, 3.0, 6.0 mm) is set at the origin of the coordinate and the flow velocity at nozzle exit U_0 is set at 5, 10, or 20 m/s. The frequencies of the vortex shedding f_c are in the range of 166 - 2,000 Hz. The measurements are performed at $x_1/d_c = 1.80$ and $x_2/d_c = 1.25$.

Figure 2.10 shows the ratio of the RMS (Root Mean Square) value of the measured pressure fluctuation p' and that of the predicted value p'_f. The ordinate is p'/p'_f and the abscissa is f_c. Here, $p'/p'_f = 1.0$ means the measurement error is equal to zero. Figure 2.10 indicates that the maximum measurement error of the pressure fluctuation is 10 %, which is much smaller than the value of 18 % obtained in a previous study [59].

2.2.3 Spatial arrangement of combined probe

The spatial arrangement of the pressure probe and the hot-wire probe, particularly the gap between the probes, is very important for the accuracy of the simultaneous measurement of the velocity and pressure in turbulent flows, because in some cases, the disturbances caused by one probe influence the measurement accuracy of the other probe. Therefore, the influence of this gap between the pressure probe and the hot-wire probe on the measurement accuracy is investigated. This investigation is indispensable for the optimization of the spatial arrangement of each probe.

In this study, the investigation is performed in a plane jet. The reason why a plane jet is chosen is that a plane jet is a basic classical flow and there are plenty of past measured results to be compared with. Figure 2.11 shows a schematic view of the experimental apparatus and coordinate system of the present plane jet. A skimmer is installed approximately 1.0 mm downstream of the nozzle exit in order to eliminate the boundary layer that developed along the contraction wall of the nozzle. Height d and width l of the skimmer exit are 12 mm and 236 mm, respectively. Velocity U_0 at the skimmer exit is 27.5 m/s, and the Reynolds number Re ($=U_0 d/\nu$, ν is kinematic viscosity) is 22,000. Further, the sidewall is set vertically in the test section in order to inhibit entrainment from the surroundings on each side. Using the skimmer and the sidewall, a uniform velocity profile at the skimmer exit and a good two-dimensional flow field in the test section are realized. The coordinate system is as follows: the axial (streamwise) coordinate is x_1, the vertical (cross-streamwise) coordinate is x_2, the spanwise coordinate is x_3, and the origin of the coordinate is set at the center of the nozzle exit. The sampling frequency of the pressure probe and the hot-wire probe is 10 kHz, and the number of sampling is 262,144. In the preliminary experiments, it was confirmed that the sampling length is adequate to obtain

Table 2.1 Combinations of s_1 and s_2 for the investigation.

No.	s_1 (mm)	s_2 (mm)
1	0.25	0.0
2	0.40	0.0
3	0.50	0.0
4	0.25	1.0
5	0.40	1.0
6	0.50	1.0
7	0.25	2.0
8	0.40	2.0
9	0.50	2.0

the reliable turbulence statistics. The measured data are stored on the hard disk of a personal computer via an A/D converter, and then the data are statistically analyzed.

In this study, to estimate the degree of interference between the hot-wire sensor and the pressure probe, firstly the preliminary experiments have been performed by using the I-type hot-wire probe and the pressure probe that are shown in Figure 2.12. The hot-wire, of diameter 5.0 μm and length 1.0 mm, is connected to a self-made constant temperature anemometer. The coordinate directions shown in Figure 2.12 correspond to those of the plane jet shown in Figure 2.11. The gap between the hot-wire and the sidewall of the pressure probe is denoted by s_1, and the gap between the hot-wire and the tip of the pressure probe is denoted by s_2. The influence of gaps s_1 and s_2 on the measurement accuracy of the pressure probe and the I-type hot-wire probe is investigated for several combinations of s_1 and s_2 as shown in Table 1, and the best combination of s_1 and s_2 (for minimal influence) is determined. In practice, the influence is estimated by comparing the results measured by the combined probe with those measured individually by either the pressure probe or the hot-wire probe alone.

Figure 2.13 shows the axial variations of the streamwise mean velocity in the cases of $s_1 = 0.25$ mm, 0.40 mm, and 0.50 mm when s_2 is fixed to 0.0 mm. The ordinate is $\overline{U_c}/U_0$, and the abscissa is x_1/d, where $\overline{U_c}$ is the streamwise mean velocity on the jet centerline, U_0 is the streamwise mean velocity at the skimmer exit, and d is the height of the skimmer exit. The solid line shows the results measured by the I-type hot-wire probe alone (i.e., without the pressure probe). The open squares, open triangles, and open downward triangles in Figure 2.13 shows the results measured for $s_1 = 0.25$ mm, 0.40 mm,

and 0.50 mm, respectively. As seen in Figure 2.13, the results (denoted by symbols) decay more slowly than those measured by the I-type hot-wire probe alone (solid line), even in the case of $s_1 = 0.50$ mm (denoted by downward triangle in Figure 2.13). The maximum measurement errors in this case are 14 % ($s_1 = 0.25$ mm), 8.8 % ($s_1 = 0.40$ mm), and 3.3 % ($s_1 = 0.50$ mm). This illustrates the blockage effect caused by the presence of the pressure probe near the hot-wire and implies that the velocity measured by the hot-wire is influenced by the pressure probe.

Figure 2.14 shows the axial variations of the streamwise mean velocity for $s_1 = 0.25$ mm, 0.40 mm, and 0.50 mm when s_2 is fixed to 1.0 mm. The ordinate, abscissa, solid lines, and symbols have the same definitions as in Figure 2.13. The results shown in Figure 2.14 (denoted by symbols) show a faster decay than those shown in Figure 2.13. The maximum measurement errors in this case are 8.2 % ($s_1 = 0.25$ mm), 5.7 % ($s_1 = 0.40$ mm), and 3.6 % ($s_1 = 0.50$ mm). However, these results differ only slightly from the results obtained using an I-type hot-wire probe alone. This indicates that the problem of the blockage effect caused by the presence of the pressure probe remains unsolved even in this arrangement.

Figure 2.15 shows the axial variations of the streamwise mean velocity in the cases of $s_1 = 0.25$ mm, 0.40 mm, and 0.50 mm when s_2 is fixed to 2.0 mm. The definitions of the ordinate and abscissa as well as the meanings of the solid line and symbols, are the same as those in Figure 2.13. As seen in Figure 2.15, all the results (denoted by symbols) are in good agreement with those measured by the I-type hot-wire probe alone (solid line). The maximum measurement errors in this case are 3.1 % ($s_1 = 0.25$ mm), 2.6 % ($s_1 = 0.40$ mm), and 1.2 % ($s_1 = 0.50$ mm). Therefore, there is almost no blockage effect from the pressure probe. This means that the streamwise spatial gap s_2 becomes an essential parameter for avoiding the blockage effect caused by the pressure probe.

Figure 2.16 shows the cross-streamwise profiles of the RMS values of the streamwise velocity fluctuation u' in the cases of $s_1 = 0.25$ mm and 0.50 mm when s_2 is fixed to 2.0 mm. The abscissa is x_2/b, and the ordinate is u'/u'_c, where u'_c is the RMS value of the streamwise velocity fluctuation on the jet centerline and b is the half-width of the cross-streamwise profile of the mean streamwise velocity. (Note that the variation of the half-width b was given in a previous paper (Sakai et al. 2006)). A solid line denotes the results measured by the I-type hot-wire probe alone. Figure 2.16 shows that the results (denoted by symbols) are in good agreement with those measured by the I-type hot-wire probe alone. The maximum measurement errors in this case are 1.3 % ($s_1 = 0.25$ mm) and 1.2 % ($s_1 = 0.50$ mm) for the inner region of the jet ($-1.4 \leq x_2/b \leq 1.4$). Therefore,

the effect of gap s_1 is very small in case $s_1 = 0.50$ mm.

Figure 2.17 shows the cross-streamwise profiles of the RMS values of the pressure fluctuation p' in the case of $s_1 = 0.25$ mm and 0.50 mm when s_2 is fixed to 2.0 mm. The abscissa is x_2/b, and the ordinate is p'/p'_c, where p'_c is the RMS value of the pressure fluctuation on the jet centerline. The solid line shows the results measured by the pressure probe alone (i.e., without an I-type hot-wire probe). As seen in Figure 2.17, the results (denoted by symbols) are in good agreement with those measured by the pressure probe alone. The maximum measurement errors in this case are 1.9 % ($s_1 = 0.25$ mm) and 1.8 % ($s_1 = 0.50$ mm) for the inner region of the jet (-1.4 $\leq x_2/b \leq$ 1.4).

From the above preliminary experiments, it is concluded that no noticeable interference is found between the signals observed by the pressure probe and the I-type hot-wire probe with $s_1 = 0.50$ mm and $s_2 = 2.0$ mm. On the basis of these results, the newly arranged combined probe is designed, as shown in Figure 2.18 and Figure 2.19. The pressure probe is placed between two hot-wires that comprise the X-type hot-wire sensor for the measurement of two velocity components. The diameter of the hot-wire is 5.0 μm, and its length is 1.0 mm. Note that in contrast with the previous combined probe, shown in Figure 2.20 (Sakai et al. 2010), the measurement points of the pressure probe and X-type hot-wire probe are strictly at the same location in the spanwise (x_3) direction. From this configuration of the combined probe, the spanwise spatial error of the measurement can be removed.

However, there is still a slight gap (s_2 in Figure 2.12) in the streamwise direction; therefore, the pressure fluctuation signal measured by the pressure probe has a slight time lag with respect to the velocity fluctuation signal measured by the X-type hot-wire probe. Therefore, the pressure fluctuation signal is corrected using Taylor's hypothesis given as

$$\tau = \frac{s_2 + s_3}{U(t)} = \frac{0.00325}{U(t)} \tag{2.11}$$

where τ is the time delay between the pressure fluctuation signal and the velocity fluctuation signal, $U(t)$ is the instantaneous streamwise velocity measured by the X-type hot-wire probe, and s_3 is the distance (1.25 mm) between the tip of the pressure probe and the pressure holes on the downstream side (see Figure 2.1).

In addition, the measurement error of the pressure fluctuation caused by the cross-flow error (see Figures 2.7 and 2.8) is completely corrected on the basis of flow angle data obtained from the instantaneous velocity measured by using the X-type hot-wire probe, except for the error caused by the cross flow provided by the spanwise (x_3) velocity.

However, the time variation RMS value of the cross-flow angle provided by these velocities in this plane jet is less than 6°. Therefore, the measurement error caused by the cross flow is considered to be less than 8 %.

In the following section, the results measured using the new combined probe are described and discussed for the plane jet, as shown in Figure 2.11. The resolution of this combined probe is noteworthy. In previous experiments, for the same plane jet [66], the Taylor transverse and Kolmogorov microscales in the jet's self-preserving region were approximated to be 3.0 mm and 0.1 mm, respectively. Therefore, on the basis of the diameter and arrangement of this combined probe, the spatial resolution for measurements of the velocity and pressure fluctuations is considered to be larger than the Kolmogorov microscale but smaller than the Taylor transverse microscale. This consideration is derived by using George's approach [58], which estimated the spatial resolution of the pressure probe to be the distance of the sensing holes from the tip of the tube or five times the probe diameter.

2.3 Simultaneous measurement of velocity and pressure in a plane jet

2.3.1 Velocity and pressure fileds

Figure 2.21 shows the cross-streamwise profiles of the mean streamwise velocity $\overline{U}$. The abscissa is x_2/b, and the ordinate is $\overline{U}/\overline{U_c}$, where $\overline{U_c}$ is the mean streamwise velocity on the jet centerline ($x_2/b = 0$). The measurements are performed at $x_1/d = 20$, 30, and 40. The solid line indicates the Gaussian Profile.

Figure 2.22 shows the cross-streamwise profiles of the RMS values of the streamwise velocity fluctuation u'. The abscissa is x_2/b, and the ordinate is u'/u'_c, where u'_c is the RMS value of the streamwise velocity fluctuation on the jet centerline. These measurements are performed at $x_1/d = 20$, 30, and 40. The solid line indicates the measured results ($x_1/d = 40$) obtained by Sakai et al. [97][98], who performed the simultaneous measurement of pressure and two velocity components (i.e., streamwise and cross-streamwise components) using the previous combined probe shown in Figure 2.20.

Figure 2.23 shows the cross-streamwise profiles of the RMS values of the pressure fluctuation p'. The ordinate is p'/p'_c, and the abscissa and the meaning of the solid line are the same as those in Figure 2.22. The measurements are performed at $x_1/d = 20$, 30, and 40.

Figure 2.24 shows the cross-streamwise profiles of the Reynolds stress -$\overline{uv}$. The ordinate is the Reynolds stress normalized by the product of u'_c and v'_c, where v'_c is the RMS value of the cross-streamwise velocity fluctuation on the jet centerline. The abscissa and the meaning of the solid line are the same as those in Figure 2.22. The measurements are performed at x_1/d = 20, 30, and 40.

The downstream variations of the spectrum E_{uu} of the streamwise velocity fluctuation u at x_2/b = 1.0 are shown in Figure 2.25. The ordinate is normalized by the turbulent energy dissipation ε per unit mass and the kinematic viscosity ν. The abscissa is the axial wavenumber k_1 normalized by the Kolmogorov microscale η. It should be noted that ε and η are estimated on the basis of the assumption of isotropic turbulence, as follows.

$$\varepsilon = 2\nu \int_0^\infty k^2 E(k) dk \tag{2.12}$$

$$\eta = \left(\frac{\nu^3}{\varepsilon}\right)^{\frac{1}{4}} \tag{2.13}$$

where $E(k)$ is the three-dimensional power spectrum of u, which is calculated from the one-dimensional power spectrum $E_1(k_1)$ as

$$E(k) = \frac{1}{2}\left[k_1^3 \frac{d}{dk_1}\left\{\frac{1}{k_1}\frac{d}{dk_1}E_1(k_1)\right\}\right]_{k_1=k} \tag{2.14}$$

$E_1(k_1)$ is calculated from the one-dimensional Eulerian frequency spectrum $E_1(f)$ by using Taylor's hypothesis. The measurements are performed at x_1/d = 20, 30, and 40. It should be noted that the upper limit of the frequency shown in the spectrum distribution corresponds to the Nyquist frequency of 5 kHz. Figure 2.25 shows the region that obeys Kolmogorov's five-thirds power law.

The downstream variations of the spectrum E_{pp} of the pressure fluctuation p at x_2/b = 1.0 are shown in Figure 2.26. The ordinate is normalized by the turbulent energy dissipation ε per unit mass, the kinematic viscosity ν, and the density ρ of the air. The abscissa is the same as that shown in Figure 2.25, but $E(k)$ in Equation (2.12) is the power spectrum of p. The measurements are performed at x_1/d = 20, 30, and 40. Figure 2.26 clearly shows the region with the seven-thirds power law.

From the measured results discussed above (Figures 2.21-2.26), it is found that the data obtained by the new combined probe are in good agreement with the previous results of Sakai et al. [97][98]. Therefore, the validity of the measurement apparatus is confirmed.

2.3.2 Estimation of the turbulent energy budget

The transport equation of the turbulent energy for a plane jet can be written as follows.

$$U\frac{\partial k}{\partial x_1} + V\frac{\partial k}{\partial x_2} + \overline{uv}\frac{\partial U}{\partial x_2} + (\overline{u^2} - \overline{v^2})\frac{\partial U}{\partial x_1} + \hat{\varepsilon} + \frac{\partial}{\partial x_2}(\frac{1}{2}\overline{vq^2} + \frac{1}{\rho}\overline{vp}) = 0 \tag{2.15}$$

where, k and $\hat{\varepsilon}$ are given by

$$k = \frac{\overline{q^2}}{2} = \frac{1}{2}\overline{\boldsymbol{u}\cdot\boldsymbol{u}} = \frac{1}{2}(\overline{u^2} + \overline{v^2} + \overline{w^2}) \tag{2.16}$$

$$\hat{\varepsilon} = \nu\overline{\frac{\partial u_i}{\partial x_j}^2} = \frac{1}{2}(\varepsilon_{\mathrm{i}} + \varepsilon_{\mathrm{j}} + \varepsilon_{\mathrm{k}}) \tag{2.17}$$

$$\varepsilon_i = 2\nu(\overline{\frac{\partial u_i}{\partial x_1}^2} + \overline{\frac{\partial u_i}{\partial x_2}^2} + \overline{\frac{\partial u_i}{\partial x_3}^2}) \tag{2.18}$$

Each subscript of ε_{i} (i = 1, 2, 3) corresponds to a component of the velocity fluctuation (i.e., u, v, and w). Moreover, the diffusion term in Equation (2.15) is expressed as

$$\frac{\partial}{\partial x_2}(\frac{1}{2}\overline{vq^2} + \frac{1}{\rho}\overline{vp}) = \frac{\partial}{\partial x_2}(\frac{\overline{u^2v} + \overline{v^3} + \overline{vw^2}}{2}) + \frac{\partial}{\partial x_2}(\frac{1}{\rho}\overline{vp}) \tag{2.19}$$

where the first term is the turbulent diffusion term, and the second term is the pressure diffusion term. The triple correlation vw^2 in the turbulent diffusion term can be measured by rotating the combined probe, as shown in Figure 2.27. In particular, by the rotating the combined probe through 45° around the streamwise axis (x_1), the output of the X-type hot-wire probe is made proportional to $(v+w)/\sqrt{2}$ [99], and then vw^2 can be estimated as

$$\overline{vw^2} = \frac{\overline{(v+w)^3} - \overline{v^3}}{3} \tag{2.20}$$

on the assumption that $\overline{w}$ is equal to zero. Furthermore, the turbulent energy k is calculated from Equation (2.21) on the assumption that $\overline{vw}$ is equal to zero.

$$k = \frac{\overline{u^2}}{2} + \frac{\overline{(v+w)^2}}{2} \tag{2.21}$$

Obviously, this rotation method of measurement has become useful only by miniaturizing the pressure probe and changing the spatial arrangement of the combined probe. By

this method, all terms of Equation (2.15) except the dissipation rate $\hat{\epsilon}$ can be measured directly. In this study, $\hat{\epsilon}$ can be estimated as the residual of Equation (2.15).

Figure 2.28 shows the cross-streamwise profiles of the RMS values of the streamwise, cross-streamwise, and spanwise velocity fluctuations u', v', and w' at $x_1/d = 40$. The abscissa is x_2/b, and the ordinates are u'/u'_c, v'/v'_c, and w'/w'_c, where, w'_c is the RMS value of the spanwise velocity fluctuation on the jet centerline. The results measured at the self-preserving region of the jet are denoted by a solid line and dashed line for $x_1/d = 40$ [100] and by a dot-dashed line for $x_1/d = 102$ [101]. As seen in Figure 2.28, the results measured by the new combined probe are in good agreement with those measured in previous studies. Therefore, the validity of this method of measurement is confirmed.

Figure 2.29 shows the turbulent energy budget of a plane jet at $x_1/d = 40$. The meanings of the symbols in Figure 2.29 are as follows; open circle denotes the convection term, which is the summation of the first and second terms in Equation (2.15); open triangle denotes the production term, which is the summation of the third and fourth terms in Equation (2.15); open diamond denotes the dissipation term, which is the fifth term in Equation (2.15); and open downward triangle denotes the diffusion term, which is the sixth term in Equation (2.15). The abscissa is x_2/b, and the ordinate is the value of each term normalized by $\overline{U_c}^3/b$. The solid and the dashed lines indicate the convection and the production terms estimated by Sakai et al. [97][98]), respectively. Figure 2.29 shows that the convection term (open circle) and the production term (open triangle) are in good agreement with the results measured by Sakai et al. [97][98].

Figure 2.30 shows only the dissipation and the diffusion term in Equation (2.15) at $x_1/d = 40$. The meanings of the symbols in Figure 2.30 are the same those in Figure 2.29. The solid and the dashed line indicate the dissipation and the diffusion terms estimated by Sakai et al. [97][98], respectively, and the dash-dot and the dash-dot-dot line indicate the dissipation and the diffusion terms estimated by Bradbury [102], respectively. Figure 2.30 shows that the diffusion term (open downward triangle) has a minimum within $0.5 \leq x_2/b \leq 0.6$ and a maximum at $x_2/b = 1.5$; therefore, although some quantitative difference can be still observed, the profile of the diffusion term is more similar to that of Bradbury (1965) than that of Sakai et al. [97][98]. Because of the difference in the profile of the diffusion term (open downward triangle), the profile of the dissipation term (open diamond) also changes and is more similar to that of Bradbury [102] than that of Sakai et al. [97][98].

For further discussion, the turbulent diffusion term and the pressure diffusion term in Equation (2.15) are estimated separately and compared with the data obtained by Sakai

et al. [97][98]. The results are shown in Figure 2.31. The meanings of the symbols in Figure 2.31 are as follows; open rightward triangle denotes the turbulent diffusion term, which is the first term in Equation (2.19); open leftward triangle denotes the pressure diffusion term, which is the second term in Equation (2.19); and open downward triangle denotes the total diffusion term, which is the summation of the turbulent diffusion term and the pressure diffusion term. The solid line indicates the turbulent diffusion term, and the dashed line indicates the pressure diffusion term which were estimated by Sakai et al. [97][98]. As seen in Figure 2.31, the pressure diffusion term (open leftward triangle) agrees with that of Sakai et al. [97][98]. However, the profile of the turbulent diffusion term (open rightward triangle) has a minimum at $x_2/b = 0.5$ and a maximum at $x_2/b = 1.5$ and thus differs from that of Sakai et al. [97][98]. Therefore, the difference in the distribution of the total diffusion term is due to the difference in the profile of the turbulent diffusion term. Furthermore, the integrated value of the diffusion term (i.e., the summation of the diffusion of the turbulent energy), which theoretically should be zero [102], is estimated over the cross section as follows.

$$\frac{b}{\overline{U_c^3}} \int_0^\infty \frac{\partial}{\partial x_2} \left(\frac{1}{2} \overline{vq^2} + \frac{1}{\rho} \overline{vp} \right) dx_2 \tag{2.22}$$

The integrated value of the diffusion term in the present study is -0.037 and is thus closer to zero than that in the previous study (-0.081 [97][98]). From these results mentioned above, it is concluded that a highly accurate estimate of the turbulent energy budget can be achieved with the newly arranged combined probe.

2.3.3 Cross-correlation coefficient in the intermittent region

Velocity and pressure are simultaneously measured in the intermittent region of a plane jet to obtain more understanding of the entrainment process. In this experiment, an I-type hot-wire probe (hereafter called a "detector") is installed in the intermittent region ($x_2/b = 1.315$) of the jet to distinguish the flow state of the region, and the velocity and pressure are simultaneously measured at $x_2/b = 1.3$ using our combined probe, as shown in Figure 2.32.

The flow state is distinguished by applying the method proposed with reference to Hedley et al. [103] and Koso et al. [10] to the signal obtained by the detector. First, we calculate the first-order time derivative of the velocity data $U(t)$ obtained by using the

detector.

$$| \dot{U}(t) | = | \frac{\partial}{\partial t}(U(t)) | \tag{2.23}$$

Next, we calculate the second-order time derivative as follows.

$$| \ddot{U}(t) | = | \frac{\partial}{\partial t} | \dot{U}(t) || \tag{2.24}$$

The phase of the second-order time derivative is then shifted 90° and the sum of the first-order and second-order time derivatives is obtained as follows. The sum is defined as a discriminant function $D(t)$.

$$D(t) = \frac{1}{2}(| \dot{U}(t) | + \frac{\sqrt{\overline{\dot{U}(t)}^2}}{\sqrt{\overline{\ddot{U}(t)}^2}}) \tag{2.25}$$

Next, we smoothen the discriminant function $D(t)$ by applying a 500-Hz low-pass filter and obtain the criterion function defined as $\hat{D}(t)$. Finally, we determined the intermittency function $I(t)$ (0: Non-turbulent state, 1: Turbulent state) using $\hat{D}(t)$ to have a threshold of 0.05 m/s^2. The functioning of the low-pass filter and the threshold measurement are validated by comparing the intermittency factor obtained by $I(t)$ with that obtained in a previous study [101].

Figures 2.33 and 2.34 show the cross-correlation coefficient $R_{\mathrm{vp_1}}$ and $R_{\mathrm{vp_2}}$ between the fluctuating cross-streamwise velocity v and the pressure p at $x_1/d = 40$, respectively. The cross-correlation coefficient $R_{\mathrm{vp_1}}$ and $R_{\mathrm{vp_2}}$ are defined by using the following equations:

$$R_{\mathrm{vp_1}} = \overline{v(t_1)p(t_1+\tau)}/(v'_{\mathrm{c}}p'_{\mathrm{c}}) \tag{2.26}$$

$$R_{\mathrm{vp_2}} = \overline{v(t_2)p(t_2+\tau)}/(v'_{\mathrm{c}}p'_{\mathrm{c}}) \tag{2.27}$$

where the over-bar and prime symbol (') denote the ensemble average and RMS value, respectively. t_1 is the time that $I(t)$ changes from 0 to 1 and t_2 is the time that $I(t)$ changes from 1 to 0. The time delay τ is normalized by the integral time scale T_{uI} of the streamwise velocity u. Here, a negative value of τ indicates that t_1 or t_2 has elapsed and a positive value of τ indicates that t_1 or t_2 has not elapsed.

Figure 2.33 shows that the sign of p changes at around t_1. By considering the sign of v at t_1 to be positive (owing to the ejection of turbulent fluid to the outer region), it can be seen that the sign of p will be negative at $\tau > 0$ and positive at $\tau < 0$. Further, Figure 2.34 shows that the sign of p changes around time t_2. As considering the sign of v is

negative (owing to the entrainment of non-turbulent fluid to the inner region), it is seen that the sign of p will be negative at $\tau < 0$ and positive at $\tau > 0$.

These results support the model of the vortex structure suggested in previous studies (Browne et al. [81], Tanaka et al. [104], Sakai et al. [66]), which is shown in Figure 2.35.

2.4 Conclusions

In this chapter a new combined probe for measuring instantaneous pressure and two velocity components simultaneously was developed. The combined probe consists of an X-type hot-wire and a newly devised pressure probe. The pressure probe was miniaturized by using a 0.1-inch microphone and the tip of the pressure probe was shaped into a hemisphere similar to that of the pitot tube. First, we checked the accuracy of the pressure fluctuation in turbulent flows by using the new pressure probe. Then, we carefully examined the effect of the spatial arrangement of the hot-wire probe and the pressure probe, and investigated the measurement accuracy of the new combined probe in a plane jet. Finally, we estimated the turbulent energy budget and the velocity-pressure cross-correlation coefficient in the intermittent region of the plane jet. The results are summarized as follows.

1. When the newly devised pressure probe was used, the measurement errors of the pressure fluctuation were 0 % - 10 % for a uniform flow.

2. No noticeable interference was observed between the signals with the pressure probe and the hot-wire sensor when the lateral distance (cross-streamwise distance) between the hot-wire sensor and the side wall of the pressure probe was set to 0.5 mm and when the longitudinal distance (streamwise distance) between the hot-wire sensor and the tip of the pressure probe was set to 2.0 mm. These values corresponded to approximately 0.17 times and 0.67 times the Taylor transverse microscale in the presently considered plane jet.

3. The results obtained by using the combined probe and the signal processing system were in good agreement with the reliable results obtained previously. Therefore, we conclude that this newly developed combined probe and the signal processing system were useful for the simultaneous measurements of the velocity and pressure.

4. The integral value of the total diffusion term (which should theoretically be equal to zero) was shown to be closer to zero compared with results reported previously

by Bradbury [102]. This is because the proposed combined probe and the signal processing system could measure the pressure diffusion $\overline{vp}$ and the triple correlation $\overline{vw^2}$ more accurately and directly than the probes used in previous studies.

5. The time-variation of the cross-correlation coefficient in the intermittent region supported the vortex structure model suggested by the results of previous studies (Browne et al. [81], Tanaka et al. [104], Sakai et al. [66]).

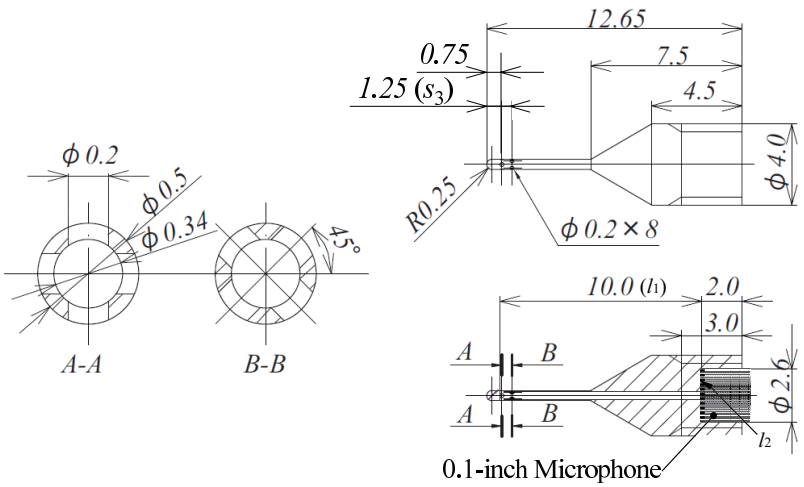

Figure 2.1 Schematic view of the new pressure probe (unit:mm).

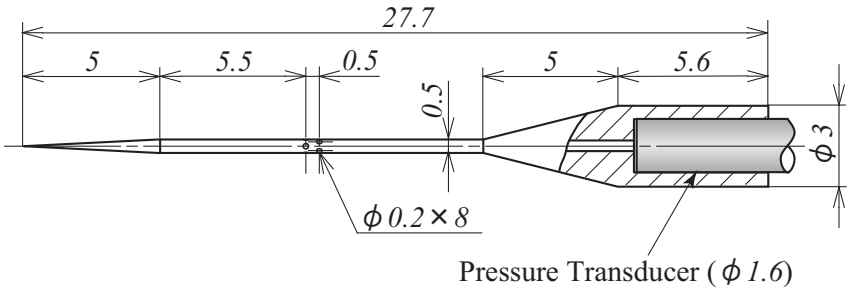

Figure 2.2 Schematic view of the previous pressure probe (unit:mm) [97][98].

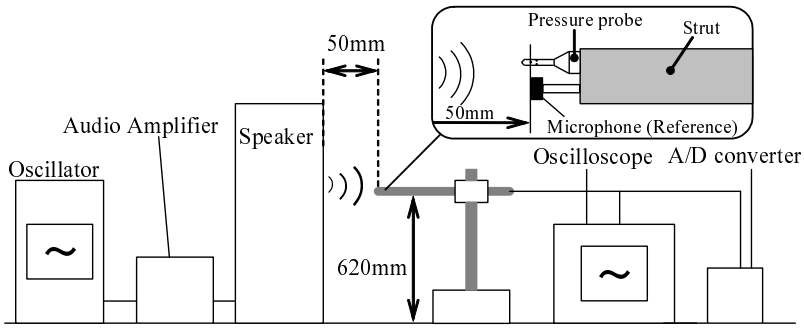

Figure 2.3 Experimental apparatus in the test of frequency response.

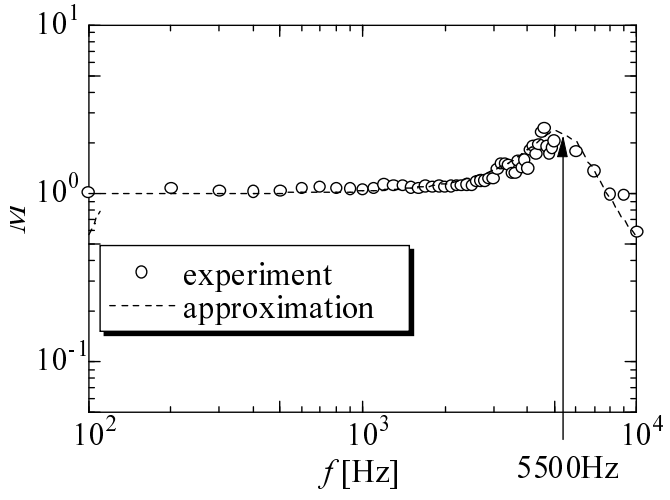

Figure 2.4 Amplitude ratio M in the test of frequency response.

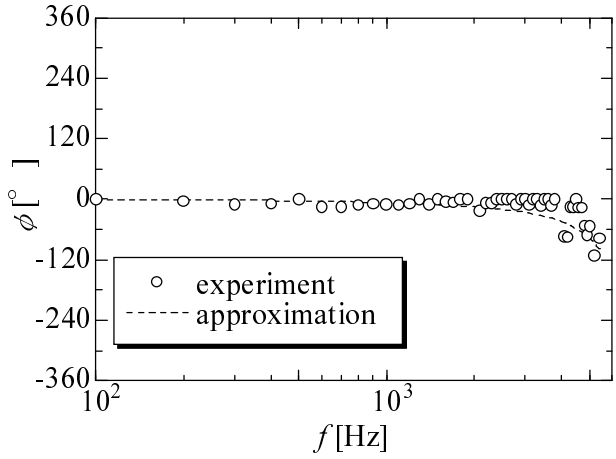

Figure 2.5 Phase difference φ in the test of frequency response.

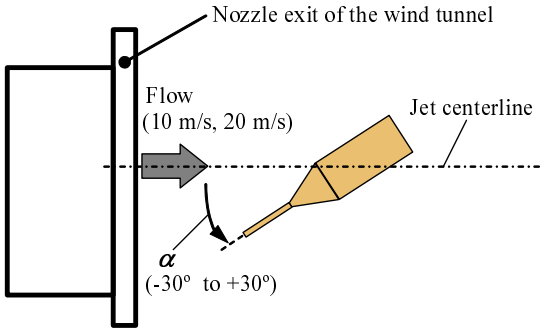

Figure 2.6 Experimental apparatus to check the cross-flow error of the pressure probe (not to scale).

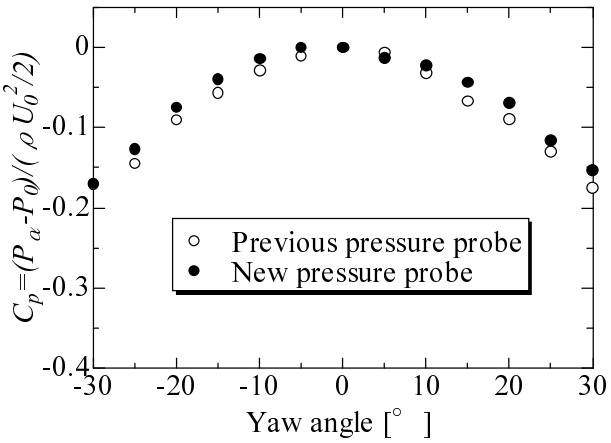

Figure 2.7 Cross-flow error of the pressure probe ($U_0 = 10$ m/s).

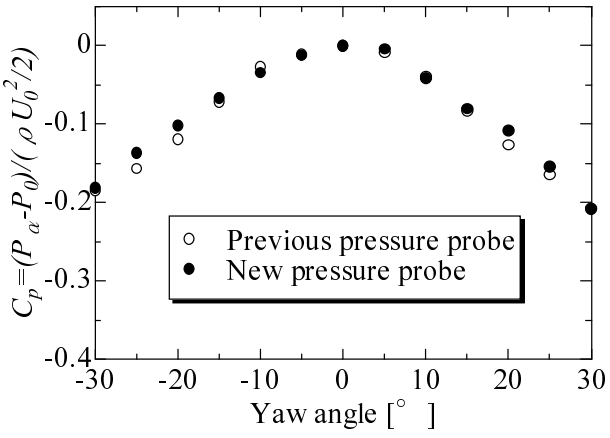

Figure 2.8 Cross-flow error of the pressure probe ($U_0 = 20$ m/s).

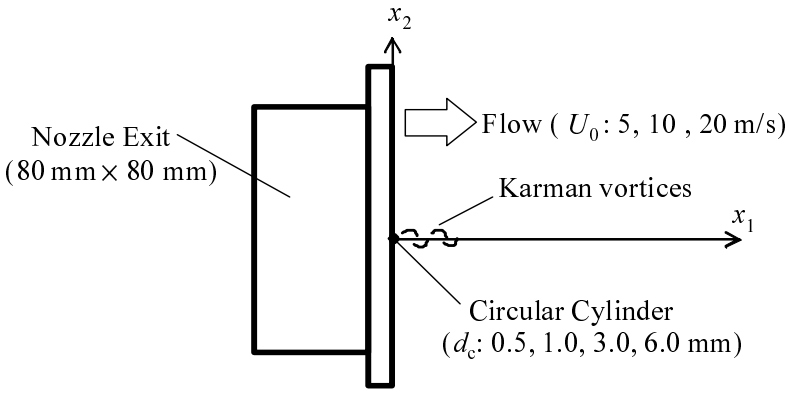

Figure 2.9 Measurement apparatus for the calibration.

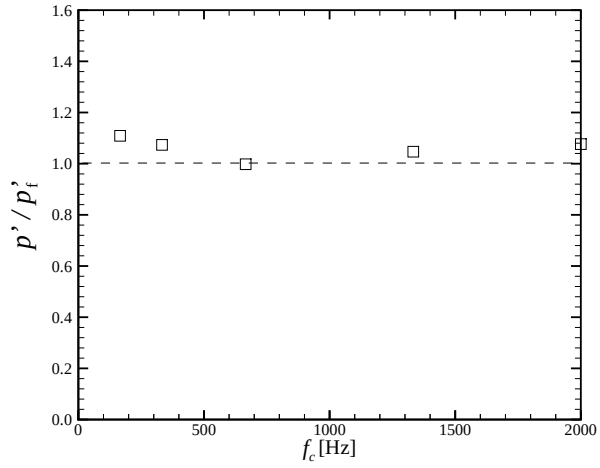

Figure 2.10 Ratio of the RMS value of the measured pressure fluctuation p' and that of predicted value p'_f.

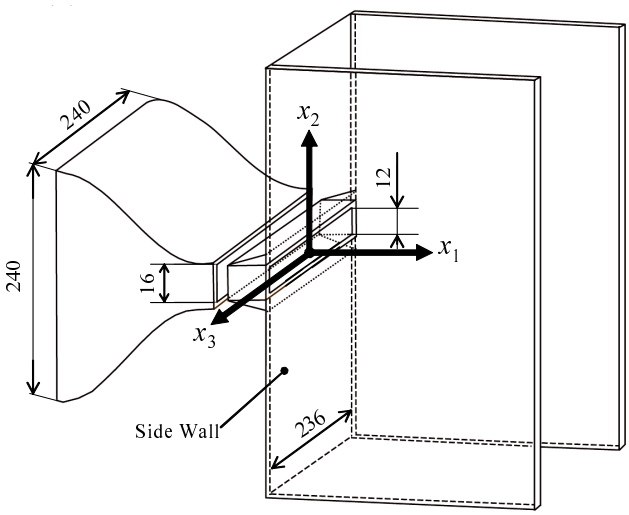

Figure 2.11 Experimental apparatus of plane jet (unit:mm).

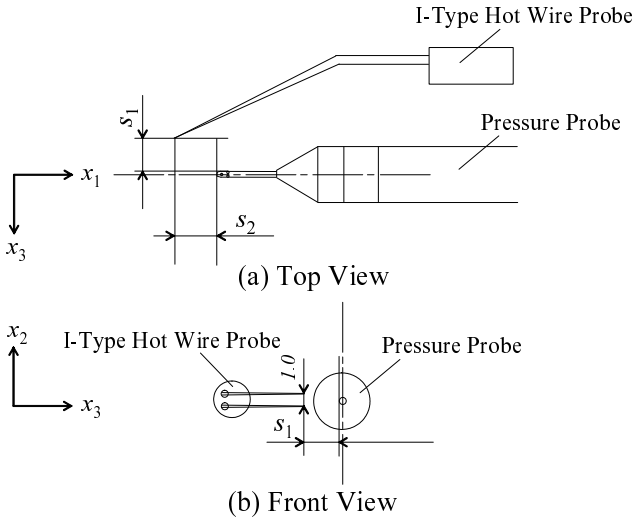

Figure 2.12 Schematic view of the I-type hot-wire probe and the new pressure probe (unit:mm).

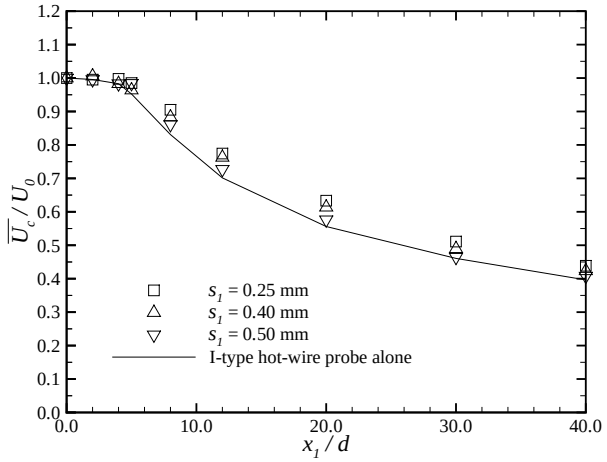

Figure 2.13 Axial variation of the jet centerline mean streamwise velocity $\overline{U_c}$. $s_1 = 0.25$, 0.40, and 0.50 mm, and s_2 is fixed to 0.0 mm. The solid line shows the results measured by the I-type hot-wire probe alone.

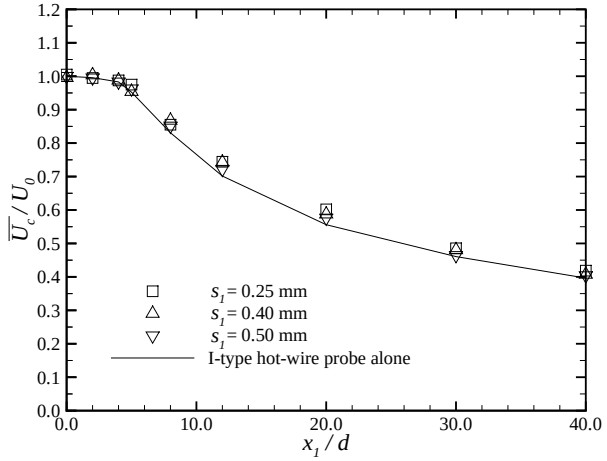

Figure 2.14 Axial variation of the jet centerline mean streamwise velocity $\overline{U}_c/U_0$. s_1 = 0.25, 0.40, and 0.50 mm, and s_2 is fixed to 1.0 mm. The solid line shows the results measured by the I-type hot-wire probe alone.

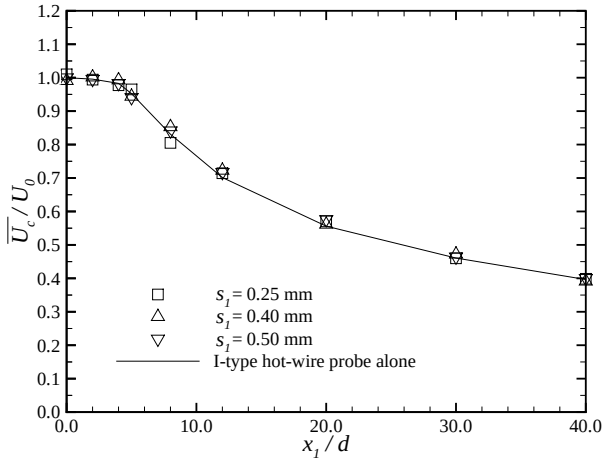

Figure 2.15 Axial variation of the jet centerline mean streamwise velocity $\overline{U_c}$. $s_1 = 0.25$, 0.40, and 0.50 mm, and s_2 is fixed to 2.0 mm. The solid line shows the results measured by the I-type hot-wire probe alone.

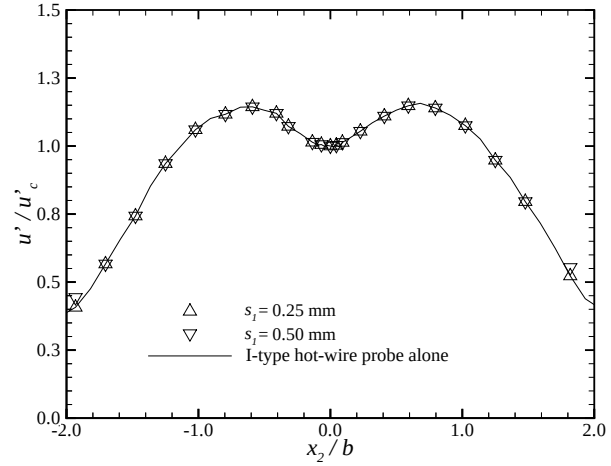

Figure 2.16 Cross-streamwise profiles of u'. $s_1 = 0.25$ mm and 0.50 mm, and s_2 is fixed to 2.0 mm. The solid line shows the results measured by the I-type hot-wire probe alone.

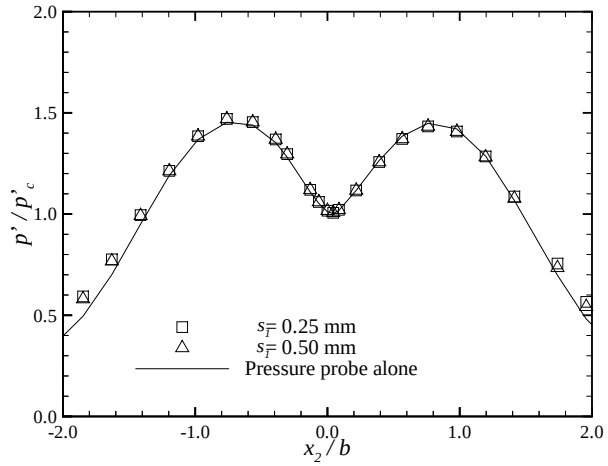

Figure 2.17 Cross-streamwise profiles of p'. $s_1 = 0.25$ mm and 0.50 mm, and s_2 is fixed to 2.0 mm. The solid line shows the results measured by the pressure probe alone.

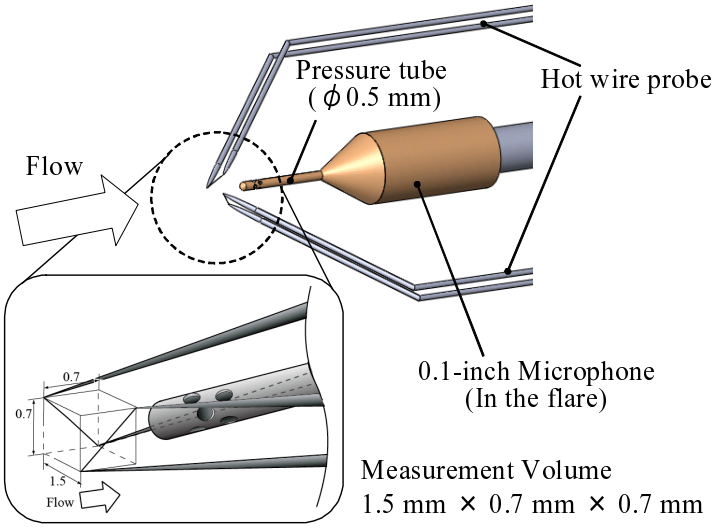

Figure 2.18 Schematic view of the newly arranged combined probe (Diagrammatic erspective view. unit:mm).

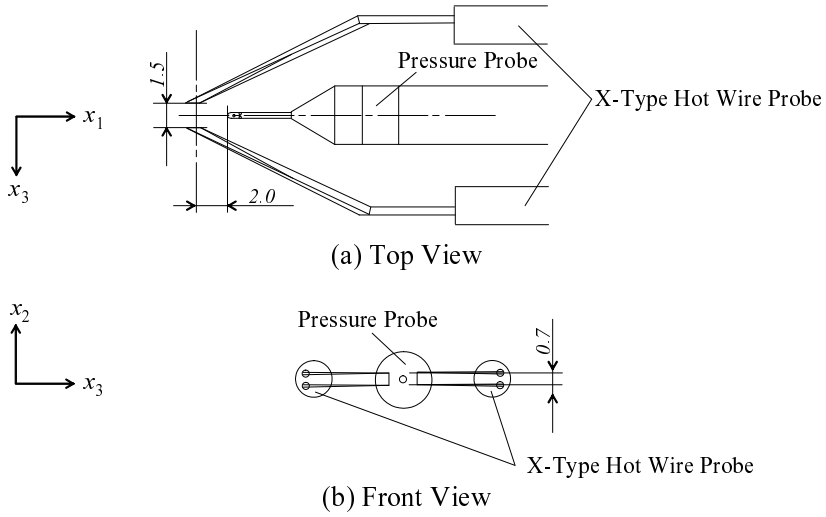

Figure 2.19 Schematic view of the newly arranged combined probe (Top view and front view. unit:mm).

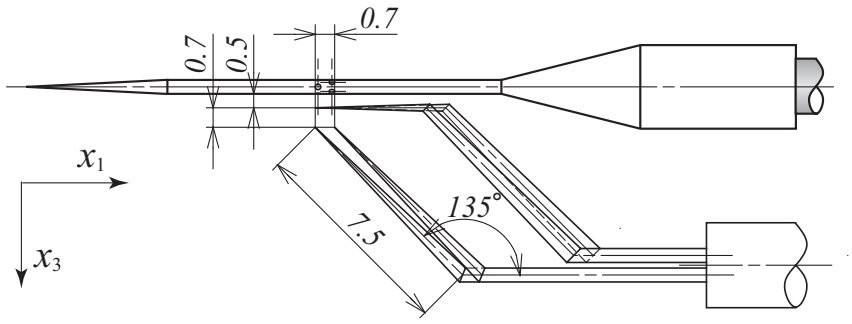

Figure 2.20 Schematic view of the previous combined probe (unit:mm) [97][98].

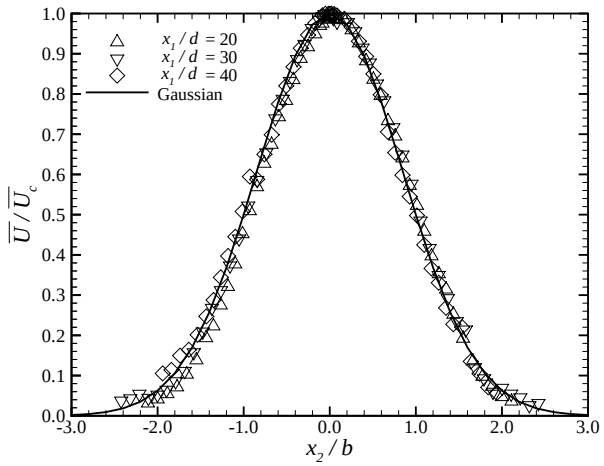

Figure 2.21 Cross-streamwise profiles of the mean streamwise velocity $\overline{U}$.

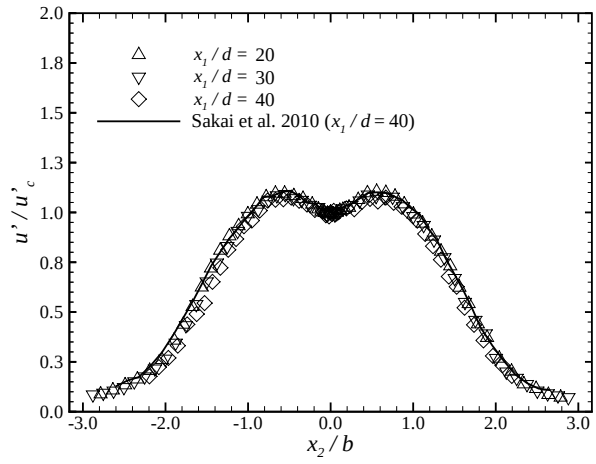

Figure 2.22 Cross-streamwise profiles of the RMS values of the streamwise velocity fluctuation u'.

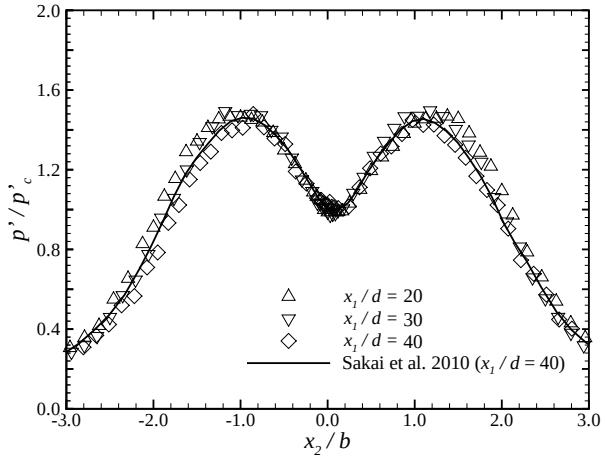

Figure 2.23 Cross-streamwise profiles of the RMS values of the pressure fluctuation p'.

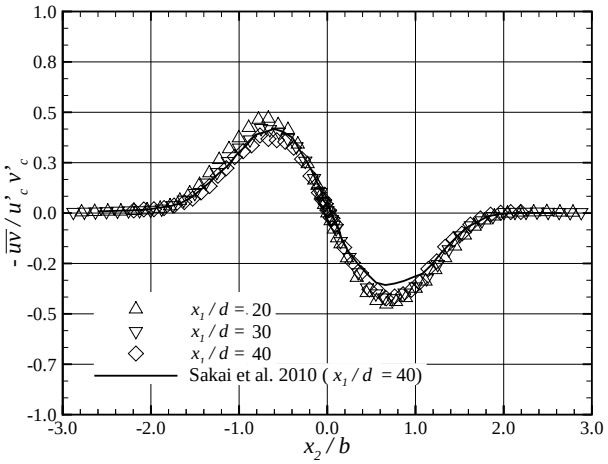

Figure 2.24 Cross-streamwise profiles of the Reynolds stress $-\overline{uv}$.

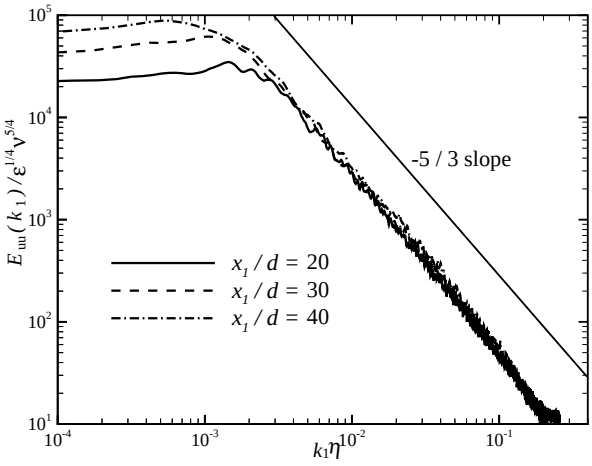

Figure 2.25 The downstream variation of the spectrum E_{uu} of the streamwise velocity fluctuation u at x_2/b=1.0.

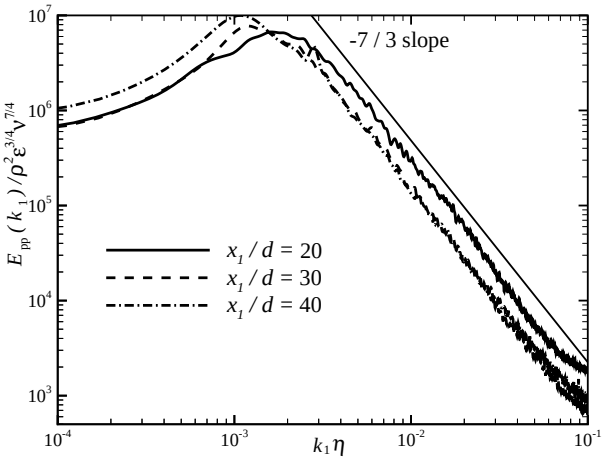

Figure 2.26 The downstream variation of the spectrum E_{pp} of the pressure fluctuation p at x_2/b=1.0.

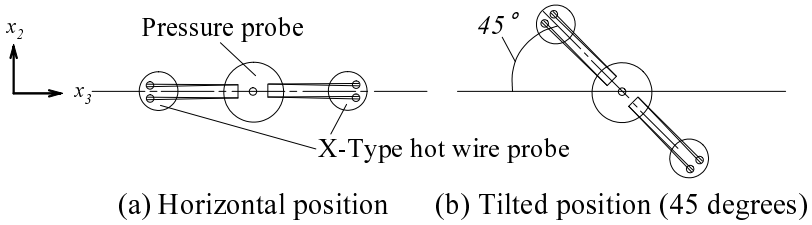

Figure 2.27 Front view of the combined probe, (a) horizontal position and (b) tilted position.

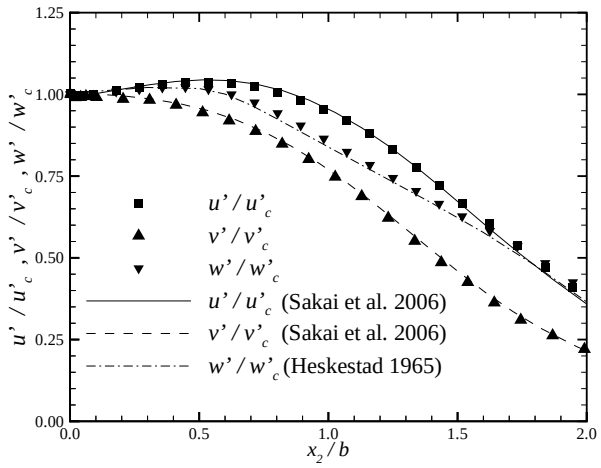

Figure 2.28 Cross-streamwise profiles of the RMS values of the streamwise, cross-streamwise, and spanwise velocity fluctuation at x_1/d=40.

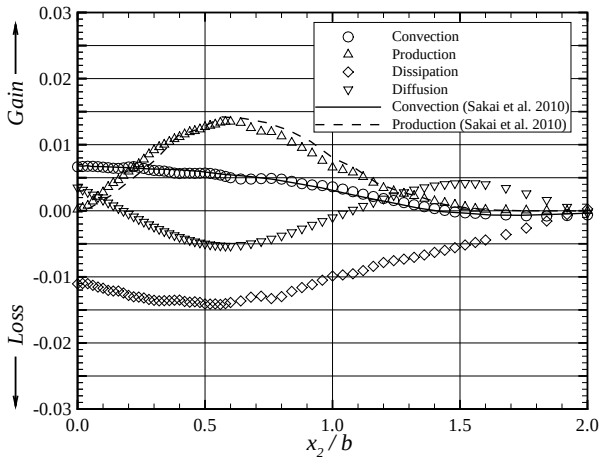

Figure 2.29 Turbulent energy budget at x_1/d=40.

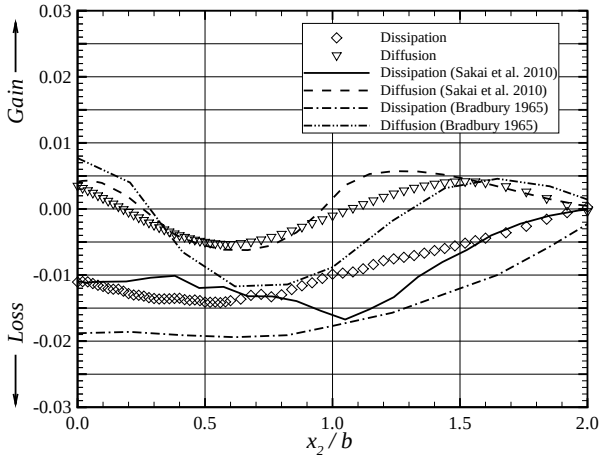

Figure 2.30 Dissipation and diffusion term at x_1/d=40.

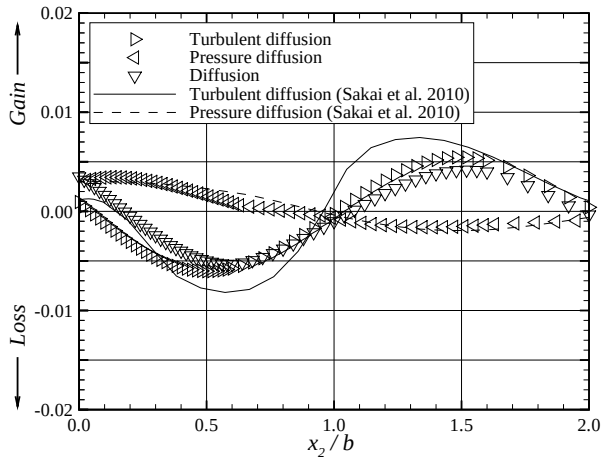

Figure 2.31 Diffusion terms in the turbulent energy budget at x_1/d=40.

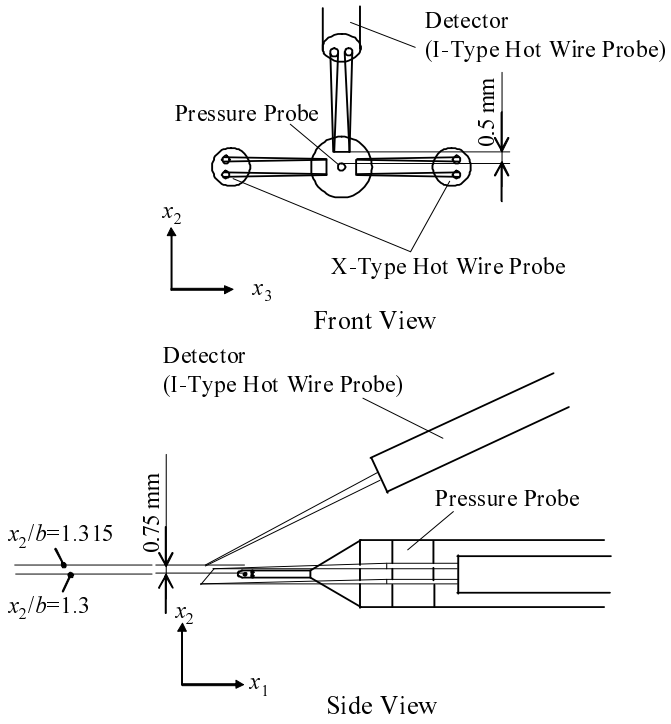

Figure 2.32 Spatial arrangement of combined probe and detector.

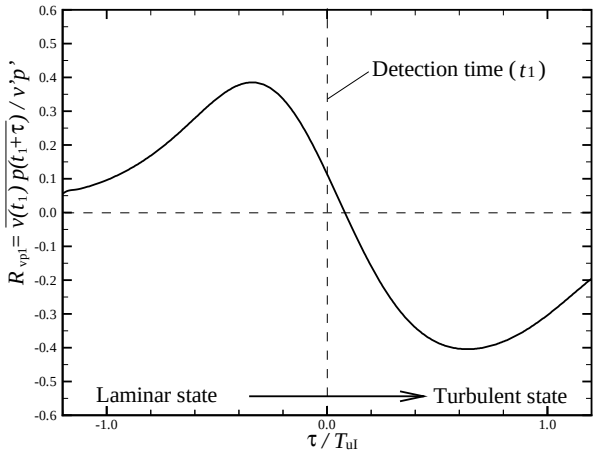

Figure 2.33 Cross-correlation coefficient R_{vp1} ($I(t)$: $0 \rightarrow 1$).

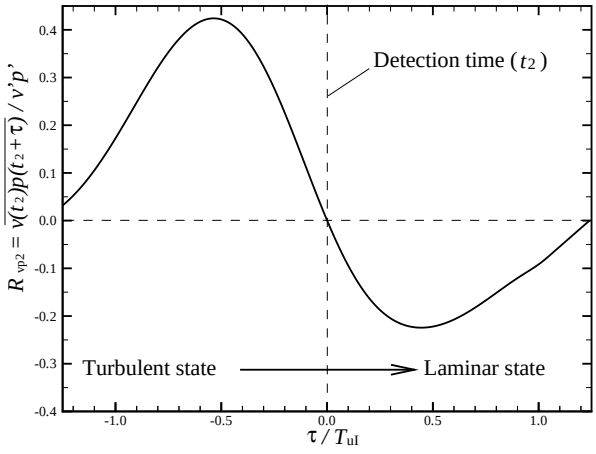

Figure 2.34 Cross-correlation coefficient R_{vp2} ($I(t)$: $1 \rightarrow 0$).

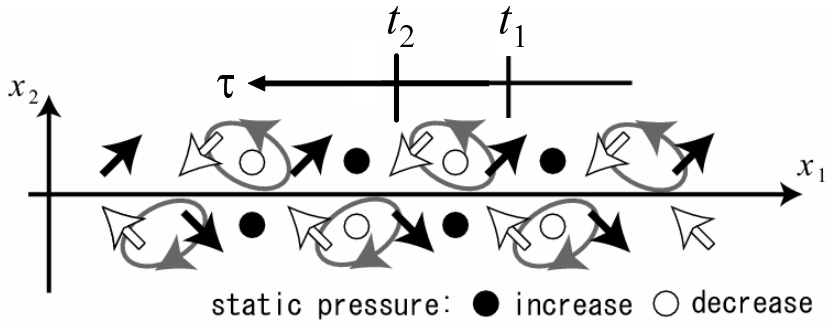

Figure 2.35 A model for the vortex structure of a plane jet (Browne et al. [81], Tanaka et al. [104], Sakai et al. [66]).

Chapter 3

Estimation of conditional averaged value and diffusion term in the intermittent region of a plane jet [105]

3.1 Introduction

In Chapter 2, a newly-devised combined probe for the simultaneous measurement of two components of the velocity and pressure in a plane jet was developed. Further, the turbulent energy budget of a plane jet was estimated and it was found that the accuracy of the simultaneous measurement was improved. In this chapter, with using the combined probe developed in Chapter 2, the simultaneous measurement of the velocity and pressure in a plane jet is performed again and the measured results are discussed from another point of view.

Firstly, for the more detail understanding of the flow phenomena in the intermittent region of a plane jet, the conditional ensemble-averaged statistics are investigated on the basis of the intermittency function obtained from the velocity signal by the hot-wire sensor set in the intermittent region of a plane jet. In the discussions, the changes of the profiles of the mean velocity, velocity fluctuation, Reynolds stress and pressure fluctuation are mainly placing the focus on. Further, the turbulent energy budget of a plane jet is also discussed.

Secondly, the validity of the models for the diffusion term is investigated. In this chapter, the validity of the Daly's model [42] and Shir's model [40] are investigated with using the data obtained by the combined probe. Further, the validation of the models for the rapid term [51] and the slow term [39] of the pressure diffusion process are also investigated.

3.2 Experimental setup and procedure

3.2.1 Experimental apparatus and conditions

The experiment is performed in a plane jet shown in Figure 2.11. The experimental apparatus, coordinate system and experiment conditions are the same with the experiment described in Chapter 2.

In this study, to obtain the conditional ensemble-averaged statistics, an I-type hot-wire probe (hereafter called as "detector") is installed in the intermittent region of the jet to distinguish the flow state of the region. Further, the velocity and pressure near the detector are simultaneously measured by the combined probe which was shown in Figure 2.32 in the previous chapter. The minimum gap between the hot-wire of the detector and the outer wall of the pressure probe is 0.5 mm. This value was determined in the preliminary experiment. The position of the combined probe is controlled by the traverse system which can make the positioning accuracy less than ± 0.1 mm (See Figure 3.1).

The sampling frequency of the combined probe and detector is 20 kHz and the number of sampling is 262,144 (about 13 seconds). In the preliminary experiments, it was confirmed that the sampling length is adequate to obtain the reliable turbulence statistics. The measured data are stored on the hard disk of a personal computer via an A/D converter and then the data are statistically analyzed.

3.2.2 Turbulent/non-turbulent decision

In this study, to distinguish the turbulent region from the non-turbulent region, the method proposed with reference to Hedley et al. [103] and Koso et al. [10] is applied to the signal obtained by the detector. The detail of the method was described in Chapter 2. So that only the image of the signal processing for turbulent or non-turbulent decision is shown in Figure 3.2.

3.3 Results and discussions

3.3.1 Base flow

The cross-streamwise profiles of the streamwise mean velocity $\overline{U}$, the RMS value of the streamwise velocity fluctuation u', the RMS value of the pressure fluctuation p', and the Reynolds stress -$\overline{uv}$ were shown in Figures 2.21, 2.22, 2.23, and 2.24 in Chapter 2,

respectively.

Figure 3.3 shows the cross-streamwise profiles of the intermittency factor γ. The ordinate indicates γ determined on the basis of the intermittency function $I(t)$ and the abscissa is the same as that in Figure 2.21. The solid line indicates the intermittency factor obtained by Heskestad [101]. The measurements are performed at $x_1/d = 20$, 30, and 40. In Figure 3.3, only the profile in the range $x_2/b \leq 0$ is shown because in the preliminary experiment (shown in Chapter 2), it was found that the velocity and pressure fields were symmetrical to $x_2/b = 0$. Figure 3.3 shows the similarity of the profiles and the profile corresponds with the result of Heskestad at $x_1/d = 40$. Therefore, the functioning of the low-pass filter and the threshold value in the turbulent/non-turbulent decision process are validated. Further, in the following, the detector is set at $x_2/b = 1.7$ where γ equals to 0.5.

3.3.2 Conditional ensemble-averaged statistics

Velocity and pressure field

Figure 3.4 shows the conditional ensemble-averaged value in the range $x_2/b \leq 0$. Figure 3.4 (a) shows the mean streamwise velocity, Figures 3.4 (b)-(e) show the RMS value of streamwise velocity fluctuation, cross-streamwise velocity fluctuation, spanwise velocity fluctuation and pressure fluctuation, respectively. Further, Figure 3.4 (f) shows the Reynolds stress. In these figures, the ordinate indicates the value normalized by the value on the jet centerline and the abscissa indicates x_2/b. The subscript of "T" and "NT" means the value when the flow state at the position of the detector is turbulent state and non-turbulent state, respectively. Measurements are performed at $x_1/d = 40$, $0 \leq x_2/b \leq 2.5$ and $x_3 = 0$. Spatial interval of the measurements is 0.05 times x_2/b. The spanwise velocity fluctuation w is obtained by rotating the combined probe 90 degrees on the jet centerline. The solid line, dashed line, and dot-dash line indicate the whole time averaged value, the conditional ensemble-averaged value when $I(t) = 1$ (denoted by the subscript of T) and the conditional ensemble-averaged value when $I(t) = 0$ (denoted by the subscript of NT), respectively.

Figure 3.4 shows that the profiles of the conditional ensemble-averaged value differ in the range $1.0 \leq x_2/b \leq 2.5$. The differences can be clearly found especially in the profile of the RMS value of the streamwise velocity fluctuation u' (Figure 3.4 (b)), spanwise velocity fluctuation w' (Figure 3.4 (d)), and Reynolds stress -$\overline{uv}$ (Figure 3.4 (f)).

Turbulent energy budget

The turbulent energy budget in a plane jet which was estimated in the last chapter is estimated again with using the conditional ensemble-averaged value. The estimation is performed in the same process described in the previous chapter.

Figures 3.5 (a)-(c) show the cross-streamwise profiles of convection term (sum of the first and second term in Equation (2.15)), production term (sum of the third and fourth term in Equation (2.15)), diffusion term (sixth term in Equation (2.15)), respectively. In this estimation, convection term (CT), production term (PT), and diffusion term (DT) are estimated as follows.

$$\mathrm{CT} = \overline{U_*}\frac{\partial k_*}{\partial x_1} + \overline{V_*}\frac{\partial k_*}{\partial x_2} \tag{3.1}$$

The production term (PT) is estimated by next equation.

$$\mathrm{PT} = \overline{u_* v_*}\frac{\partial \overline{U_*}}{\partial x_2} + (\overline{u_*^2} - \overline{v_*^2})\frac{\partial \overline{U_*}}{\partial x_1} \tag{3.2}$$

The diffusion term (DT) is estimated by next equation.

$$\mathrm{DT} = \frac{\partial}{\partial x_2}(\overline{v_* k_*} + \frac{1}{\rho}\overline{v_* p_*}) \tag{3.3}$$

Here, subscript of * shows the flow state T or NT. The ordinate indicates the value of each term normalized by $\overline{U_\mathrm{c}}^3/b$ and the abscissa indicates x_2/b. The solid line, dashed line, and dot-dash line indicate the whole time averaged value, the conditional ensemble-averaged value when $I(t) = 1$ (T) and the conditional ensemble-averaged value when $I(t) = 0$ (NT), respectively.

Figure 3.5 (a) shows that the profiles of the convection term whose role is the injection of the turbulent energy from the outer side of the jet to the inner side have difference in the range $x_2/b \geq 1.0$. When $I(t) = 1$, the injection of the turbulent energy can be observed in the wider area than that when $I(t) = 0$. Further, the profiles of the convection term are almost the same in the range $x_2/b \leq 0.6$. Therefore, it can be concluded that the constant injection of the turbulent energy to the inner side of the jet (which does not depend on the flow state of the intermittent region) takes place in this region.

Figure 3.5 (b) shows that the profiles of the production term whose role is the production of the turbulent energy have difference in the range $0 \leq x_2/b \leq 2.0$. Especially, the difference of positive peak value of the profiles around $x_2/b = 0.7$ is noticeable. The peak when the flow state is turbulent is higher than that when the flow state is non-turbulent. However, the integrated value of the production term to x_2 direction is almost the same

in these cases. Therefore, it can be concluded that the profile of the production term depends on the flow state in the intermittent region but the integrated value of the profile does not strongly depend on it.

Figure 3.5 (c) shows that the profiles of the diffusion term whose role is the transportation of the turbulent energy have difference in the range $0.8 \leq x_2/b \leq 2.0$. The transportation of the turbulent energy to the outer region of the jet is enhanced when the flow state in the intermittent region is turbulent and it becomes small when the flow state is non-turbulent.

Figure 3.6 (a)-(c) show the cross-streamwise profiles of dissipation term, turbulent diffusion term, pressure diffusion term, respectively. In this estimation, turbulent diffusion term is estimated as the first term of the diffusion term shown in Equation (3.3) and pressure diffusion term is estimated as the second term of it. Then, the dissipation term is estimated as a residual. The meanings of the ordinate, abscissa, solid line, dashed line, and dot-dash line are the same with Figure 3.5.

Figure 3.6 (a) shows that the dissipation of the turbulent energy in $x_2/b \leq 1.0$ becomes large when the flow state in the intermittent region is turbulent and it becomes small when the state is non-turbulent. Further, Figure 3.6 (b) shows that the profiles of turbulent diffusion show some difference which depends on whether the flow state in the intermittent region is turbulent or not. The transportation of the turbulent energy by turbulent diffusion is enhanced in the range $x_2/b \leq 1.0$ when the flow state is turbulent and it decreases when the flow state is non-turbulent as with the diffusion term shown in Figure 3.5 (c). On the other hand, Figure 3.6 (c) shows that the pressure diffusion has a little different characteristics and it does not strongly depend on the flow state. Therefore, the difference observed in Figure 3.5 (c) is caused by the difference of the turbulent diffusion. In addition, from the results shown above, it can be concluded that the transport of the turbulent energy from outer region of the jet to the inner region by the pressure diffusion does not depend on the flow state strongly. This may because the turbulent energy transport by the pressure diffusion mainly depends on the large-scale coherent vortex structures near the jet centerline but the ejection or entrainment which dominates the flow state in the intermittent region.

3.3.3 Validation of the turbulence models

Gradient diffusion model

The study on the models for the diffusion term included in the Reynolds stress transport equation and momentum equation have been performed by Rotta [106][107] and many researchers up to date.

In this study, the validity of the Gradient-Diffusion-Models which are one of the models for the diffusion process proposed by Daly & Harlow [42] and Shir [40] is discussed by using the measurement results of two velocity components and pressure in a plane jet. The details of the Gradient-Diffusion-Models will be shown in the following.

The exact equation for the evolution of Reynolds stress is expressed again as follows.

$$\frac{\mathrm{D}}{\mathrm{D}t}\overline{u_\mathrm{i}u_\mathrm{j}} + \frac{\partial}{\partial x_\mathrm{k}}\left(T^{\nu}_{\mathrm{kij}} + T^{p}_{\mathrm{kij}} + T^{u}_{\mathrm{kij}}\right) = P_\mathrm{ij} + R^{a}_\mathrm{ij} - \epsilon_\mathrm{ij} \tag{3.4}$$

Here, T^{ν}_{kij}, T^{p}_{kij}, and T^{u}_{kij} are viscous diffusion term, pressure diffusion term, and turbulent diffusion term, respectively and expressed as follows.

$$T^{\nu}_{\mathrm{kij}} = -\nu\frac{\partial\overline{u_\mathrm{i}u_\mathrm{j}}}{\partial x_\mathrm{k}} \tag{3.5}$$

$$T^{p}_{\mathrm{kij}} = \frac{2}{3}\delta_\mathrm{ij}\overline{u_\mathrm{k}p}/\rho \tag{3.6}$$

$$T^{u}_{\mathrm{kij}} = \overline{u_\mathrm{i}u_\mathrm{j}u_\mathrm{k}} \tag{3.7}$$

It should be noted that the viscous diffusion term T^{ν}_{kij} is negligible except in the viscous wall region.

Daly & Harlow [42] developed a model which uses the generalized gradient diffusion hypothesis for the triple correlation as follows.

$$T'_\mathrm{kij} = T^{p}_{\mathrm{kij}} + T^{u}_{\mathrm{kij}} = -C_\mathrm{sDH}\frac{k}{\epsilon}\overline{u_\mathrm{k}u_\mathrm{l}}\frac{\partial\overline{u_\mathrm{i}u_\mathrm{j}}}{\partial x_\mathrm{l}} \tag{3.8}$$

Here, C_sDH is a model constant, k is turbulent energy, ϵ is dissipation energy of turbulent energy per unit mass. k and ϵ are expressed as follows.

$$k \equiv \frac{\overline{q^2}}{2} = \frac{1}{2}\overline{\boldsymbol{u}\cdot\boldsymbol{u}} = \frac{1}{2}(\overline{u^2} + \overline{v^2} + \overline{w^2}) \tag{3.9}$$

$$\varepsilon = \hat{\varepsilon} + \nu\frac{\partial\overline{u_\mathrm{i}u_\mathrm{j}}}{\partial x_\mathrm{i}\partial x_\mathrm{j}} \tag{3.10}$$

$$\hat{\varepsilon} = \nu\overline{\frac{\partial u_\mathrm{i}}{\partial x_\mathrm{j}}^2} = \frac{1}{2}(\varepsilon_u + \varepsilon_v + \varepsilon_w) \tag{3.11}$$

They derived the transport equations, which describing the dynamics of transient flow of an incompressible fluid in arbitrary geometry in such a manner as to incorporate the principles of invariance and universality. Then, the applicability of the equations was demonstrated by comparison of solutions with experiments on turbulence distortion on the turbulence in the flow between flat plates. In their model, it was assumed that the effect of pressure diffusion term could be modeled into turbulent diffusion which was modeled as an expression shown in Equation (3.8). In related to this model, Launder [44] suggests the value of C_{sDH} equals to 0.22. In addition, the simplest gradient-diffusion-model for T'_{kij} due to Shir [40] is expressed as follows.

$$T'_{\mathrm{kij}} = -C_{\mathrm{sSH}} \frac{k^2}{\epsilon} \frac{\partial \overline{u_{\mathrm{i}} u_{\mathrm{j}}}}{\partial x_{\mathrm{k}}} \tag{3.12}$$

Here, C_{sSH} is a model constant. Shir developed this model to study atmospheric turbulence in the planetary boundary layer.

In this study, the model constants C_{sDH} and C_{sSH} can be estimated directly by using measurement results of the velocity and pressure. Therefore, the cross-streamwise profile of each model constant is estimated and the validation of the gradient-diffusion-model is investigated.

Figure 3.7 shows the cross-streamwise profile of the model constant C_{sDH} and C_{sSH} measured at $x_1/d = 40$. The ordinate shows the value of model constant C_{sDH} or C_{sSH} and the abscissa shows x_2/b.

Figure 3.7 shows that C_{sDH} is not equal to 0.22 which Launder proposed but it is almost constant in the range $0 \leq x_2 \leq 0.8$. Therefore, C_{sDH} can be assumed as a model constant in the inner region of the jet. One of the reasons for C_{sDH} is not to be constant in the outer region of the jet ($0.8 \leq x_2/b$) is that the contribution of the pressure diffusion to the diffusion process in the outer region becomes large (See Figure 3.5, 3.6) but Daly & Harlow model neglected the effect of the pressure diffusion.

Figure 3.7 also shows that C_{sSH} is almost constant in the range $0.4 \leq x_2/b \leq 1.2$ but it is not constant $x_2/b \leq 0.4$ and $x_2/b \geq 1.2$. The reason for C_{sSH} to be relatively constant in the outer region of the jet where C_{sDH} is not constant is that Shir model included the effect of pressure diffusion process explicitly. On the other hand, the reason for C_{sDH} not to be constant in the range $x_2/b \leq 0.4$ and $x_2/b \geq 1.2$ is considered to be the effect of the pressure diffusion process which is relatively weak near the jet centerline and the turbulent intermittency in the outer region of the jet.

From the results described above, it can be concluded that Daly & Harlow model is adequate for the flow filed where the effect of the pressure diffusion process is weak.

Further, Shir model is adequate for the flow field where the effect of the pressure diffusion process is relatively strong and the turbulent intermittency is small.

Models for rapid/slow term

In this section, the results of the validation of the models for the rapid/slow term of the pressure diffusion term is described.

In general, the velocity-pressure correlation term $\overline{u_\mathrm{l} p}$ included in the pressure diffusion term T^p_kij is divided into two parts named the rapid term and slow term [51].

$$\overline{u_\mathrm{l} p}/\rho = \frac{1}{2\pi}\frac{\partial \overline{u_\mathrm{m}}}{\partial x_\mathrm{n}}\int_V \frac{\overline{\partial u_\mathrm{n} u_\mathrm{l}}}{\partial r_\mathrm{m}}\frac{\mathrm{d}V}{|\underline{\mathrm{r}}|} + \frac{1}{4\pi}\int_V \frac{\partial^2 \overline{u_\mathrm{m} u_\mathrm{n} u_\mathrm{l}}}{\partial r_\mathrm{n}\partial r_\mathrm{m}}\frac{\mathrm{d}V}{|\underline{\mathrm{r}}|} \tag{3.13}$$

Here, the first term in the right hand side of Equation (3.13) is the rapid term (hereafter, called as T^p_R), the second term is the slow term (hereafter, called as T^p_S). T^p_R is modeled by Suga [51] as a linear function of both the Reynolds stress and a length-scale vector l_m expressed as follows.

$$T^p_\mathrm{R} = \frac{\partial \overline{u_\mathrm{m}}}{\partial x_\mathrm{n}}\gamma^\mathrm{nl}_\mathrm{m}(\overline{u_\mathrm{n} u_\mathrm{l}}, l_\mathrm{m}) \tag{3.14}$$

Here, $\gamma^\mathrm{nl}_\mathrm{m}$ is the third rank tensor whose general form satisfies the symmetry in the indexes n and l. Further, by applying the continuity and the TCL turbulence conditions, the Equation (3.14) can be written as follows.

$$\frac{\partial \overline{u_\mathrm{m}}}{\partial x_\mathrm{n}}\beta_1 k\left(l_\mathrm{m}\delta_\mathrm{ln} - \frac{1}{4}(l_\mathrm{n}\delta_\mathrm{lm} + l_\mathrm{l}\delta_\mathrm{mn}) + \frac{3}{2}l_\mathrm{m}a_\mathrm{ln} - \frac{3}{8}l_\mathrm{o}(a_\mathrm{no}\delta_\mathrm{lm} + a_\mathrm{lo}\delta_\mathrm{mn})\right) \tag{3.15}$$

In addition, T^p_S is modeled as a linear expression of the triple moments to satisfy the realizability conditions expressed as follows [45][51].

$$T^p_\mathrm{S} = -\frac{\overline{u_\mathrm{m} u_\mathrm{m} u_\mathrm{l}}}{5} \tag{3.16}$$

In the following, the validity of these models shown above is examined by comparing $\overline{u_\mathrm{l} p}$ with T^p_R and T^p_S.

Figure 3.8 (a) shows the cross-streamwise profile of $\overline{up}/\rho\overline{U}^3_\mathrm{c}$, T^p_R, T^p_S, and sum of T^p_R and T^p_S. The ordinate shows the value of each term and the abscissa shows x_2/b. The solid, dashed, dot-dashed, dotted line indicates $\overline{up}/\rho\overline{U}^3_\mathrm{c}$, T^p_R, T^p_R, and sum of T^p_R and T^p_S, respectively. It is found that the profile of $\overline{up}/\rho\overline{U}^3_\mathrm{c}$ shows some difference from the profile of T^p_S especially in the region near the jet centerline. However, the profile of sum of T^p_R and T^p_S is closer to the profile of $\overline{up}/\rho\overline{U}^3_\mathrm{c}$ than that of T^p_S.

Figure 3.8 (b) shows the cross-streamwise profile of $\overline{vp}/\rho\overline{U}_c^3$, T_R^p, T_S^p, and sum of T_R^p and T_S^p. The meanings of the ordinate, abscissa and lines are the same with those of Figure 3.8 (a). It is found that the profile of $\overline{vp}/\rho\overline{U}_c^3$ shows some difference from the profile of T_S^p in the range $x_2/b \leq 1.2$. However, the profile of sum of T_R^p and T_S^p is almost the same with the profile of $\overline{up}/\rho\overline{U}_c^3$.

From the results described above, it can be concluded that the pressure diffusion process can not be modeled only by the slow term and the modeling of the pressure diffusion process by both rapid and slow term can achieve the improvement of the modeling accuracy.

3.4 Conclusions

In this chapter, by using the combined probe developed in Chapter 2, the simultaneous measurement of the velocity and pressure in a plane jet is performed again and the measured results are discussed from another point of view. Firstly, for the more detail understanding of the flow phenomena in the intermittent region of a plane jet, the conditional ensemble-averaged statistics are investigated on the basis of the intermittency function obtained from the velocity signal by the hot-wire sensor set in the intermittent region of a plane jet. Secondly, the validity of the models for the turbulent and pressure diffusion term such as Daly & Harlow model, Shir model and the model for the rapid/slow term is investigated. The results are summarized as follows.

1. Estimated results of the turbulent energy budget of the turbulent energy transport equation shows that the profiles of the convection term, production term and diffusion term depend on the flow state in the intermittent region of the jet. When the flow state is turbulent, the convection of the turbulent energy to the inner region of the jet and the production profile of the turbulent energy extends to the outer region becomes large. Further, the diffusion of the turbulent energy to the outer region of the jet is enhanced.

2. Estimated results of the turbulent energy budget of the turbulent energy transport equation also shows that the profile of the turbulent diffusion term depends on the flow state in the intermittent region but the pressure diffusion term does not strongly depend on it. Therefore, the dependence of the diffusion process on the flow state is caused of that of the turbulent diffusion process. Further, the pressure diffusion of the turbulent energy to the inner side of the jet observed in the previous

studies is not caused by the entrainment/ejection process which strongly relates to the turbulent intermittency.

3. Daly & Harlow model is adequate for the flow filed where the effect of the pressure diffusion process is weak and the turbulent intermittency is small and Shir model is adequate for the flow field where the effect of the pressure diffusion process is relatively strong and the turbulent intermittency is small.

4. The pressure diffusion process can not be modeled only by the slow term and the modeling of the pressure diffusion process by both of the rapid and the slow term can achieve the improvement of the modeling accuracy.

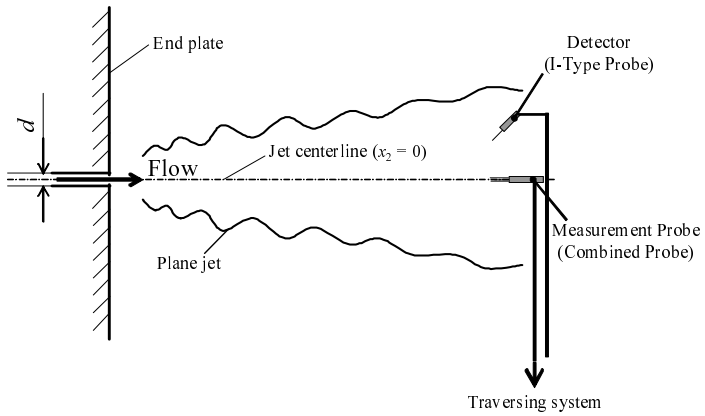

Figure 3.1 Schematic view of the combined probe and detector in a plane jet.

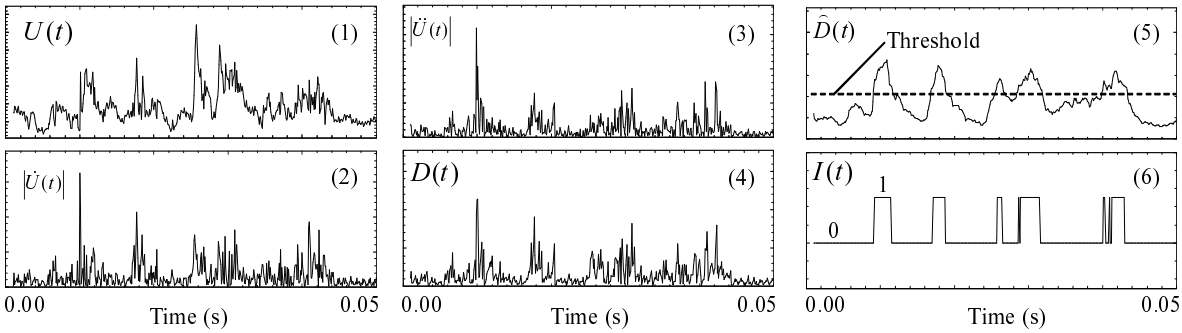

Figure 3.2 Signal processing for turbulent/non-turbulent decision.

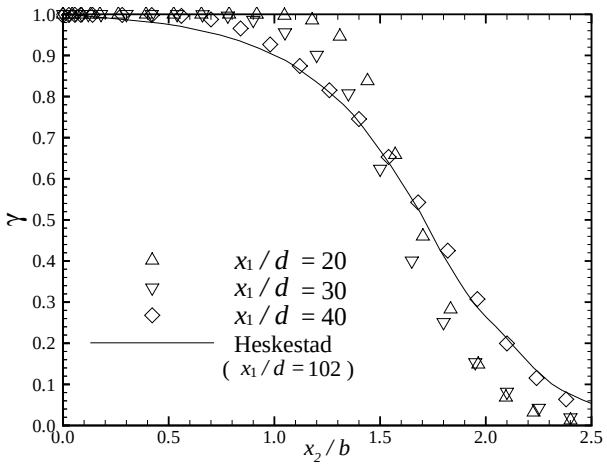

Figure 3.3 Cross-streamwise profiles of intermittency factor γ.

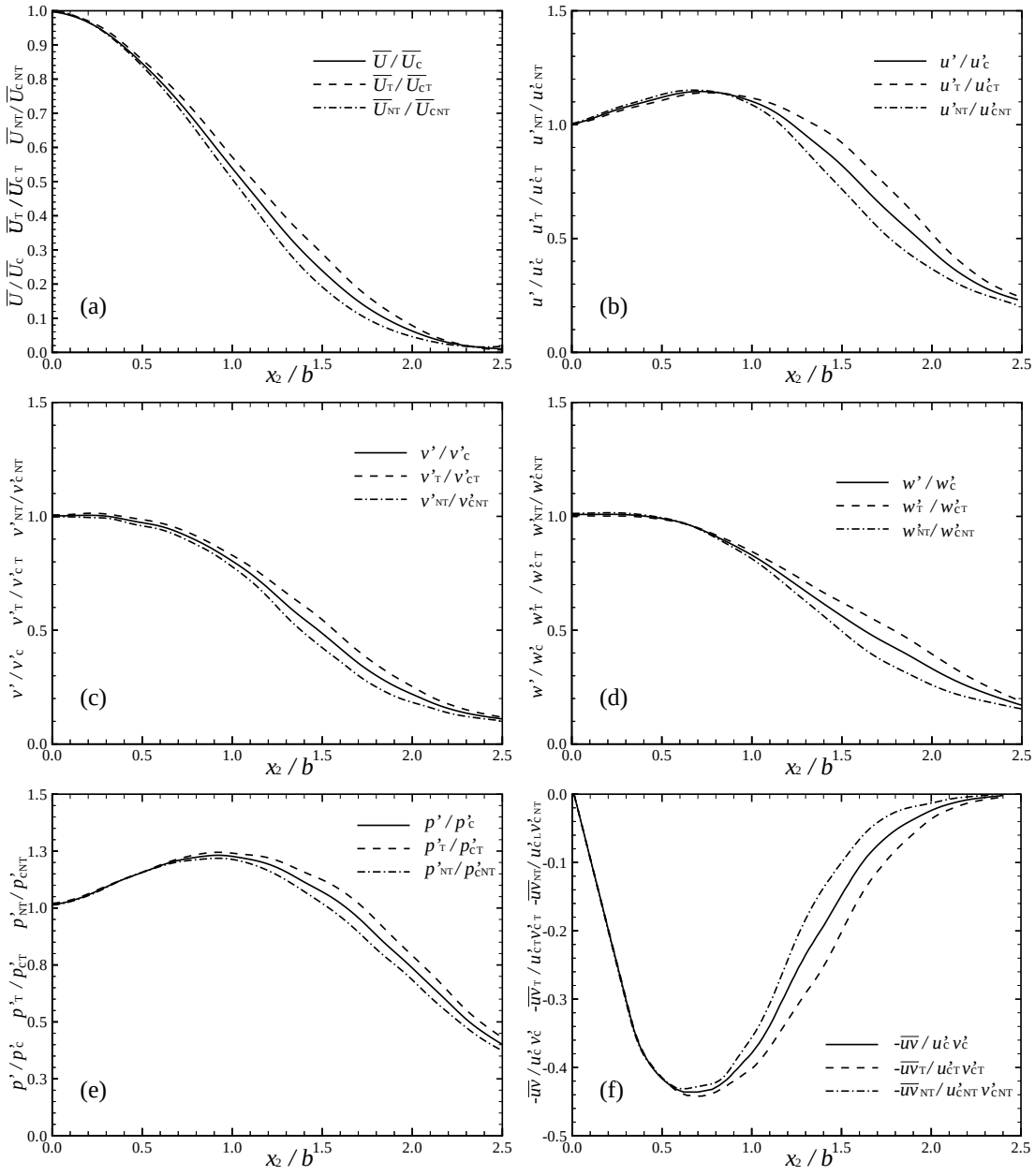

Figure 3.4 Cross-streamwise profiles of (a) mean streamwise velocity $\overline{U}$, (b) RMS value of the streamwise velocity fluctuation u', (c) RMS value of the cross-streamwise velocity fluctuation v', (d) RMS value of the spanwise velocity fluctuation w', (e) RMS value of the static pressure fluctuation p', and (f) Reynolds stress -$\overline{uv}$.

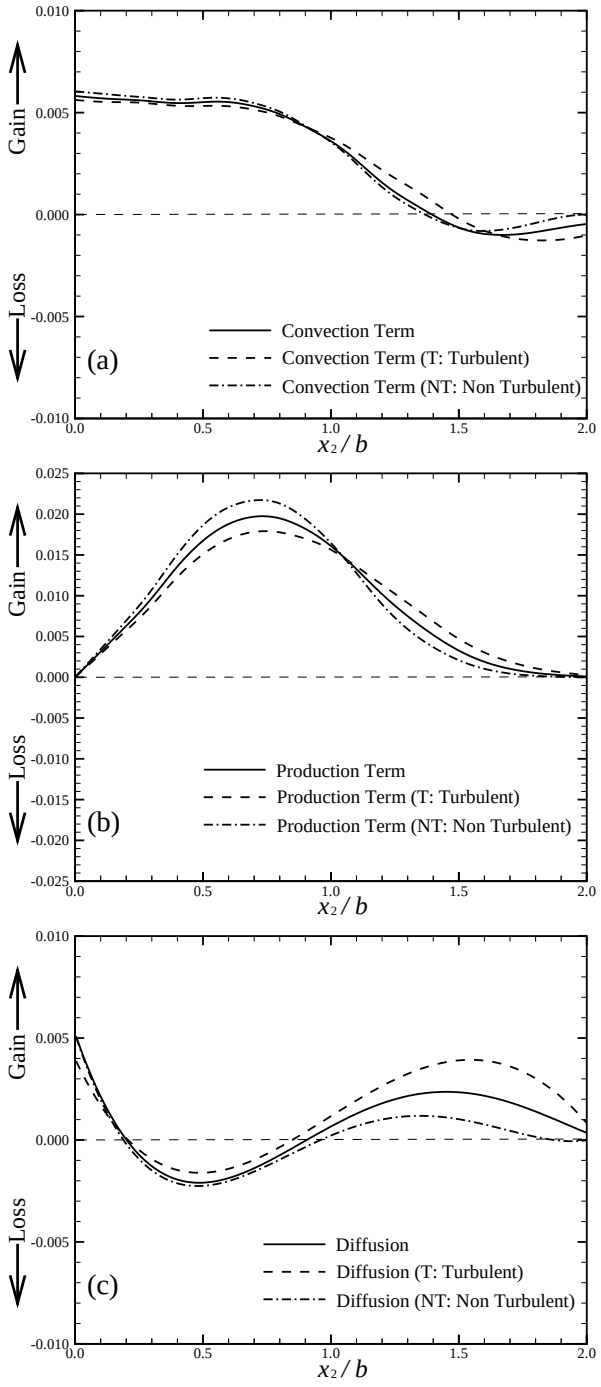

Figure 3.5 Cross-streamwise profiles of (a) convection term, (b) production term, and (c) diffusion term in turbulent energy transport equation.

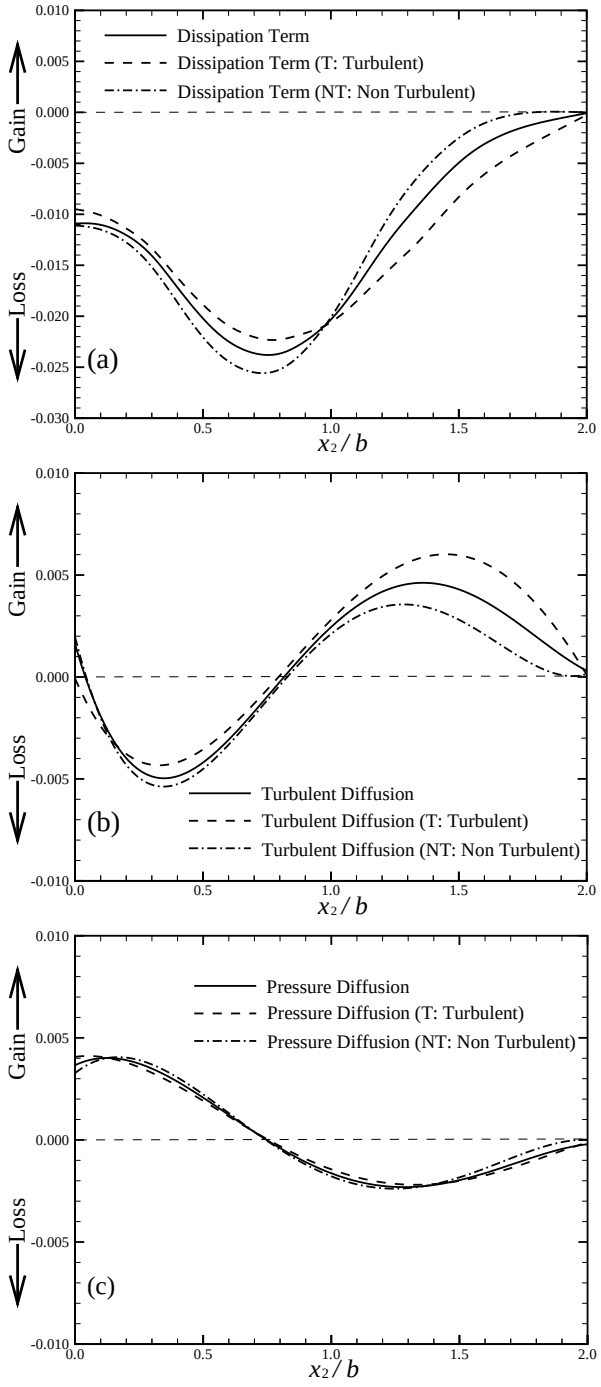

Figure 3.6 Cross-streamwise profiles of (a) dissipation term, (b) turbulent-diffusion term, and (c) pressure-diffusion term in turbulent energy transport equation.

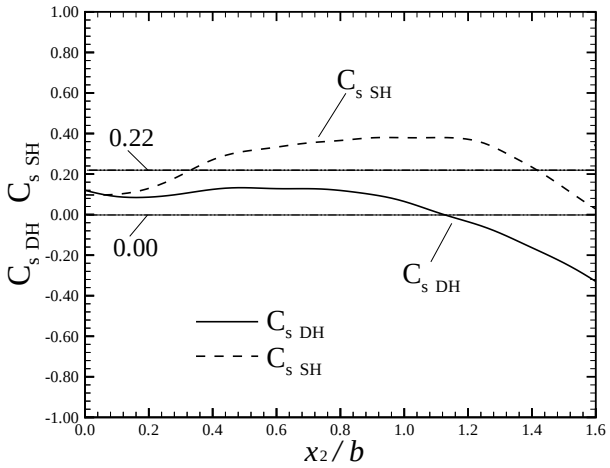

Figure 3.7 Cross-streamwise profile of model constant C_{sDH} and C_{sSH}.

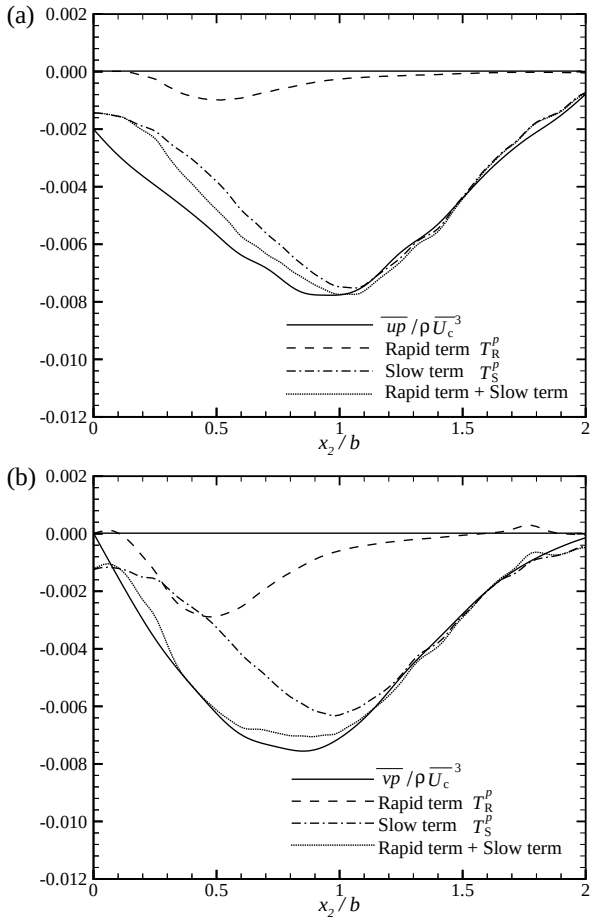

Figure 3.8 Cross-streamwise profile of pressure-velocity correlation and rapid/slow term of pressure diffusion process. (a) $\overline{up}$ and (b) $\overline{vp}$.

Chapter 4

Study on the interfacial layer between turbulent/non-turbulent region in a plane jet [108][109]

4.1 Introduction

In Chapter 3, the conditional ensemble-averaged statistics were investigated on the basis of the intermittency function in the intermittent region of a plane jet. Further, the validity of the models for the turbulent and pressure diffusion term (Daly & Harlow model and Shir model), and the model for the rapid/slow term was investigated. However, the flow characteristics and vortex structure just near the turbulent/non-turbulent interface have not been clarified. Moreover, at the interface between the turbulent and non-turbulent region in the free shear flow observed in the jets and wakes, the entrainment of the non-turbulent fluid into the turbulent fluid and the sticking out (nibbling) of the turbulent region into the non-turbulent region arise and these phenomena are very interesting from academic and industrial viewpoints because they relate to the mixing and the diffusion of the fluid and the scalar.

From these backgrounds, in this chapter, the measurement of the velocity and pressure field near the interface between the turbulent and the non-turbulent region is conducted in a plane jet in order to clarify the flow characteristics and vortex structure just near the turbulent/non-turbulent interface on the basis of the experiment method and results obtained in Chapter 3. The velocity and the pressure field are measured simultaneously using a combined probe shown in previous chapters. The measurement data are analyzed by using the conditional sampling technique and an ensemble-averaged technique on the basis of the intermittency function for the turbulent/non-turbulent decision, and the results are discussed.

4.2 Experimental setup and procedure

4.2.1 Experimental apparatus and conditions

The experiment is performed in a plane jet shown in Figure 2.11. The experimental apparatus, coordinate system and conditions are the same with the experiment described in Chapter 3.

4.2.2 Detection of the interface

In this study, the cross-streamwise profile of the velocity and pressure near the interface between the turbulent and non-turbulent region of a plane jet shown in Figure 4.1. The measurement is performed by means of a combined probe to measure two-components of the velocity and pressure simultaneously, and a detector to detect the interface. The combined probe, the detector and their spatial arrangement are the same as the experiment described in Chapter 3.

The process of the detection of the interface is proposed with reference to the study by Inasawa et al. [16] as follows. Firstly, the detector is installed at $x_2/b = 1.7$, $x_1/d = 40$. Next, we traverse the combined probe around the detector in the range $1.4 \leq x_2/b \leq 2.0$ at $x_1/d = 40$ and measure two-components of the velocity and pressure by the combined probe and the streamwise velocity by the detector, simultaneously. Next, obtain the intermittency function $I(t)$ from measured data by applying the same method described in section 2.3.3 ($I(t) = 0$: Non turbulent, $I(t) = 1$: Turbulent). Finally, the time when the intermittency function of the detector $I_\mathrm{d}(t)$ changes from 0 to 1, and the intermittency function of the combined probe $I_\mathrm{c}(t)$ is 1 ($x_2/b \leq 1.7$) and 0 ($x_2/b \geq 1.7$) is determined as the time when the detector detects the interface (hereafter this time is denoted as t_d) as shown in Figure 4.2.

4.3 Results and discussions

4.3.1 Base flow

The cross-streamwise profiles of the streamwise mean velocity $\overline{U}$, the RMS value of the streamwise velocity fluctuation u', the RMS value of the pressure fluctuation p', the Reynolds stress -$\overline{uv}$, and the intermittency factor γ were shown in Figures 2.21, 2.22, 2.23, 2.24, and 3.3 in Chapters 2 and 3, respectively.

4.3.2 Conditional ensemble-averaged statistics

Velocity and pressure field

Figure 4.3 (a) shows the cross-streamwise profile of conditional ensemble-averaged streamwise velocity $\overline{U_{\rm con}}$, the RMS value of the streamwise velocity fluctuation $u'_{\rm con}$, and the cross-streamwise velocity fluctuation $v'_{\rm con}$. In this estimation, $\overline{U_{\rm con}}$, $u'_{\rm con}$, and $v'_{\rm con}$ are defined as follows and conditional ensemble-averaged value is the ensemble-averaged value when detector detects the interface ($t = t_{\rm d}$).

$$\overline{U_{\rm con}} = \frac{1}{\rm N}\sum_{\rm i=1}^{\rm N} U_{\rm con,i} \tag{4.1}$$

$$u'_{\rm con} = \sqrt{\frac{1}{\rm N}\sum_{\rm i=1}^{\rm N}(u_{\rm con,i})^2} = \sqrt{\frac{1}{\rm N}\sum_{\rm i=1}^{\rm N}(U_{\rm con,i} - \overline{U})^2} \tag{4.2}$$

$$v'_{\rm con} = \sqrt{\frac{1}{\rm N}\sum_{\rm i=1}^{\rm N}(v_{\rm con,i})^2} = \sqrt{\frac{1}{\rm N}\sum_{\rm i=1}^{\rm N}(V_{\rm con,i} - \overline{V})^2} \tag{4.3}$$

Here, $U_{\rm con}$ and $V_{\rm con}$ are the streamwise and the cross-streamwise velocity at $t_{\rm d}$, respectively. N is the number of realization in the ensemble-averaging and it is almost 2,000 in this study. The ordinate shows $\overline{U_{\rm con}}/\overline{U_{\rm c}}$, $u'_{\rm con}/u'_{\rm c}$, $v'_{\rm con}/v'_{\rm c}$ and the abscissa shows x_2/b. The symbols in the figure show the measurement point with respect to each of two measurement points (i.e., the space interval of the measurement is $x_2/b = 0.01$). It is found that $\overline{U_{\rm con}}$, $u'_{\rm con}$, and $v'_{\rm con}$ change near the interface ($x_2/b = 1.7$) rapidly and they change in the range $1.62 \leq x_2/b \leq 1.7$. Hereafter, this region is called as "interfacial layer". The thickness of the interfacial layer is about 0.08 b which corresponds to the 1.0 - 1.1 times the Taylor microscale at the measurement position. DNS results by Bisset et al. [12] indicated that the thickness of the interfacial layer is almost the same with the Taylor microscale at the measurement position. Therefore, it can be concluded that the results of present study are consistent with the results of their results.

Figure 4.3 (b) shows the cross-streamwise profile of the Reynolds stress -$\overline{u_{\rm con}v_{\rm con}}$ and the turbulent energy $k_{\rm con}$. Here, $\overline{u_{\rm con}v_{\rm con}}$ and $k_{\rm con}$ are defined as follows.

$$\overline{u_{\rm con}v_{\rm con}} = \frac{1}{\rm N}\sum_{\rm i=1}^{\rm N}(u_{\rm con,i}v_{\rm con,i}) \tag{4.4}$$

$$k_{\rm con} = \frac{1}{2}(\overline{u^2_{\rm con}} + \overline{v^2_{\rm con}} + \overline{w^2_{\rm con}}) \tag{4.5}$$

The ordinate shows -$\overline{u_{\rm con}v_{\rm con}}/u'_{\rm c}v'_{\rm c}$ and $k_{\rm con}/k_{\rm c}$. The abscissa and the meanings of the symbols in the figure are the same with Figure 4.3 (a). It is found that -$\overline{u_{\rm con}v_{\rm con}}$ and $k_{\rm con}$ also change near the interface. Further, -$\overline{u_{\rm con}v_{\rm con}}$ becomes almost zero in the non-turbulent region ($x_2/b \geq 1.7$).

Figure 4.3 (c) shows the cross-streamwise profile of $\overline{u_{\rm con}}$, $\overline{v_{\rm con}}$ and $\overline{p_{\rm con}}$. Here, $\overline{p_{\rm con}}$ is expressed as follows.

$$\overline{p_{\rm con}} = \frac{1}{\rm N}\sum_{\rm i=1}^{\rm N}(p_{\rm con,i}) \tag{4.6}$$

where $p_{\rm con}$ is pressure fluctuation at $t_{\rm d}$. The ordinate shows $\overline{u_{\rm con}}/u'_{\rm c}$, $\overline{v_{\rm con}}/v'_{\rm c}$, and $\overline{p_{\rm con}}/p'_{\rm c}$. The abscissa and the meanings of the symbols in the figure are the same with Figure 4.3 (a). It is found that $\overline{u_{\rm con}}$, $\overline{v_{\rm con}}$, and $\overline{p_{\rm con}}$ also change near the interface. In addition, the sign of $\overline{u_{\rm con}}$ and $\overline{v_{\rm con}}$ change across the interfacial layer. Further, there is a local minimum of the static pressure at the middle of the interfacial layer, represented by the circle in Figure 4.3 (c). Figure 4.3 (c) implies that the vortex exists in the interfacial layer as illustrated in Figure 4.4.

Turbulent energy budget

In my previous studies shown in the previous chapters, the turbulent energy budget of the turbulent energy transport equation for a plane jet was estimated. With reference to the previous studies, the profile of the convection term, production term, and diffusion term near the interface are estimated in this section.

Figure 4.5 shows the cross-streamwise profile of the convection term, production term, and diffusion term near the interface. In this estimation, the convection term is estimated by the next equation.

$$\mathrm{CT} = \overline{U_{\rm con}}\frac{\partial k_{\rm con}}{\partial x_1} + \overline{V_{\rm con}}\frac{\partial k_{\rm con}}{\partial x_2} \tag{4.7}$$

The production term is estimated by next equation.

$$\mathrm{PT} = \overline{u_{\rm con}v_{\rm con}}\frac{\partial \overline{U_{\rm con}}}{\partial x_2} + (\overline{u^2_{\rm con}} - \overline{v^2_{\rm con}})\frac{\partial \overline{U_{\rm con}}}{\partial x_1} \tag{4.8}$$

The diffusion is estimated by next equation.

$$\mathrm{DT} = \frac{\partial}{\partial x_2}(\overline{v_{\rm con}k_{\rm con}} + \frac{1}{\rho}\overline{v_{\rm con}p_{\rm con}}) \tag{4.9}$$

The ordinate shows the value of the convection term, production term, diffusion term and the abscissa shows x_2/b. The meanings of the symbols in the figure are as follows;

$\square$: Convection term, $\triangle$: Production term, and $\triangledown$: Diffusion term. It is found that the convection of the turbulent energy near the interface is very small and the production of the turbulent energy rapidly decreases across the interface. Further, the loss of the turbulent energy by the diffusion process arises in the middle of the interfacial layer and the gain of the energy arises in the inner and the outer side of the layer. These results imply that the produced turbulent energy near the interface transported to the inner side of the interface and the outer "non-terbulent region".

Figure 4.6 shows the cross-streamwise profile of the total diffusion term (sum of the turbulent diffusion term and pressure diffusion term), turbulent diffusion term, and pressure diffusion term near the interface. Here, the turbulent diffusion term is the first term in Equation (4.9) and the pressure diffusion term is its second term. The ordinate shows the value of the total diffusion term, turbulent diffusion term, pressure diffusion term and the abscissa shows x_2/b. The solid line, dashed line, and dot-dash line show the total diffusion term, turbulent diffusion term, and pressure diffusion term, respectively. It is found that the turbulent energy is transported to the inner side of the interface and no diffusion can be observed into the outer side of the interface in turbulent diffusion process. It is also found that the loss of the turbulent energy in the inner side of the interface arises and a little transport of the turbulent energy can be observed into the outer side of the interface by the pressure diffusion process. These results indicate that the transport of the turbulent energy to the inner side of the interface is caused by turbulent diffusion, and that to the "non-turbulent region" (the outer side of the interface) is caused by pressure diffusion. If this transportation of the turbulent energy contributes to the transition of the non-turbulent fluid (to the turbulent fluid), it must be concluded that the existence of the interfacial layer is very important to the transition of the non-turbulent fluid because the transportation of the turbulent energy to the non-turbulent region is determined by the pressure diffusion, and it is caused by the existence of the interfacial layer.

Pressure field in outer side of interface

Based on the above results, there is a possibility that the turbulent energy is transported from the inner side and the inside of the interfacial layer to the outer non-turbulent region, and this energy transport is caused by the existence of the interfacial layer. In this section, the cross-streamwise profile of RMS value of pressure fluctuation at the outer side of the interfacial layer (the non-turbulent region) is investigated.

The measurements for the investigation is performed by using the detector (set at x_1/d

= 40, $x_2/b = 1.7$) and the combined probe which is set at $x_1/d = 40$ and $x_2/b \geq 1.7$. The measurement data are analyzed according to a conditional ensemble-averaging technique on the basis of the intermittency function $I_c(t)$ and $I_d(t)$. The time t_d is defined as t_1, and expressed by the normalized spatial distance L_i (= $\overline{U}_{1.7}\ t_i/b$, $\overline{U}_{1.7}$ is time-averaged streamwise velocity at $x_2/b = 1.7$). In this investigation, the cross-streamwise profile of RMS value of pressuer fluctuation p'_{con} at 0.0 (L_1), -0.055 (L_2), and -0.110 (L_3) whose relation to $I_d(t)$ is shown in Figure 4.7 are estimated.

Figure 4.8 shows the cross-streamwise profiles of the RMS value of the pressure fluctuation p'_{con} at L_1, L_2, and L_3. The ordinate shows p'_{con}/p'_c and the abscissa shows x_2/b. The solid, dashed, and dot-dash line show the profile of L_1, L_2, and L_3, respectively. It is found that p'_{con} at the outer side ($x_2 \geq 1.7$) of the interface becomes large as the interface approaches to the detector.

These results shown above indicate that the turbulent energy (pressure energy) of the non-turbulent fluid in the outer side of the interface increases as a result of the approach of the interface to the non-turbulent fluid: and also, the results support the assertion, mentioned in the previous sections that the turbulent energy is transported to the non-turbulent region by the pressure diffusion process.

4.4 Conclusions

In this study, the measurement of the velocity and pressure field near the interface of the turbulent and non-turbulent region is conducted in a plane jet in order to clarify the flow characteristics and vortex structure just near the turbulent/non-turbulent interface on the basis of the experiment method and obtained results in Chapter 3. The velocity and the pressure field are measured simultaneously using a combined probe comprising an X-type hot-wire and a static pressure tube. The measurement data are analyzed using the conditional sampling technique and an ensemble-averaged technique on the basis of the intermittency function for the turbulent/non-turbulent decision, and the results are discussed. The results are summarized as follows.

1. It is found that there is a thin interfacial layer between the turbulent and the non-turbulent region accompanied with the rapidly changing of the physical values, such as the streamwise velocity.

2. The thickness of the interfacial layer is 0.08 times the half-widh of the cross-streamwise profile of the mean streamwise velocity and almost the same as Taylor

transverse micro scale of the turbulent fluid at the measurement position.

3. The velocity and pressure field near the interfacial layer indicate the existence of vorticity at the middle of the interfacial layer.

4. From the separated estimation of the diffusion term in the transport equation of the turbulent energy, it is found that the turbulent energy is transported from the inner side and the inside of the interfacial layer to the outer non-turbulent region by the pressure diffusion. In addition, this transportation of the turbulent energy is caused by the existence of the interfacial layer.

5. There is a possibility that the existence of the interfacial layer is one of the processes for the transition of the non-turbulent fluid to the turbulent fluid, because the existence of the interfacial layer and the approach of the interfacial layer to the non-turbulent region cause the transportation of turbulent energy to the non-turbulent fluid.

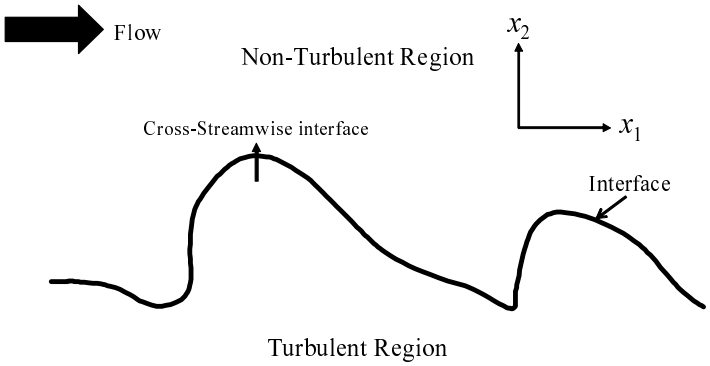

Figure 4.1 Definition and roughly sketch of the interface between turbulent and non-turbulent region.

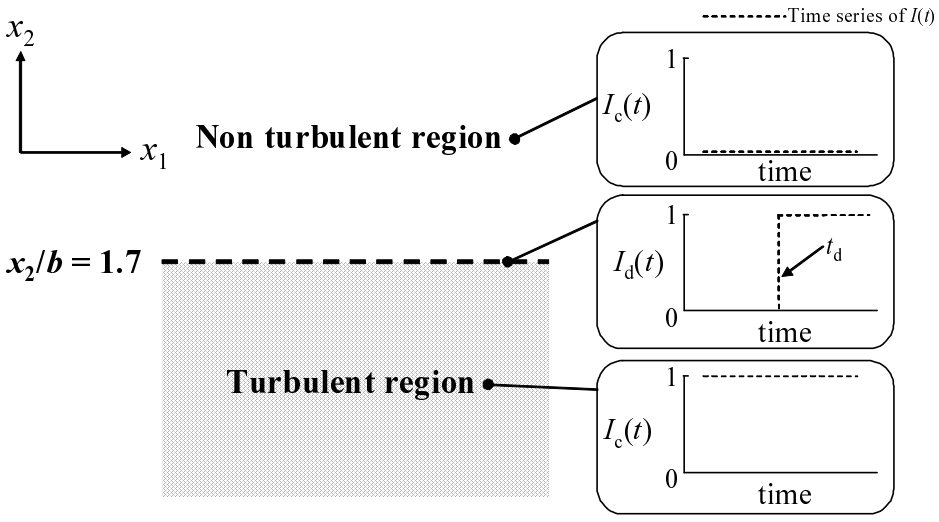

Figure 4.2 Definition of the time when the detector detects the interface (t_d).

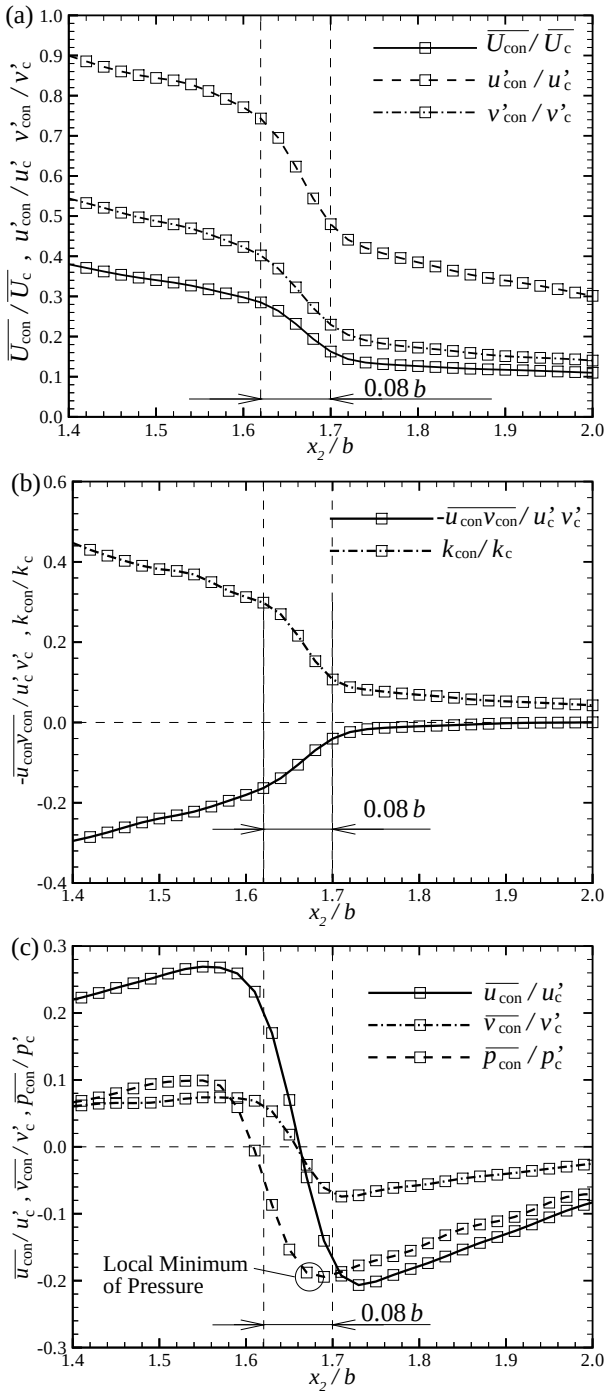

Figure 4.3 Cross-streamwise profiles of (a) $\overline{U_{\rm con}}/U_c$, $u'_{\rm con}/u'_c$, $v'_{\rm con}/v'_c$, (b) $-\overline{u_{\rm con}v_{\rm con}}/u'_c v'_c$, $k_{\rm con}/k_c$, and (c) $\overline{u_{\rm con}}/u'_c$, $\overline{v_{\rm con}}/v'_c$, $\overline{p_{\rm con}}/p'_c$.

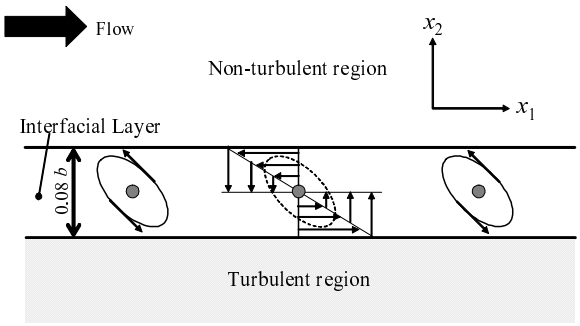

Figure 4.4 Sketch of vortex structure in the interfacial layer.

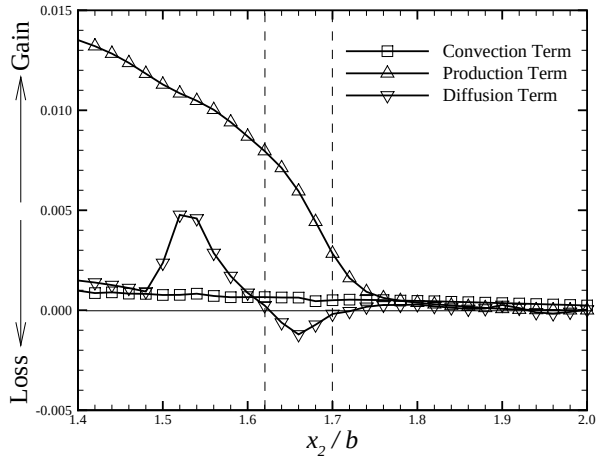

Figure 4.5 Cross-streamwise profile of convection term, production term, and diffusion term near the interface.

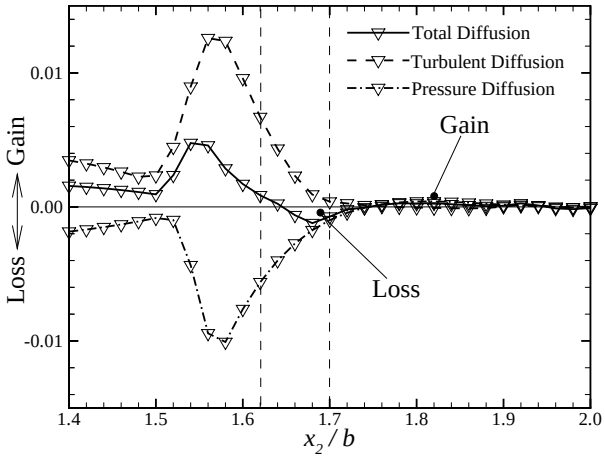

Figure 4.6 Cross-streamwise profile of turbulent diffusion term and pressure diffusion term.

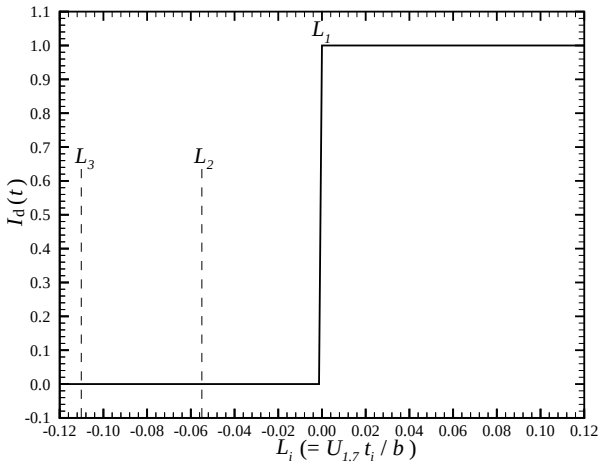

Figure 4.7 Normalized spatial distance L_1, L_2, and L_3

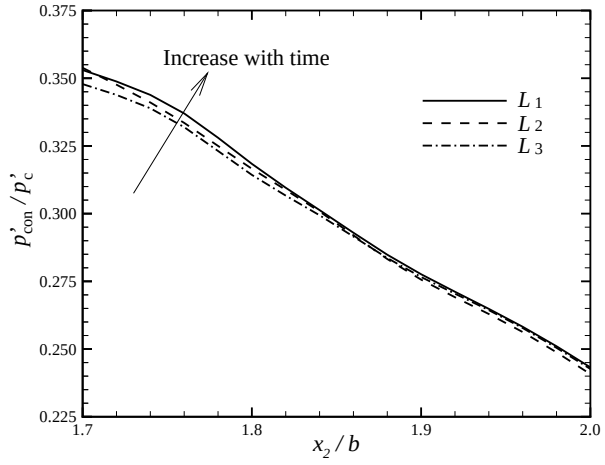

Figure 4.8 Cross-streamwise profile of $p'_{\mathrm{con}}/p'_{\mathrm{c}}$.

Chapter 5

Streamwise interfaces of an isolated turbulent region in a laminar boundary layer [110][111][112][113]

5.1 Introduction

In chapter 4, the flow characteristics and vortex structure near the cross-streamwise interface of turbulent/non-turbulent region in a plane jet were investigated. In this chapter, the interface between the turbulent/non-turbulent (laminar) region is investigated again in an isolated turbulent region excited into a laminar boundary layer.

The objective of the present study is to understand the flow phenomenon at the streamwise interfaces between the turbulent and laminar regions, which is independent of the influence of the spanwise interfaces. A turbulent region is periodically generated in a laminar boundary layer by periodically activating bimorph-type piezoceramic actuator that raises its trailing end from the wall. The shape of a turbulent region generated by the piezoceramic actuator becomes trapezoidal and the interference of the spanwise interfaces with the streamwise interfaces can be substantially reduced. Therefore, the streamwise interfaces become more pure. In the experiment, the velocity fields at the leading or trailing end of the turbulent region are measured by a single-type hot-wire probe and a rake with six individual hot-wire probes is connected to a constant temperature anemometer (CTA). The measured data are analyzed using an ensemble-averaging technique. For an understanding of the mechanism by which the turbulent region spreads in the streamwise direction, the results are discussed particularly from the perspective of the transport of the turbulent/laminar fluid through the interfaces.

5.2 Experimental setup and procedure

5.2.1 Experimental setup

Wind tunnel and flat plate

The experiment is performed in a blowout-type wind tunnel shown in Figure 5.1. The contraction ratio of the nozzle is 9:1 and a closed-type test section is connected to the contraction nozzle. The length of the test section is 2,000 mm in the streamwise direction and its cross section is a square of 500 $\times$ 500 mm^2. The ceiling of the test section is adjustable to realize zero pressure gradient in the streamwise direction. The free stream velocity U_∞ is set at 5.0 m/s and the RMS value of the streamwise velocity fluctuation u_{R} in the free stream is less than 0.25% of U_∞ (i.e., turbulent intensity $u_{\mathrm{R}}/U_\infty \leq 0.0025$). A flat plate with piezoceramic actuator (described in the next subsection) is set in the test section and periodically activated to excite a series of isolated turbulent regions within a laminar boundary layer.

The schematic view of the flat plate with a piezoceramic actuator used is shown in Figure 5.2. The plate is 1,800 mm long, 490 mm wide, and 10 mm thick, and is horizontally mounted 200 mm above the floor of the test section. An elliptical leading edge with the radius ratio 24:1 is attached to the plate, and a flap with a 190 mm chord is attached at the downstream end to adjust the stagnation point at the leading edge. The origin of the coordinate system is located at the center of the leading edge of the plate. The streamwise, wall-normal and spanwise coordinates are x, y, and z, respectively.

Piezoceramic actuator

To excite a widely spreading turbulent region periodically in the laminar boundary layer, a pair of piezoceramic actuator is used. The characteristics of the piezoceramic piece are described in the following paragraphs.

A piezoceramic piece has the capability to produce an electrical voltage when a mechanical stress is imposed on it. The piezoceramic piece also exhibits the opposite effect, called the converse piezoelectric effect, in which an electrical field creates a mechanical stress (i.e., deformation or distortion) in the crystal. This transducing effect is called the piezoelectric effect. The negative ions move toward the positive electrode when voltage is applied. Therefore, a piezoceramic piece can be expanded or contracted because the crystals in the piezoceramic piece have self-polarization.

There are two types of piezoceramics: one is the unimorph type and the other is the

bimorph type, as shown in Figure 5.3. The unimorph type is made from only one piezoceramic piece, which expands by positive voltage and contracts by negative voltage. The bimorph type is made from two piezoceramic pieces, which deform in opposite directions. Therefore, it can perform a bending motion. In the previous studies, the unimorph type was used to excite the streamwise velocity fluctuations in a boundary layer by supplying alternating current to the piezoceramic pieces (Fukunishi et al. [114]), and the bimorph type was used to generate the turbulent wedge in a laminar boundary layer (Inasawa et al. [16]).

In this study, two bimorph-type piezoceramic pieces are used as an actuator, as shown in Figure 5.2. Each piezoceramic piece is 150 mm long, 40 mm wide, and 0.5 mm thick. The downstream ends of both piezoceramic pieces are located at $x = 350$ mm. The piezoceramic pieces are fixed horizontally on the flat plate using double-faced tapes at 200 mm $\leq x \leq$ 230 mm (i.e., only upstream-side 30 mm of the piezoceramic pieces are glued). Therefore, the downstream ends can be moved upward by supplying voltage to the piezoceramic pieces. Dummy pieces made of rigid polyvinyl chloride fill the spacing between the spanwise ends of the piezoceramic pair and the side walls, in order to maintain the two-dimensionality of the flow. When a voltage of 80 DC V is applied to the piezoceramic pieces, the downstream end is raised 2.0 mm from the wall surface. The height (2.0 mm) corresponds to 39% of the laminar boundary layer thickness δ_{99} and 113% of the displacement thickness δ^* at the downstream end location ($x = 350$ mm). In the experiment, 80 DC V is applied for a duration of 0.04 s every second. Hence, the turbulent region is excited in the laminar boundary layer at an interval of one second. The voltage signal used in activating the piezoceramic pieces is shown in Figure 5.4. This method has an advantage in generating a turbulent region of a preferred size, compared to other methods used for generation of turbulent spots, where jet ejection through a tiny hole is commonly used.

Definition of the turbulent region

In order to investigate the interface between the turbulent region and the laminar region, it is necessary to define the turbulent region. In the previous studies (Hedley et al. [103], Gad-el-hak et al. [21], Wygnanski et al. [115], Gostelow et al. [27], and Chong et al.[116]), many methods have been proposed. In this study, the random component of the streamwise velocity signal is used to define a turbulent region. The random component is defined as the difference between the randomly fluctuating value (e.g., streamwise velocity

fluctuation) and the ensemble-averaged value. Here, the random component $\hat{u}(t)$ and the intensity of the random component $\hat{u}_{\mathrm{R}}(t)$ are respectively given by the following equations:

$$U(t) = \overline{U} + \tilde{u}(t) + \hat{u}(t) = \tilde{U}(t) + \hat{u}(t) \tag{5.1}$$

$$\hat{u}_{\mathrm{R}}(t) = \sqrt{\frac{1}{\mathrm{N}} \sum_{i=1}^{\mathrm{N}} (\hat{u}_i(t))^2} \tag{5.2}$$

where, $U(t)$ is the instantaneous streamwise velocity, $\overline{U}$ is the time-averaged streamwise velocity, $\tilde{u}(t)$ is the periodic streamwise velocity fluctuation that corresponds to the ensemble-averaged fluctuation, $\tilde{U}(t)$ $(= \overline{U} + \tilde{u}(t))$ is the ensemble-averaged streamwise velocity, and N is the number of realizations in the ensemble-averaging (N = 120). In this study, the region where $\hat{u}_{\mathrm{R}}/U_\infty$ is greater than 0.02 is defined as the turbulent region. Here, U_∞ is the free stream velocity in the test section. By using this index, turbulent and laminar regions are distinguished more clearly, because the large irregularity of the streamwise velocity fluctuation, which is shown by the large intensity of the random component, is one of the properties of the turbulent region. In addition, the streamwise velocity fluctuation $u(t)$ is defined in this study by the following equation.

$$u(t) = \tilde{u}(t) + \hat{u}(t) \tag{5.3}$$

5.3 Results and discussion

5.3.1 Base flow

The x profile of the pressure coefficient C_{p} in the test section is shown in Figure 5.6. The abscissa indicates the streamwise location x and the ordinate is the pressure coefficient -C_{p} which is defined as follows:

$$-C_{\mathrm{p}} = \frac{-P + P_0}{\rho U_\infty^2/2} \tag{5.4}$$

where P is the static pressure at each streamwise location (0, 200, 400, 600, 800, and 1000 mm), P_0 is the static pressure at $x = 0$ and ρ is the density of the fluid. The static pressure is measured by a manometer through holes set on the sidewall of the test section. Figure 5.6 shows that variation C_{p} is less than 0.002 at each streamwise location which is much smaller than the dynamic pressure of the flow $(= \rho U_\infty^2/2)$. Therefore, it can be concluded that there is almost no pressure gradient in the test section.

Figure 5.7 shows the wall-normal profiles of $\overline{U}$ at x = 400, 500, 600, 700, 800, 900 mm, and $z = 0$. The abscissa is the normalized height from a flat plate η, the ordinate

is $\overline{U}/U_\infty$, and the solid line indicates the Blasius profile. Here, η is equal to $y\sqrt{U_\infty/\nu x}$ and ν is kinematic viscosity. Figure 5.7 indicates that the measured results are in good agreement with the Blasius profile, showing that the boundary layer on the flat plate when the actuator is not activated is a laminar Blasius boundary layer.

Figure 5.8 shows the wall-normal profiles of the RMS value of the streamwise velocity fluctuation u_R in a laminar boundary layer (i.e., the actuator is not activated). The abscissa is the same as that in Figure 5.7 and the ordinate is u_R/U_∞. Figure 5.8 indicates that the turbulent intensity u_R/U_∞ is less than 0.006 in the laminar boundary layer. This value is much lower than 0.02, which is the threshold to identify the flow states (laminar or turbulent), and it is much lower than the intensity of the free stream turbulence that influences the characteristics of the turbulent spot investigated in some previous studies (e.g., Fransson et al. [117]).

5.3.2 Excited turbulent region

First, we measured the flow field keeping the actuator always activated (i.e., DC power was continuously supplied to the actuator). For the profiles of the mean streamwise velocity and RMS value of the streamwise velocity fluctuation, one should refer to the previous study (Inasawa et al. [16]). Figure 5.9 shows the power spectrum of the streamwise velocity fluctuation at various distances from the wall, namely $\eta = 1.6$, 2.6, 3.6, 4.6, 5.6 at $x = 750$ mm, and $z = 0$. The abscissa is the frequency and the ordinate is the power of the streamwise velocity fluctuation E_u normalized by the square of its RMS value u_R^2. As seen in Figure 5.9, the broadband spectra similar to a fully developed turbulent flow is obtained.

Waveform of the streamwise velocity fluctuation

Figure 5.10 shows a waveform of the streamwise velocity fluctuation $u(t)$ at $x = 750$ mm, $\eta = 2.0$, and $z = 0$. The abscissa is time t normalized by the actuator activating period T and the ordinate is velocity $u(t)$ normalized by free stream velocity U_∞. In the figure, it can be found that the waveform is disturbed periodically, corresponding to the actuation of the piezoceramic actuator. The result indicates that isolated turbulent regions are generated within the laminar boundary layer as intended.

A close-up view of the waveform for one excited period is shown in Figure 5.11. In the figure, it is found that the streamwise velocity increase rapidly with high irregularity for

$2.32 \leq t/T \leq 2.44$, while the velocity decreases gradually and the flow returns to original (laminar) state at t/T=2.6.

Figure 5.12 shows the time histories of the streamwise velocity fluctuation $\tilde{u}(t)$ and the intensity of the random component $\hat{u}_{\mathrm{R}}(t)$ measured at (a) $\eta = 0.7$, 1.6, 2.6 and (b) $\eta =$ 3.6, 4.6, 5.6. This measurement is performed by using a hot-wire rake, which is shown in Figure 5.5. The abscissas are t/T, while the ordinates are $\tilde{u}(t)/U_\infty$ and $\hat{u}_{\mathrm{R}}(t)/U_\infty$. The dash-dotted lines in the figures show the threshold used to determine the turbulent region ($\hat{u}_{\mathrm{R}}(t)/U_\infty = 0.02$). As seen in Figure 5.12, at the leading end of the turbulent region ($t/T = 0.25 - 0.30$), $\tilde{u}$ and $\hat{u}_{\mathrm{R}}$ change rapidly at all wall-normal positions. However, $\tilde{u}$ gradually approaches zero at different timings depending on the η position (i.e., $\eta = 5.6 \rightarrow 0.7$) after the trailing end of the turbulent region passes ($t/T = 0.4 - 0.5$). In other words, the streamwise velocity fluctuation $\tilde{u}$ maintains a high value even after the high frequency velocity fluctuation pattern associated with the turbulent region disappears.

Ensemble-averaged image of the turbulent region

Figure 5.13 shows contour maps of $\hat{u}_{\mathrm{R}}(t)$ in the xz-plane of $y = 2.0$ mm at $t/T = 0.33$ (Figure 5.13 (a)) and $t/T = 0.65$ (Figure 5.13 (b)). In each figure, abscissa is x and the ordinate is z. The bright region indicates the non-turbulent region ($\hat{u}_{\mathrm{R}}(t)/U_\infty \leq 0.02$) and the dark region indicates the turbulent region ($\hat{u}_{\mathrm{R}}(t)/U_\infty \geq 0.02$). Only $z \geq 0$ is shown in Figure 5.13, because in the preliminary experiment and in the previous studies (Inasawa et al.[16]), it was found that the turbulent region develops symmetrically with respect to $z = 0$. A turbulent region spreading in the spanwise direction can be found in Figure 5.13. Furthermore, it is found that the leading end (downstream end) and trailing end (upstream end) of the turbulent region are almost uniform in the spanwise direction. In other words, the excited turbulent region is widely spread in the spanwise direction and maintains the two-dimensionality.

Figures 5.14 (a) - 5.14 (d) show contour maps of the intensity of the random component $\hat{u}_{\mathrm{R}}(t)$ in the $x\eta$-plane at $z = 0$ at $t/T = 0.31$, 0.35, 0.45, and 0.53, respectively. The abscissas are x and the ordinates are η. The contour levels in Figure 5.14 are same as those in Figure 5.13. Dashed lines indicate $|\tilde{u}(t)/U_\infty| = 0.02$. As shown in Figure 5.14, the turbulent region moves downstream spreading in the streamwise and wall-normal directions. In the figure, it can be found that the region which has high intensity random component ($\hat{u}_{\mathrm{R}}(t)$) coincides with the region of high streamwise velocity fluctuation ($\tilde{u}(t)$), except at the trailing end of the turbulent region. This indicates that the characteristics

at the trailing end of the turbulent region are different from the rest. The characteristics of the region behind the trailing end of the turbulent region are similar to those of the calmed regions that are observed behind a turbulent spot (e.g., Schubauer et al.[18]).

5.3.3 Detailed observations of streamwise interfaces

In this section, transfer of fluid through laminar/turbulent interfaces is discussed. The transfer of fluid through the interfaces is estimated by comparing the traveling speed of the interfaces $U_{\rm int}$ with the ensemble-averaged streamwise velocity $\tilde{U}$ locations on the interfaces. In this study, the traveling speeds of the interfaces are estimated in a manner similar to the previous studies (e.g., Gad-el-hak et al. [21]).

Traveling speed of streamwise interfaces

Traveling speed of the streamwise interfaces is estimated from each (leading or trailing end) interface's arrival time to several streamwise stations. Arrival time at each streamwise station is plotted in Figure 5.15, where time at $x = 750$ mm t_{750} is used as a reference. The symbols in Figure 5.15 are as follows: ■ denotes the leading end interface of $\eta = 0.6$; □ denotes the trailing end at $\eta = 0.6$; ▲ denotes the leading end at $\eta = 1.4$; △ denotes the trailing end at $\eta = 1.4$; ▼ denotes the leading end at $\eta = 3.0$; and ▽ denotes the trailing end at $\eta = 3.0$. The measurements are performed at x = 750, 770, 790, 810, 830, 850, 870, 890, 910, 930, and 950 mm stations. Figure 5.15 shows that the travelling speeds of the interfaces are constant. The traveling speed of the leading end is about $0.8 - 0.9$ times the free stream velocity U_∞ while that of the trailing end is $0.3\ U_\infty - 0.5\ U_\infty$. The leading and trailing end speeds of the turbulent spot were approximately $0.8\ U_\infty - 0.9\ U_\infty$ and $0.5\ U_\infty - 0.6\ U_\infty$ (Wygnanski, et al. [115], Zhong et al. [118]). The present results agree with these values, though the speed of the trailing end is slightly slower.

Entrainment and relaminarization through the interfaces

The amount of fluid going through the streamwise interfaces is estimated by comparing the traveling speed of the interfaces $U_{\rm int}$ to the ensemble-averaged streamwise velocities measured at the interface locations $\tilde{U}$.

Figure 5.16 shows the wall-normal profiles of the traveling speeds of the interfaces $U_{\rm int}$ and the ensemble-averaged streamwise velocities $\tilde{U}$ at the interface. Figures 5.16 (a) and 5.16 (b) show the values measured at the leading and trailing end of the turbulent

region, respectively. The measurements are performed at $x = 750$ mm and $z = 0$. The abscissas are the traveling speeds of the streamwise interface U_{int}/U_∞ or the ensemble-averaged streamwise velocities $\tilde{U}/U_\infty$. The ordinates are the wall-normal distance η. The meanings of the symbols in Figure 5.16 are as follows: □ denotes the traveling speed of the leading end; ■ denotes the ensemble-averaged streamwise velocity measured at the leading end; △ denotes the traveling speed of the trailing end; and ▲ denotes the ensemble-averaged streamwise velocity measured at the trailing end. The dashed line in Figure 5.16 (b) indicates $\eta = 1.3$.

As seen in Figure 5.16 (a), the traveling speed of the leading end (□) is faster than the ensemble-averaged streamwise velocities (■) at all wall-normal positions. This indicates that the leading end of the turbulent region moves downstream faster than the convection speed of fluid element. Therefore, the laminar fluid entrained and the fluid that used to be laminar turned turbulent passing through the interface. On the other hand, as seen in Figure 5.16 (b), the traveling speed of the trailing end of the turbulent region (△) is faster or slower than the ensemble-averaged streamwise velocity (▲) depending on the distance from the wall η. The critical distance from the wall where the traveling speed of the interface coincide with that of fluid element is found to be at $\eta = 1.3$. At $\eta > 1.3$, because the fluid's speed (▲) exceeds the traveling speed of the trailing end (△), a laminar-to-turbulent transition takes place. However, at $\eta < 1.3$, because the traveling speed of the trailing end (△) exceeds the fluid's speed (▲), a reverse transition from a turbulent state to a laminar state takes place. This is indicated in Figure 5.17. Thus, near the wall region of the trailing end, a relaminarization (turbulent to laminar transition) is taking place.

Next, the normalized height y^+ that corresponds to $\eta = 1.3$ is estimated. Here, y^+ is defined by

$$y^+ = \frac{yU_\tau}{\nu} \tag{5.5}$$

where U_τ is an averaged friction velocity.

Figure 5.18 shows the profiles of friction velocity $U_\tau(t)$ and $y^+_{1.3}(t)$, which is defined by

$$y^+_{1.3}(t) = \frac{y_{\eta=1.3}U_\tau(t)}{\nu} \tag{5.6}$$

In the equation, $y_{\eta=1.3}$ is the y value that corresponds to $\eta = 1.3$. The abscissas are t/T, while the ordinates are $U_\tau(t)/U_\infty$ (first axis) and $y^+_{1.3}(t)$ (second axis). Figure 5.18 indicates that $y^+_{1.3}$ is roughly in the range of 10.0 to 11.0, which is equivalent to the height of the viscous sublayer of a fully-developed turbulent boundary layer. The average value of $y^+_{1.3}$ within the turbulent region ($t/T = 0.40 - 0.43$) is 10.7. It should be noted that

this time corresponds to the time when the velocity gradient between $y = 0.47$ mm and $y = 0$ becomes maximum (See Figure 5.19). Therefore, it should be pointed out that the relaminarization of turbulent fluid at the trailing end of the turbulent region takes place at the region corresponding to the viscous sublayer of the turbulent region.

5.4 Conclusions

In order to better understand the flow phenomenon at the streamwise interfaces between turbulent and laminar regions, isolated turbulent regions were periodically generated in a laminar boundary layer by activating bimorph-type piezoceramic actuator. The results obtained in this study are summarized as follows:

1. Using the piezoceramic actuator, trapezoidal turbulent region with a large spanwise width could be periodically generated in a boundary layer as intended.

2. The experimental results showed that the streamwise velocity fluctuation and the intensity of the random component both changed rapidly at the leading end of the turbulent region. On the other hand, the streamwise velocity fluctuation remained high after the intensity of the random component vanished at the trailing end of the turbulent region, which is the calmed region.

3. The traveling speed of the trapezoidal turbulent region was almost the same as those of the turbulent spots with an arrow-head shape. Therefore, it was found that the spanwise interfaces have little influence on the growth of an isolated turbulent region in a laminar boundary layer.

4. From the comparison between the traveling speed of the interface and the local velocity of the same location, it was found that the laminar fluid is entrained into the turbulent region through the interface at the leading interface regardless of the wall-normal position.

5. On the other hand, in the near-wall region, $\eta < 1.3$ at the trailing interface of the turbulent region, it was found that the turbulent fluid was crossing the interface, provoking relaminarization.

6. The critical wall-normal distance of $\eta = 1.3$, which was the limit of the relaminarization process, corresponded to 10.7 in wall unit (y^+). This result suggested that the relaminarization process was taking place in the viscous sublayer.

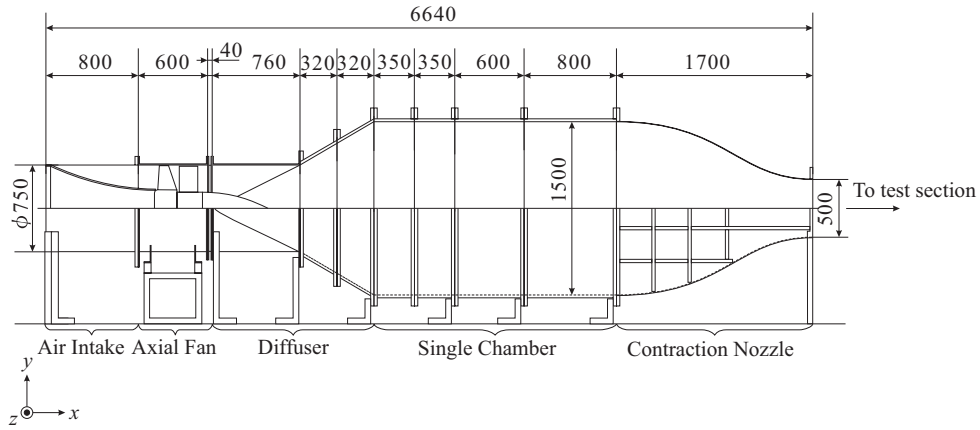

Figure 5.1 Schematic view of the blowout-type wind tunnel. (Unit:mm)

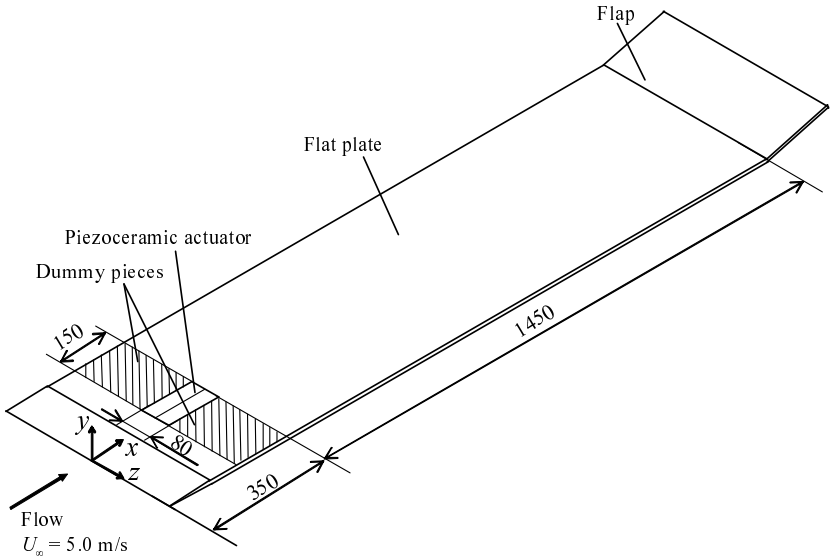

Figure 5.2 Schematic view of the flat plate with piezoceramic actuator. (Unit:mm)

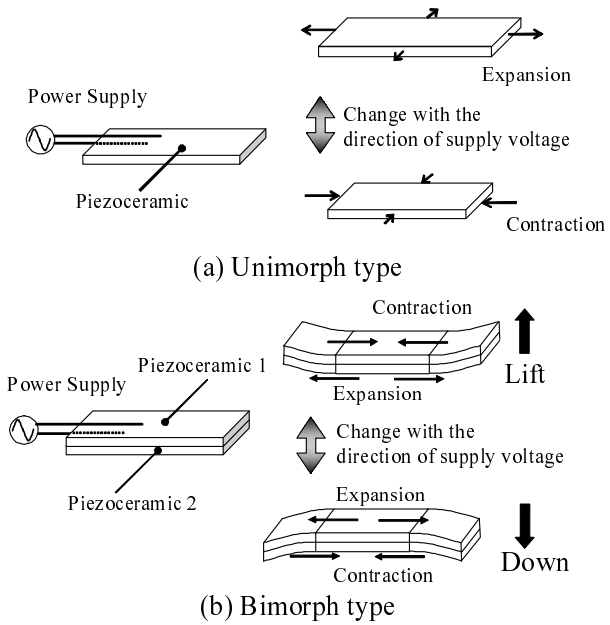

Figure 5.3 Schematic sketches of deformation of piezoceramic pieces. (a) Unimorph type and (b) bimorph type.

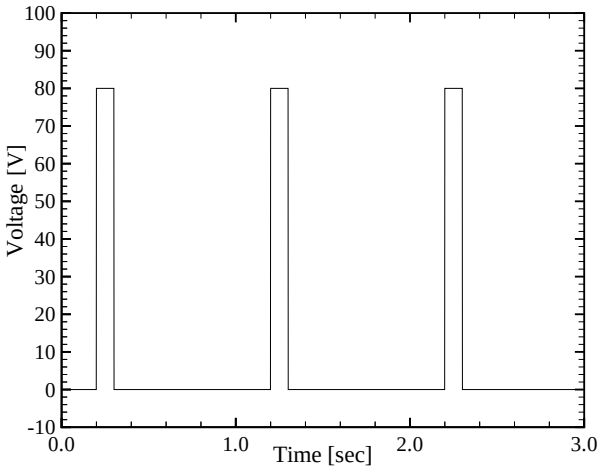

Figure 5.4 The voltage signal input to the piezoceramic pieces.

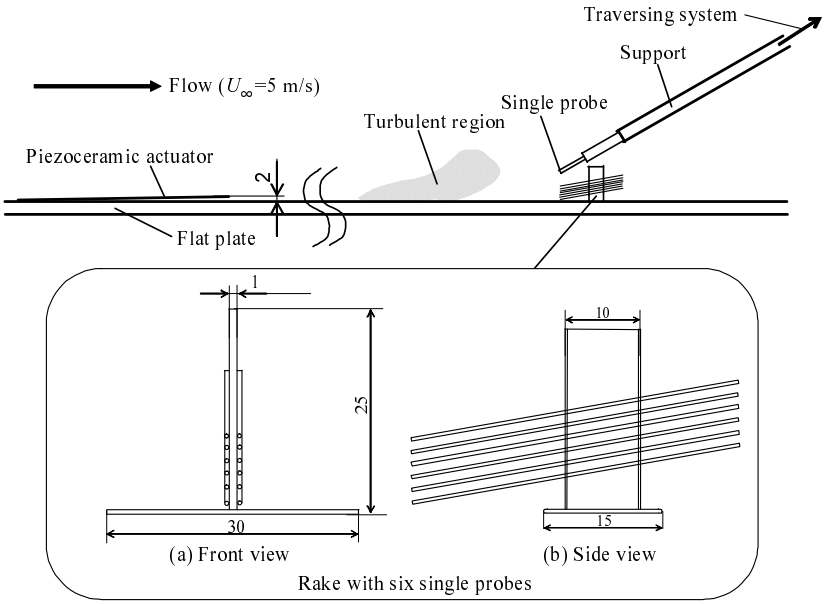

Figure 5.5 Schematic view of the hot-wire probes. (Unit:mm)

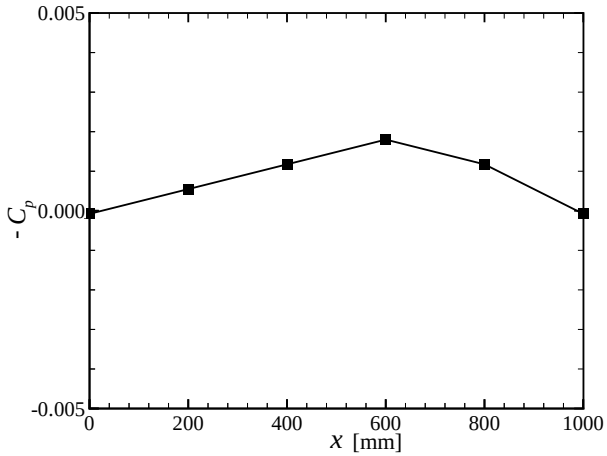

Figure 5.6 The x profile of the pressure coefficient C_p in the test section. Measurements are performed at x = 200, 400, 600, 800, and 1,000 mm. The actuator is not activated.

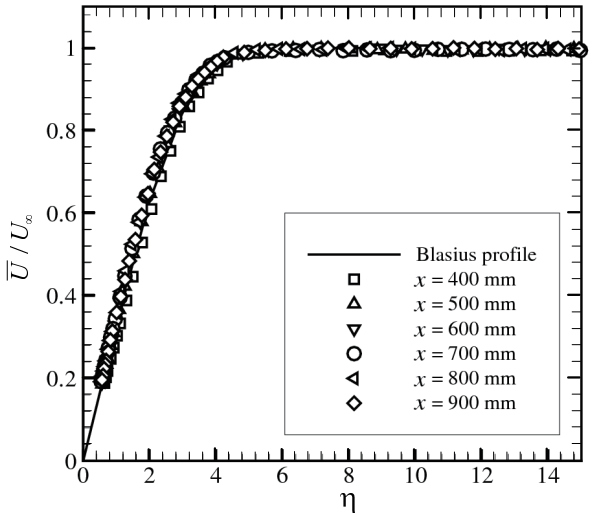

Figure 5.7 Wall-normal profiles of $\overline{U}/U_\infty$ at x = 400, 500, 600, 700, 800, 900 mm, and z = 0. The actuator is not activated. The solid line shows the Blasius profile.

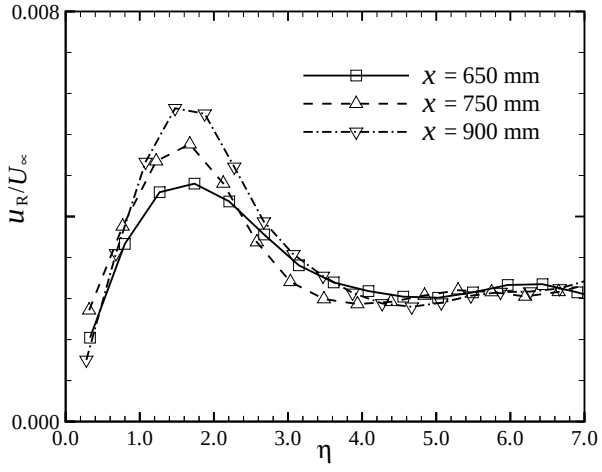

Figure 5.8 Wall-normal profiles of the RMS value of the streamwise velocity fluctuation u_R/U_∞ at x = 650, 750, 900 mm, and z = 0. The actuator is not activated.

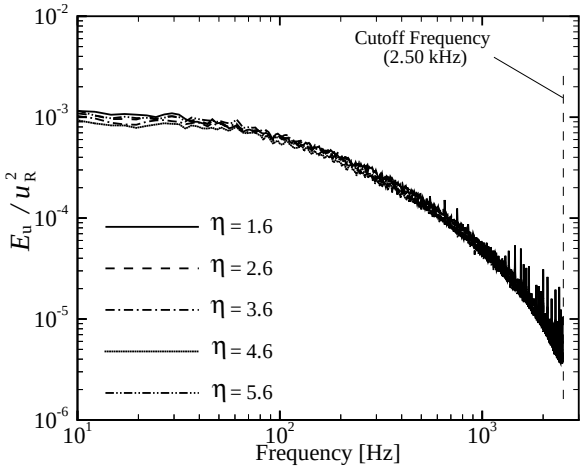

Figure 5.9 Wall-normal variation of the power spectrum of the streamwise velocity fluctuation $E_{\mathrm{u}}/u_{\mathrm{R}}^2$ at $x = 750$ mm, $\eta = 1.6$, 2.6, 3.6, 4.6, 5.6, and $z = 0$.

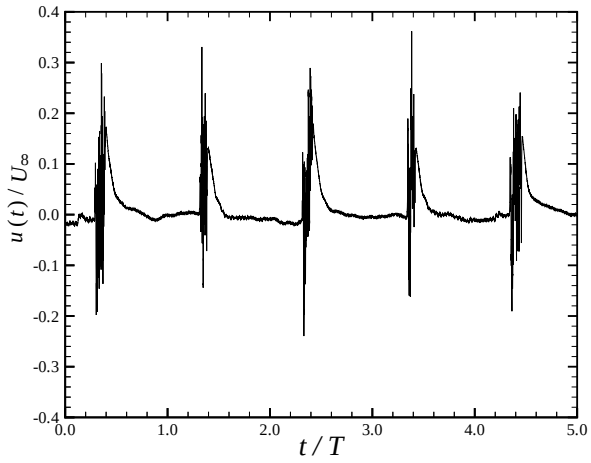

Figure 5.10 Waveform of the streamwise velocity fluctuation $u(t)/U_\infty$ at $x = 750$ mm, $\eta = 2.0$, and $z = 0$.

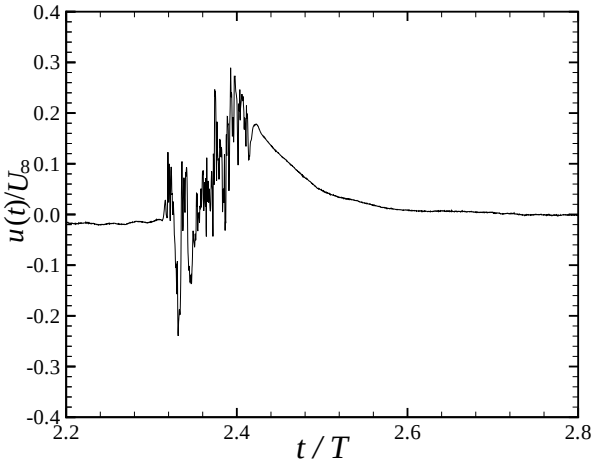

Figure 5.11 A close-up view of the waveform in Figure 5.10.

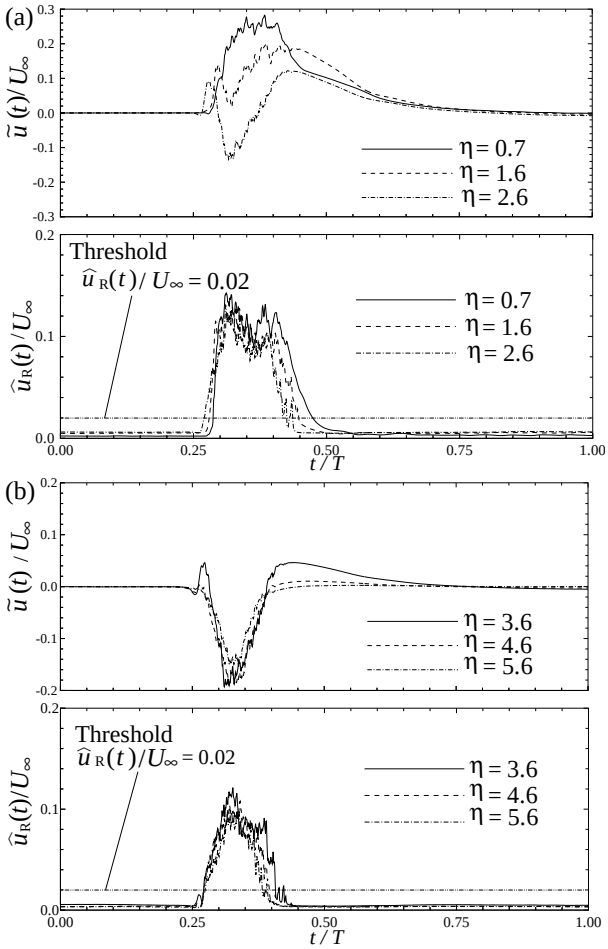

Figure 5.12 Time histories of the ensemble-averaged streamwise velocity fluctuation $\tilde{u}(t)/U_\infty$ and the intensity of the random component $\hat{u}_\mathrm{R}(t)/U_\infty$ measured at (a) $\eta =$ 0.7, 1.6, 2.6 and (b) $\eta = 3.6$, 4.6, 5.6.

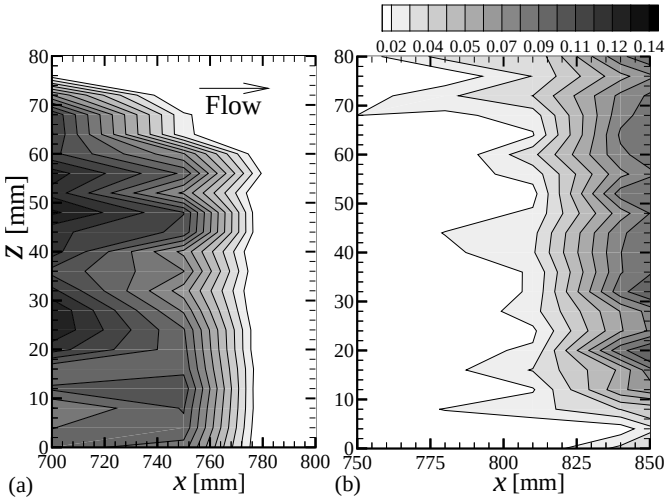

Figure 5.13 Contour maps of $\hat{u}_{\mathrm{R}}(t)/U_\infty$ in the xz-plane of $y = 2.0$ mm at $t/T = 0.33$ and $t/T = 0.65$. Flow direction is left to right.

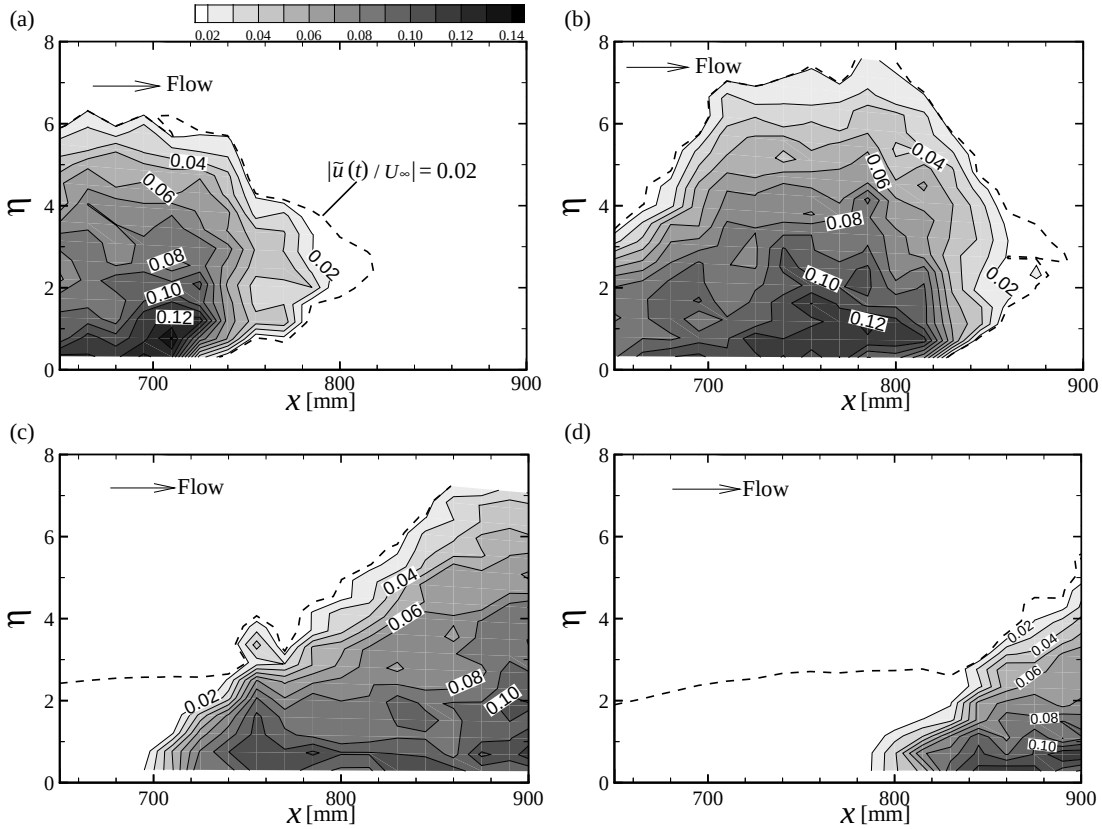

Figure 5.14 Contour maps of the intensity of the random component $\hat{u}_{\mathrm{R}}(t)/U_\infty$ in the $x\eta$-plane of $z = 0.0$. The dashed-lines indicate $|\tilde{u}(t)/U_\infty| = 0.02$. (a) $t/T = 0.31$, (b) $t/T = 0.35$, (c) $t/T = 0.45$, and (d) $t/T = 0.53$. Flow direction is left to right.

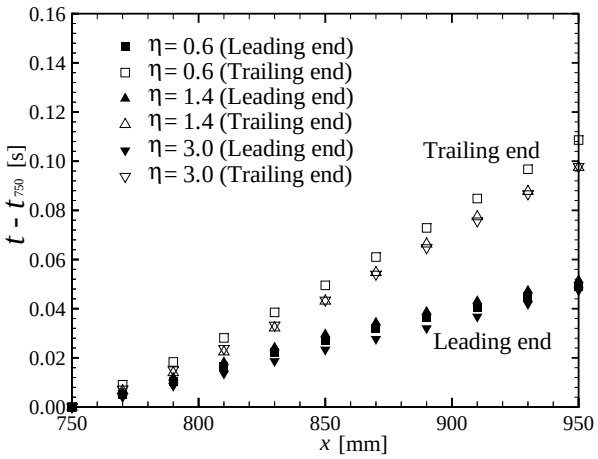

Figure 5.15 The arrival time at each streamwise station, leading end (LE) and trailing end (TE).

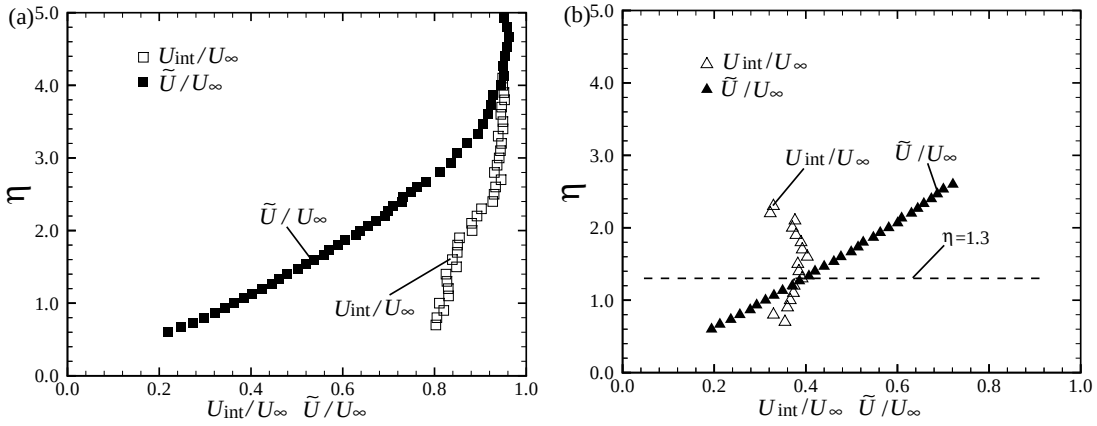

Figure 5.16 Wall-normal profiles of the traveling speeds of the interfaces $U_{\mathrm{int}}/U_\infty$ and the ensemble-averaged streamwise velocities $\tilde{U}/U_\infty$. (a) and (b) show the values measured at the leading and trailing end of the turbulent region, respectively. The measurement is performed at $x = 750$ mm and $z = 0$.

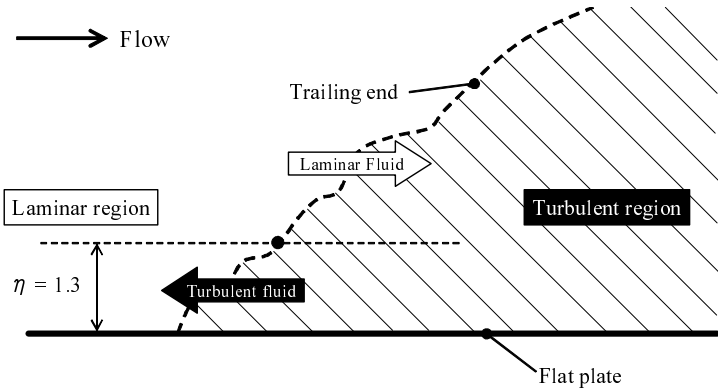

Figure 5.17 A sketch of phenomena take place at the trailing end of the turbulent region.

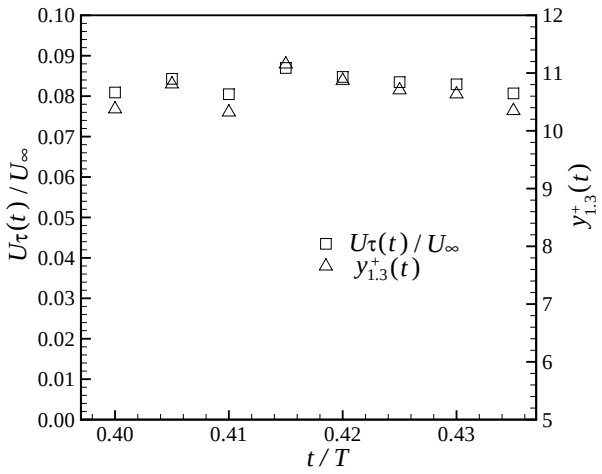

Figure 5.18 Profiles of friction velocity $U_\tau(t)/U_\infty$ and $y^+_{1.3}(t)$.

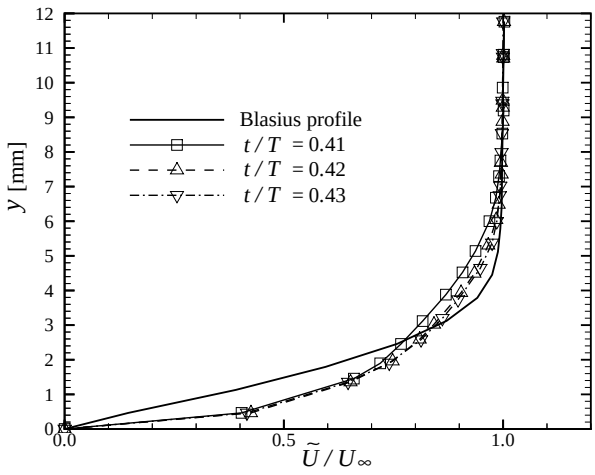

Figure 5.19 Wall-normal profiles of the ensemble-averaged streamwise velocity $\tilde{U}/U_\infty$ within the turbulent region ($t/T = 0.41$, 0.42, 0.43) measured at $x = 750$ mm and $z = 0$.

Chapter 6

Characteristics of a plane jet in flapping motion [119][120][121][122]

6.1 Introduction

In Chapters 3 to 5, the subjects (a) and (b) shown in Chapter 1 were investigated experimentally. Therefore, finally, the experiment results related to the subject (c) are described in this chapter.

The flapping motion is one of the large-scale coherent vortex structure in the self-preserving region of a plane jet [83][88][87]. The term "flapping" was named from the visual image of this phenomenon that the jet flaps as a flag does. There were almost no researches by which the entity of the flapping motion could be captured until the multi-point simultaneous measurement of the velocity in a plane jet by Sakai et al. [92]. The measured velocity field by Sakai et al. showed that there existed a pair of fluid lumps with the positive and negative streamwise velocity fluctuation on the opposite sides of the jet centerline, and the signs of the fluid lumps changed alternately as time proceeds. Furthermore, on the basis of the result of Karhumen-Loève (KL) expansion, a new interpretation of the coherent structure model in the self-preserving region of a plane jet was given from the combination of "flapping motion" and "puffing motion" [104]. However, the characteristics of the flapping phenomena are still not clear.

From this point of view, in this study, the detail characteristics of the flapping motion are investigated. Firstly, the new method to discriminate the flapping motion and determine the intermittency function about the arising of the flapping motion by using the continuous wavelet transform with Gabor mother wavelet is developed. Secondly, the ensemble-averaged velocity and the pressure field on the basis of the intermittency function obtained by the present new method is confirmed. Thirdly, the turbulent energy budget of a plane jet in the flapping motion is estimated. Finally, the interval time and the duration time of the flapping motion are estimated.

6.2 Experiment setup and procedure

6.2.1 Experiment setup

The experiment is performed in a plane jet shown in Figure 2.11. The experimental apparatus, coordinate system and conditions are same with the experiment described in Chapter 3.

In this study, two I-type hot-wire probes (hereafter called "detectors") are set at the intermittent region ($x_1/d = 40$) to detect the flapping motion as shown in Figure 6.1. In addition, the combined probe shown in Figure 2.18 for the simultaneous measurement of the velocity and pressure which is connected to the traverse system is set in the measurement region. By use of the stepping motor to move the traverse system, the high accurate spatial measurement is realized (accuracy of positioning is less than $\pm$ 0.1 mm).

6.2.2 Determination of flapping frequency

Several techniques to determine the frequency of the flapping motion (f_p) in the self-preserving region of a plane jet have been suggested. In this study, we estimate f_p by the peak frequency of the power spectrum of the cross-streamwise velocity fluctuation on the jet centerline because the damping characteristic of the flapping frequency toward streamwise direction can be evaluated more accurately than other methods. Here, the damping characteristic of the flapping frequency toward the streamwise direction means that the flapping frequency is proportional to the - 3/2 power law [123] for the dimensionless value of the streamwise location (x_1/d, defined as X). This characteristic can be derived by some characteristics of the jet in the following; (1) the downstream variation of the half width of the cross-streamwise profile of the mean streamwise velocity b, i.e., b is proportional to X ($b \propto X$); (2) the downstream variation of the streamwise velocity on the jet centerline, i.e., $\overline{U}_\mathrm{c}$ is proportional to $X^{-0.5}$ ($\overline{U}_\mathrm{c} \propto X^{-0.5}$); (3) Strouhal number S_t, which defined as $f_\mathrm{p} b/\overline{U_\mathrm{c}}$, in the self-preserving region is constant (S_t = Const.).

6.2.3 Extraction of flapping motion

In the previous study [92], the existence of the flapping motion was confirmed by the multi-point simultaneous measurement of the velocity. However, in the previous study, the flapping motion was captured visually. Therefore, it was difficult to analyze the phenomenon statistically because the visual capturing of the phenomenon was involved

in the subjective view by the observer. From this point of view, the new method to extract the flapping motion by using the continuous wavelet transform with Gabor mother wavelet is developed to eliminate the subjective view of the observer in the determination of the time which the flapping motion is arising.

The procedure by the present new method is shown in the following and Figure 6.2. Firstly, the frequency of the flapping motion f_{p} at the measurement point ($x_1/d = 40$) is estimated as the peak frequency of the power spectrum of the cross-streamwise velocity fluctuation on the jet centerline. Secondly, by applying the continuous wavelet transform with Gabor mother wavelet (see Equations (6.1) and (6.2)) to the signals of streamwise velocity fluctuations measured by two I-type hot-wire probes ($u_1(t)$ and $u_2(t)$ in Figure 6.2 (1)), the real parts of the wavelet component which corresponds to the flapping frequency f_{p} (defined as $w_1(t)$ and $w_2(t)$ in Figure 6.2 (2)) are extracted. Thirdly, the product of $w_1(t)$ and $w_2(t)$ which is defined as the detection function $D(t)$ (shown in Figure 6.2 (3)) is calculated, then the intermittency function $I(t)$ is decided by the suitable negative threshold. Finally, from the signs of $u_1(t)$ and $u_2(t)$ and the periodicity of $I(t)$, the flapping intermittency function $I_{\mathrm{f}}(t)$ is obtained. In this study, if the interval of the central time when $I(t)$ becomes 1 is in the range 0.35 - 0.65 times T_p (hereafter, this range is called "periodicity range", and T_{p} is inverse of f_{p} which is named the flapping period), jet is judged as being in the flapping motion. Further, the "negative threshold" is chosen so as for the ratio of the turbulent intensity in the flapping motion to that in the total measurement time to become 23 %. This ratio is equal to the energy contribution ratio of the first mode of the KL expansion investigated by Sakai et al. [100]. In this study, the continuous wavelet transform with Gabor mother wavelet as follows is used,

$$W(\alpha,\beta) = \frac{1}{\sqrt{\alpha}} \int \overline{\phi(\frac{t-\beta}{\alpha})} s(t) dt \tag{6.1}$$

$$\phi(t) = \frac{1}{2\sqrt{\pi}\sigma} \exp(-\frac{t^2}{\sigma^2}) \exp(-it) \tag{6.2}$$

where, α: scale parameter, β: time parameter, $s(t)$: time series signal, i: imaginary unit, $\phi(t)$: Gabor function, σ: parameter to decide the frequency resolution and the time resolution.

6.3 Results and discussions

6.3.1 Base flow

The cross-streamwise profiles of the streamwise mean velocity $\overline{U}$, the RMS value of the streamwise velocity fluctuation u', the RMS value of the pressure fluctuation p', and the Reynolds stress -$\overline{uv}$ were shown in Figures 2.21, 2.22, 2.23, and 2.24 in Chapter 2, respectively.

6.3.2 Frequency of flapping motion

The frequency of the flapping motion at $x_1/d = 40$ which is estimated by the method described above is shown in Figure 6.3. The ordinate shows the normalized flapping frequency S_t ($= f_{\mathrm{p}}b/\overline{U}_c$) and the abscissa shows x_2/b. The dash-dot-dot line in Figure 6.3 indicates the normalized flapping frequency $S_{t\mathrm{P0}}$ which is estimated by using the peak frequency of the power spectrum of the pressure fluctuation on the jet centerline f_{pP0}.

It is found that S_t is almost constant in the range $0 \leq x_2/b \leq 0.7$ and its value is 0.146. Further, it is also found that the $S_{t\mathrm{P0}}$ equals to S_t except for the outer region of the jet. Here, it can be assumed that f_{pP0} shows the frequency of the passing of vortex on the jet centerline because the point which has local minimum value of the pressure corresponds to the vortex core [124][125]. Therefore, obtained results express the vortex structure model of the flapping motion presented in the previous study by Sakai et al. [92] shown in Figure 6.4. Further, it is also found that the estimated flapping frequency is valid. In the following investigations, the normalized flapping frequency S_t is set as 0.146.

6.3.3 Velocity and pressure field in flapping motion

Figure 6.5 shows the contour map of the phase-averaged streamwise mean velocity $\hat{U}$. The contrasting density in the figure shows the $\hat{U}$ normalized by $\overline{U}_{\mathrm{c}}$, the ordinate shows x_2/b, and the abscissa shows the time from the time when the flapping motion starts (i.e., $t = 0$ means the time when the flapping phenomenon starts) normalized by the flapping period T_{p}.

Figure 6.6 shows the contour map of the phase-averaged streamwise velocity fluctuation $\hat{u}$. The contrasting density in the figure shows the $\hat{u}$ normalized by u'_{c}, the ordinate and abscissa are the same as those in Figure 6.5.

Figure 6.7 shows the contour map of the phase-averaged cross-streamwise velocity fluc-

tuation $\hat{v}$. The contrasting density in the figure shows the $\hat{v}$ normalized by v'_{c}, the ordinate and abscissa are the same as those in Figure 6.5.

From the results of Figures 6.5 - 6.7, the following characteristics of the flapping motion are verified; (1) a pair of fluid lumps with the positive and negative streamwise velocity fluctuation exists on the opposite side of the jet centerline; (2) the signs of the velocity fluctuation of those fluid lumps change alternately as the time advances (t becomes large). Therefore, it is confirmed that the present method is available to extract the flapping motion by use of the continuous wavelet transform and the suitable negative threshold.

Figure 6.8 shows the contour map of the phase-averaged pressure fluctuation $\hat{p}$. The contrasting density in the figure shows the $\hat{p}$ normalized by p'_{c}, the ordinate and abscissa are the same as those in Figure 6.5. On the basis of the assumption by Bradshaw et al. [124] and Shirahama et al. [125], it is found that the phase-averaged pressure field during the flapping motion indicates the presence of a vortex structure, interpreted as a combination of the flapping and the puffing motion in the self-preserving region of a plane jet.

6.3.4 Turbulent energy budget in flapping motion

In this section, the influence of the arising of the flapping motion on the flow characteristics is investigated by estimating the turbulent energy budget. Firstly, it is estimated by using the phase-averaged velocity and pressure field when $t/T_{\mathrm{p}} = 0.20$ at which the high speed fluid passes, and 0.70 at which low speed fluid passes. Secondly, it is estimated by using averaged velocity and pressure field while the flapping motion is arising ($t/T_{\mathrm{p}} = 0.0$ - 1.0).

Turbulent energy budget of $t/T_{\mathrm{p}} = 0.20$ and 0.70

Figure 6.9 shows the cross-streamwise profiles of the convection term at $t/T_{\mathrm{p}} = 0.20$ and 0.70. In the following, only the profiles in the range $x_2/b \geq 0$ will be shown because it was found that the averaged velocity and the pressure filed were symmetrical to the jet center line in previous chapters. The ordinate shows the value of the convection term normalized by $\overline{U}_{\mathrm{c}}^3/b$ and the abscissa shows x_2/b. The solid, dashed, and dot-dash line show the profile of $t/T_{\mathrm{p}} = 0.20$, 0.70 and the whole time averaged value shown in Chapter 2, respectively. It is found that the convection of the turbulent energy is enhanced when $t/T_{\mathrm{p}} = 0.20$ at which the high speed fluid passes and reduced when $t/T_{\mathrm{p}} = 0.70$ at which low speed fluid passes.

Figure 6.10 shows the cross-streamwise profiles of the production term at $t/T_\mathrm{p} = 0.20$ and 0.70. The ordinate shows the value of the production term normalized by $\overline{U}_\mathrm{c}^3/b$. The abscissa and the meaning of the lines are same with those in Figure 6.10. It is found that the production of turbulent energy is enhanced when $t/T_\mathrm{p} = 0.20$. However, it is almost same with the profile of whole time averaged value when $t/T_\mathrm{p} = 0.70$ except for the inner side of the jet ($x_2/b \leq 0.5$).

Figure 6.11 shows the cross-streamwise profiles of the diffusion term at $t/T_\mathrm{p} = 0.20$ and 0.70. The ordinate shows the value of the diffusion term normalized by $\overline{U}_\mathrm{c}^3/b$. The abscissa and the meaning of the lines are same with those in Figure 6.10. It is found that the diffusion of the turbulent energy from the inner side of the jet ($0 \leq x_2/b \leq 0.65$) to the outer region is enhanced when $t/T_\mathrm{p} = 0.20$ and this turbulent energy diffusion from the inner side to outer side also can be observed when $t/T_\mathrm{p} = 0.70$. However, the turbulent energy diffusion from the outer side to near the jet centerline which can be observed in the whole time averaged profile is not observed in those profiles.

Figure 6.12 shows the cross-streamwise profiles of the turbulent diffusion term at t/T_p = 0.20 and 0.70. The ordinate shows the value of the turbulent diffusion term normalized by $\overline{U}_\mathrm{c}^3/b$. The abscissa and the meaning of the lines are same with those in Figure 6.10. It is found that there is a big difference between the profile of $t/T_\mathrm{p} = 0.20$ and 0.70. Further, it can be observed in both profiles that the diffusion of the turbulent energy from the inner side of the jet to the outer region arising.

Figure 6.13 shows the cross-streamwise profiles of the pressure diffusion term at t/T_p = 0.20 and 0.70. The ordinate shows the value of the pressure diffusion term normalized by $\overline{U}_\mathrm{c}^3/b$. The abscissa and the meaning of the lines are same with those in Figure 6.10. It is found that the profile of pressure diffusion term strongly depends on the flow state caused by the flapping motion. The turbulent energy is diffused from the outer side of the jet to inner side. The quantity of the turbulent energy diffusion by pressure diffusion is smaller than whole time averaged value both in $t/T_\mathrm{p} = 0.20$ and 0.70.

Turbulent energy budget for the duration of t/T_p = 0.0 - 1.0

Figure 6.14 shows the cross-streamwise profiles of convection term while the flapping motion is arising. The ordinate shows the value of convection term normalized by $\overline{U}_\mathrm{c}^3/b$ and the abscissa shows x_2/b. The solid line and the dash-dot-dot lines show the profile of convection term while the flapping motion is arising and the whole time averaged value shown in Chapter 2, respectively. It is found that the profile of the convection term

while the flapping motion is almost consistent with that of whole time averaged profile. Therefore, the arising of the flapping motion have no big influence on the convection of the turbulent energy.

Figure 6.15 shows the cross-streamwise profiles of production term while the flapping motion is arising. The ordinate shows the value of production term normalized by $\overline{U}_c^3/b$. The abscissa and the meaning of the solid line and the dash-dot-dot line are same as in Figure 6.14. The dashed-line shows the profile of production term while no flapping motion is arising. From Figure 6.15, it is found that the profile of the production term while the flapping motion arising is bigger than those of the whole time averaged profile and while the flapping motion is not arising in the range $x_2/b \geq 0.5$. Therefore, it can be concluded that the arising of the flapping enhances the production of the turbulent energy especially in the outer region of the jet.

Figure 6.16 shows the cross-streamwise profiles of diffusion term while the flapping motion is arising. The ordinate shows the value of diffusion term normalized by $\overline{U}_c^3/b$. The abscissa and the meaning of the solid line, dash-dot-dot line are same with Figure 6.14. It can observed that the diffusion of the turbulent energy is enhanced while the flapping motion is arising. It also can be found that the turbulent energy is transported to more outer region of the jet while the flapping motion is arising.

Figure 6.17 shows the cross-streamwise profiles of the turbulent diffusion term while the flapping motion is arising. The ordinate shows the value of turbulent diffusion term normalized by $\overline{U}_c^3/b$. The abscissa and the meaning of the solid line, dash-dot-dot line, and dashed-line are same with Figure 6.15. It is found that the turbulent energy is transported to more outer region of the jet while the flapping motion is arising. Further, the loss of the turbulent energy in the inner side of the jet is enhanced while the jet is not flapping. Therefore, it is concluded that the flapping motion has a role to transport the turbulent energy to the outer region of the jet by the turbulent diffusion process and it makes the loss of the turbulent energy in the inner side of the jet small.

Figure 6.18 shows the cross-streamwise profiles of the pressure diffusion term while the flapping motion is arising. The ordinate shows the value of pressure diffusion term normalized by $\overline{U}_c^3/b$. The abscissa and the meaning of the solid line, dash-dot-dot line, and dashed-line are same with Figure 6.15. The transport of the turbulent energy to the inner side of the jet becomes small while the jet is flapping. In addition, it is enhanced while the jet is not flapping.

From Figures 6.16 to 6.18, it can be concluded about the diffusion process of the turbulent energy that the arising of the flapping motion enhances the transport of the

turbulent energy to the outer region of the jet by the combination of the increasing of the transport to the outer region by the turbulent diffusion, and the decreasing of the transport to the inner region of the jet by the pressure diffusion.

6.3.5 Interval and duration time of flapping motion

Figure 6.19 shows the interval time between the arising of one flapping motion and next arising. The ordinate indicates the relative number of each interval time in the whole measurement time (about 262 seconds) and the abscissa indicates the interval time of the flapping motion T normalized by the flapping frequency f_{p}. The meaning of symbols in the figure are as follows; ■: $\sigma = 6$, ▲: $\sigma = 1$, and ▼: $\sigma = 4$.

Figure 6.20 shows the dependence of estimated interval time on the periodicity range. The ordinate and the abscissa are same with those in Figure 6.19. The solid, dashed, and dot-dash line indicate condition 1 (the periodicity range is 0.35 - 0.65 times T_p, default), condition 2 (the periodicity range is 0.40 - 0.60 times T_p), and condition 3 (the periodicity range is 0.45 - 0.55 times T_p), respectively.

From Figures 6.19 and 6.20, it is found that the average interval time of the flapping motion is about 6.7 times the flapping period (which correspond to 0.24 seconds) and it arises at random. Further, the profiles are almost same qualitatively for various σ and periodicity range. Therefore, the estimated results do not strongly depend on those parameters.

Figure 6.21 shows the duration time of one flapping motion. The ordinate indicates the relative number of each duration time in the whole measurement time and the abscissa indicates the duration time normalized by the flapping frequency f_{p}. The meaning of symbols in the figure are the same as those in Figure 6.19.

Figure 6.22 shows the dependence of estimated duration time on the periodicity range. The ordinate and the abscissa are same with those in Figure 6.21. The meaning of the lines are same with those in Figure 6.20.

From Figures 6.21 and 6.22, it is found that the most part of the flapping motion continued only 1.0 or 1.5 times the flapping period T_{p} and the one that continues over 3.0 times the flapping period is very few. Further, the average duration time of the flapping motion is about 1.7 times the flapping period T_{p}. In addition, it is also found that the estimated results do not strongly depend on σ and the periodicity range.

Figure 6.23 shows the relation between the duration time of one flapping motion and the arising interval of the flapping motion. If the plot in the figure is at (duration, interval)

= (1.0 T_p, 60 T_p), it means the flapping motion continues 1.0 T_p and next flapping arises after 60 T_p. The ordinate shows the interval time and the abscissa shows the duration time. Figure 6.23 indicates that there is a negative correlation between the interval time and duration time. Therefore, it can be concluded that the next flapping starts soon after long duration time of flapping and the long interval time is observed only after short duration.

Finally, we investigate the two-points velocity correlation by use of the detectors. It is found that the value of two-points correlation is equal to -0.15. Note that this negative sign of the correlation is one of the characteristics of a plane jet observed by previous studies. On the other hand, it is equal to -0.33 during the time which the flapping motion is arising and -0.09 during the time which the flapping motion is not arising. These results indicate that the flapping motion plays an important role to the properties of a plane jet although it is rare phenomenon.

6.4 Conclusions

In this chapter, the detail characteristics of the flapping motion are investigated. Firstly, the new method to discriminate the flapping motion and determine the intermittency function about the arising of the flapping motion by using the continuous wavelet transform with Gabor mother wavelet is developed. Secondly, the ensemble-averaged velocity and pressure field on the basis of the intermittency function obtained by the present new method is confirmed. Thirdly, the turbulent energy budget of a plane jet in the flapping motion is estimated. Finally, the interval time and the duration time of the arising of the flapping motion are estimated. The results are summarized as follows.

1. The new method to extract the flapping motion is developed by using continuous wavelet transform and the validity of this new method is confirmed.

2. The phase-averaged pressure field during the flapping motion indicates the existence of a coherent vortex structure, interpreted as a combination of flapping and puffing motion in the self-preserving region of the jet.

3. The arising of flapping motion enhances the production of the turbulent energy especially in the outer region of the jet and transportation of the turbulent energy to the outer region.

4. The enhancing of the transportation of the turbulent energy to the outer region is

caused by the increasing of the transportation of the turbulent energy to the outer region by turbulent diffusion process and the decreasing of it to the inner side by pressure diffusion process.

5. The flapping motion arises at random and the average interval time of the arising of it is about 6.7 times the flapping period.

6. The average duration time of a flapping motion is about 1.7 times the flapping period and the one that continues over 3.0 times the flapping period is very few.

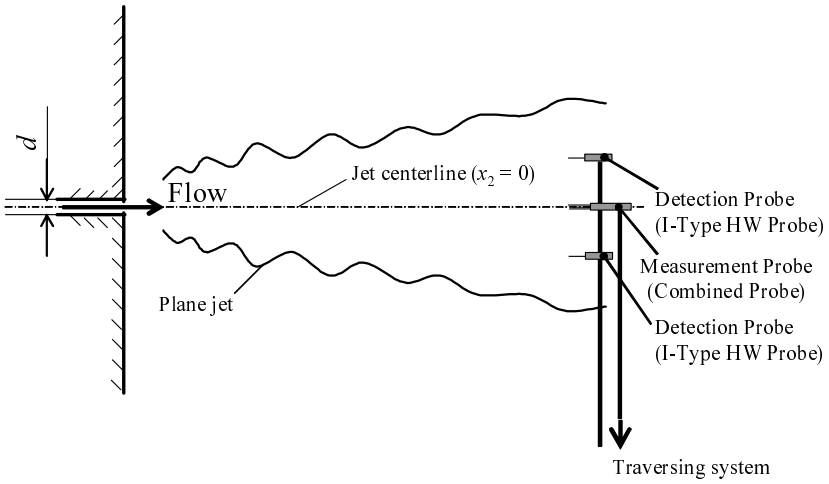

Figure 6.1 Schematic view of measurement apparatus.

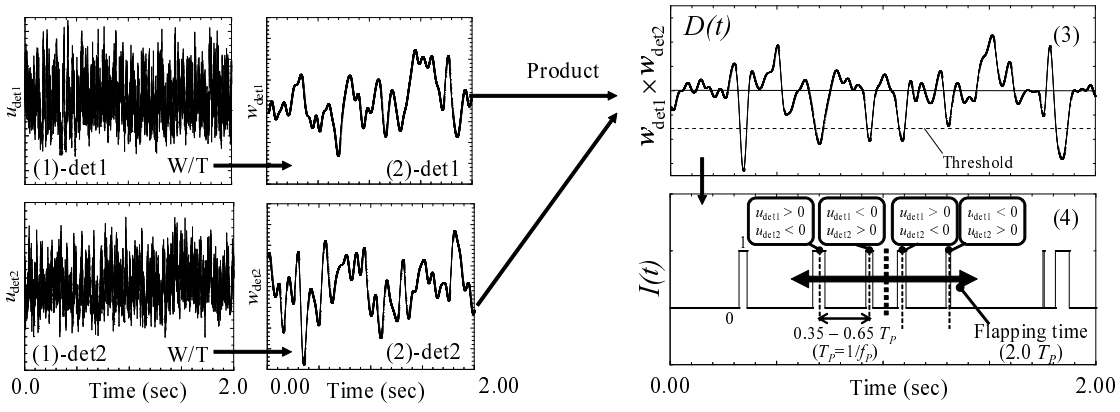

Figure 6.2 Signal processing for flapping/non-flapping decision. "W/T" means wavelet transform.

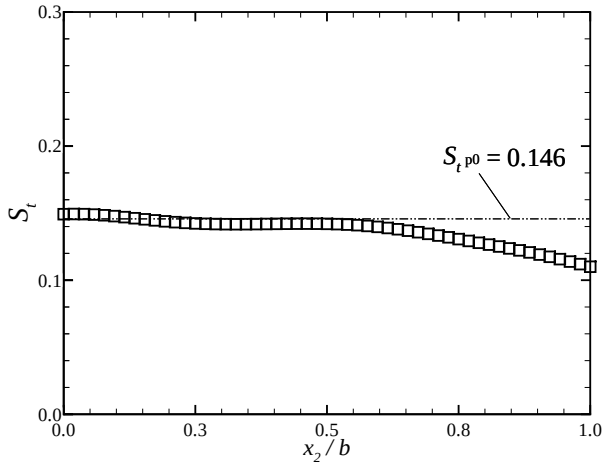

Figure 6.3 Cross-streamwise profile of Strouhal number S_t.

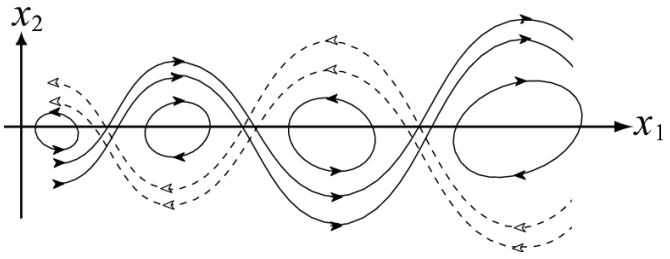

Figure 6.4 First mode model of vortex structure by the KL expansion in the self-preserving region of plane jet [92].

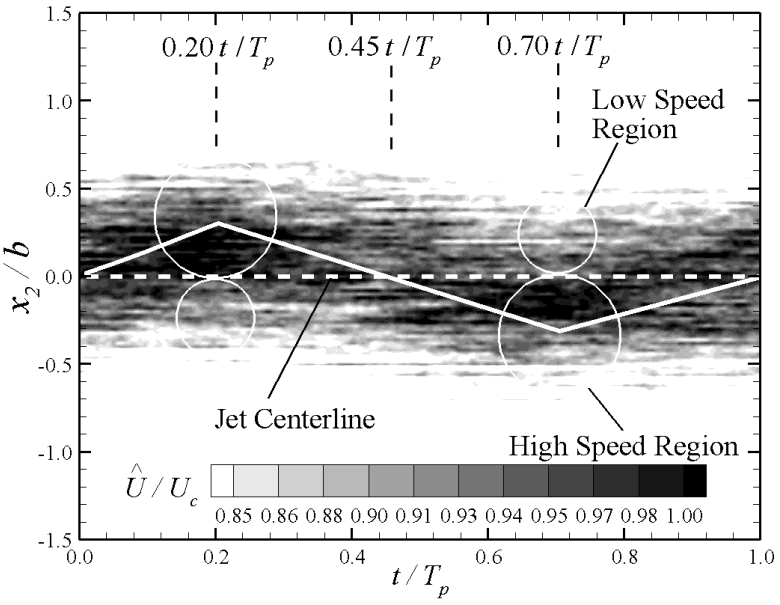

Figure 6.5 Contour map of phase-averaged streamwise velocity $\hat{U}$.

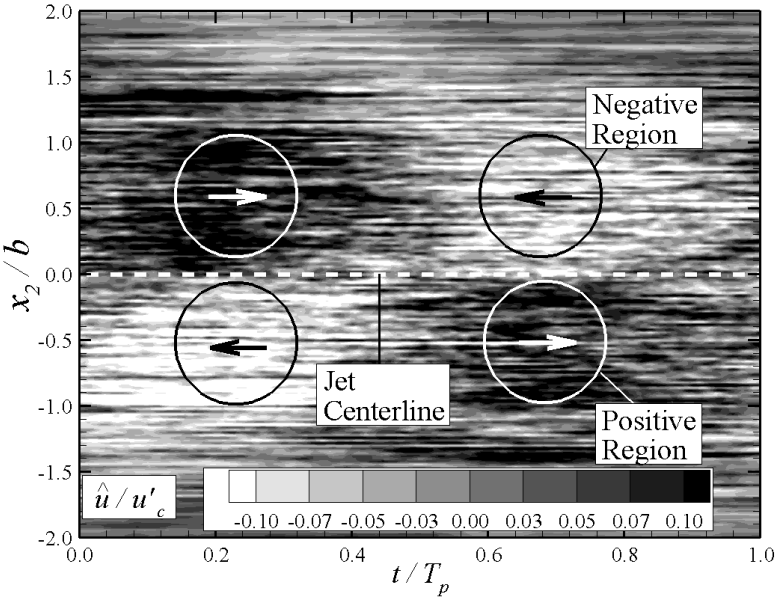

Figure 6.6 Contour map of phase-averaged streamwise velocity fluctuation $\hat{u}$.

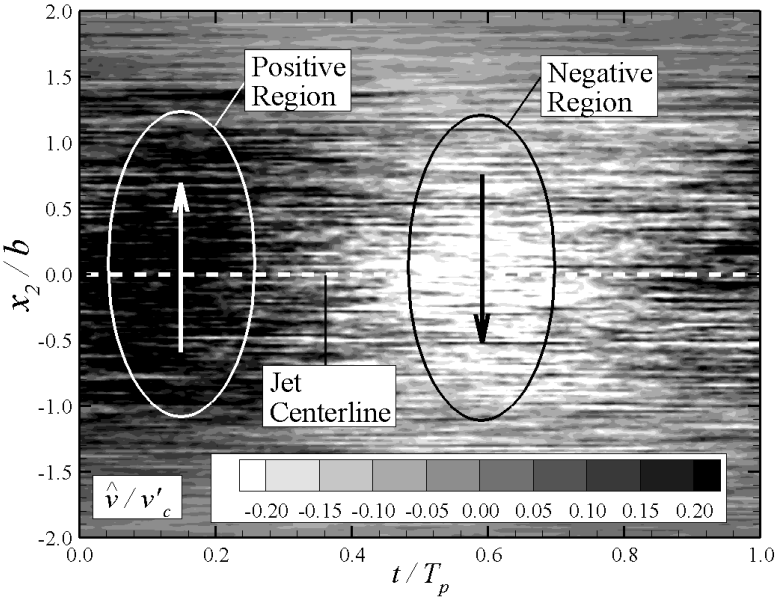

Figure 6.7 Contour map of phase-averaged cross-streamwise velocity fluctuation $\hat{v}$.

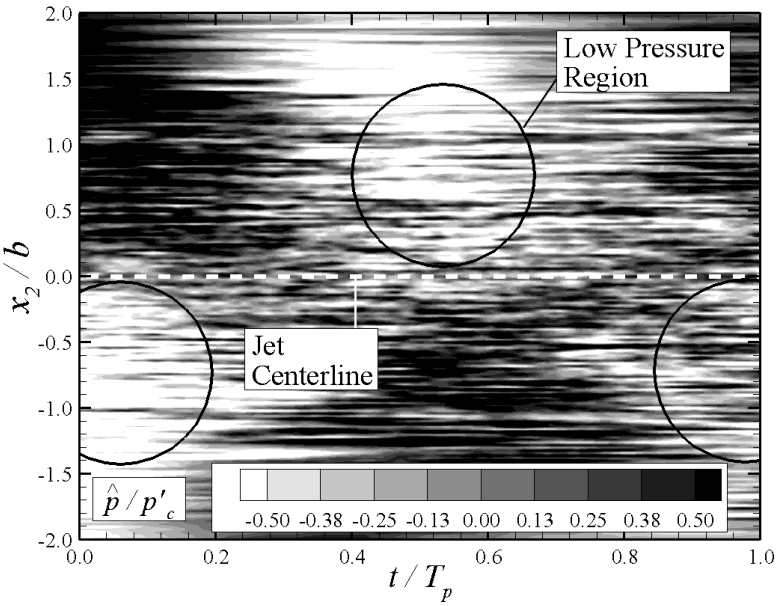

Figure 6.8 Contour map of phase-averaged pressure fluctuation $\hat{p}$.

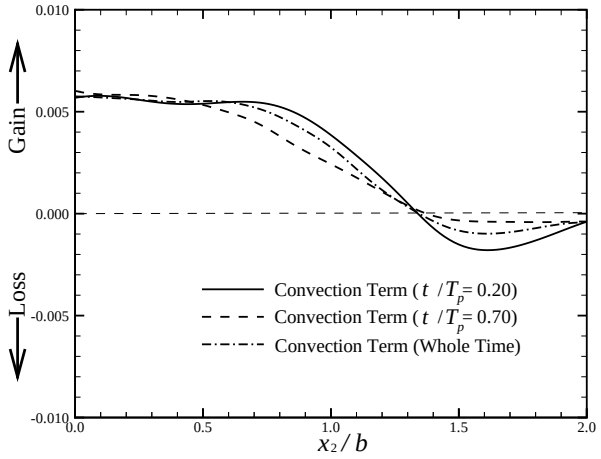

Figure 6.9 Cross-streamwise profiles of convection term at $t/T_{\mathrm{p}} = 0.20$ and 0.70.

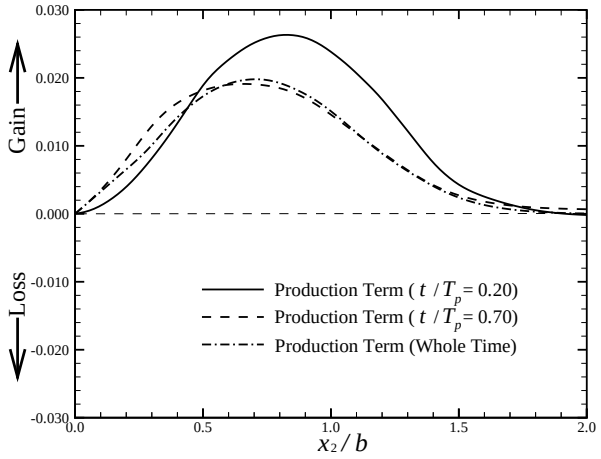

Figure 6.10 Cross-streamwise profiles of production term at $t/T_{\mathrm{p}} = 0.20$ and 0.70.

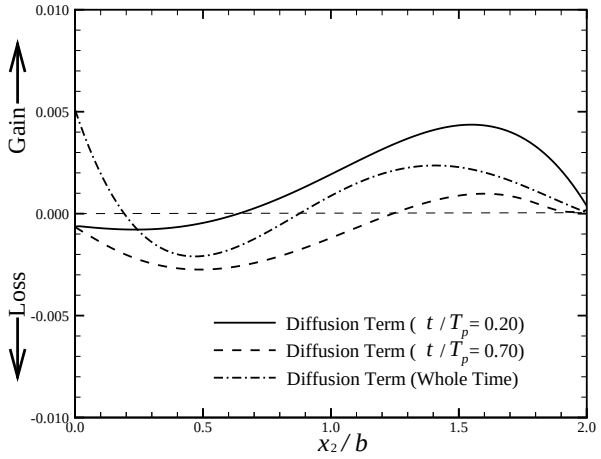

Figure 6.11 Cross-streamwise profiles of diffusion term at $t/T_{\mathrm{p}} = 0.20$ and 0.70.

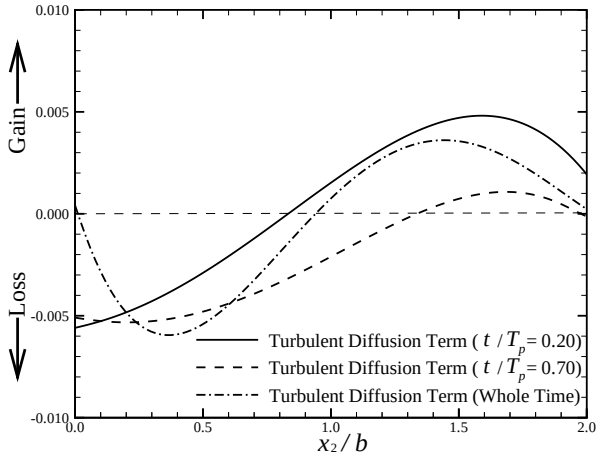

Figure 6.12 Cross-streamwise profiles of turbulent diffusion term at $t/T_{\mathrm{p}} = 0.20$ and 0.70.

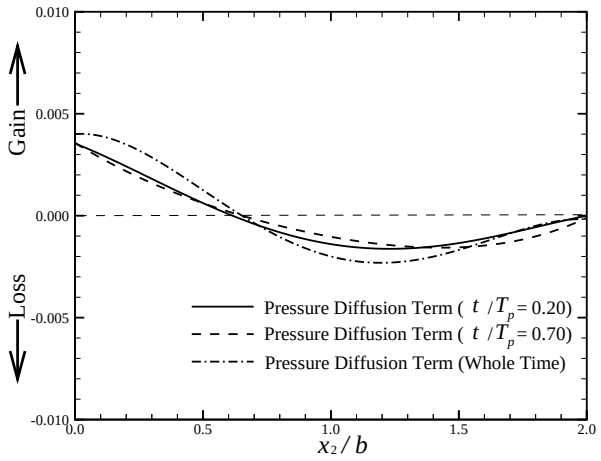

Figure 6.13 Cross-streamwise profiles of pressure diffusion term at $t/T_{\mathrm{p}} = 0.20$ and 0.70.

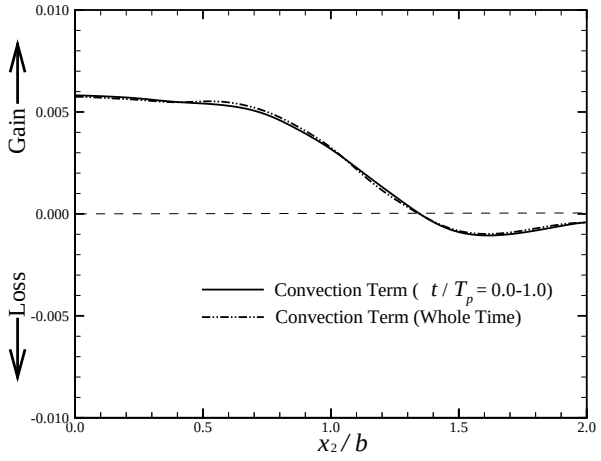

Figure 6.14 Cross-streamwise profiles of convection term while flapping motion arising ($t/T_{\mathrm{p}} = 0.0$ - 1.0).

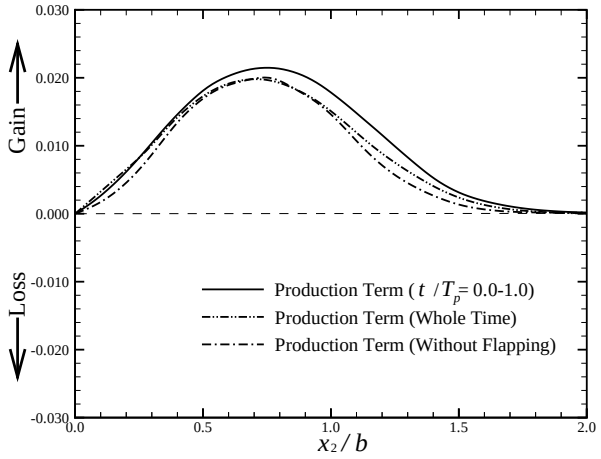

Figure 6.15 Cross-streamwise profiles of production term while flapping motion arising ($t/T_{\mathrm{p}} = 0.0$ - 1.0).

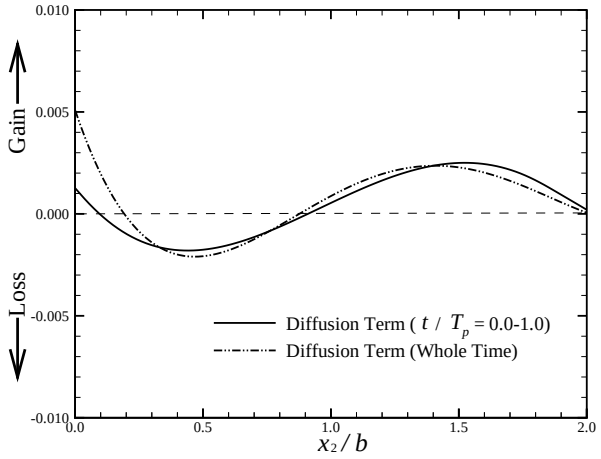

Figure 6.16 Cross-streamwise profiles of diffusion term while flapping motion arising ($t/T_{\mathrm{p}} = 0.0$ - 1.0).

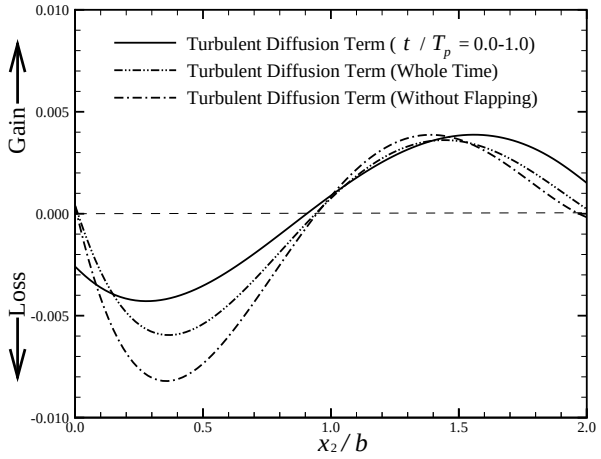

Figure 6.17 Cross-streamwise profiles of turbulent diffusion term while flapping motion arising (t/T_p = 0.0 - 1.0).

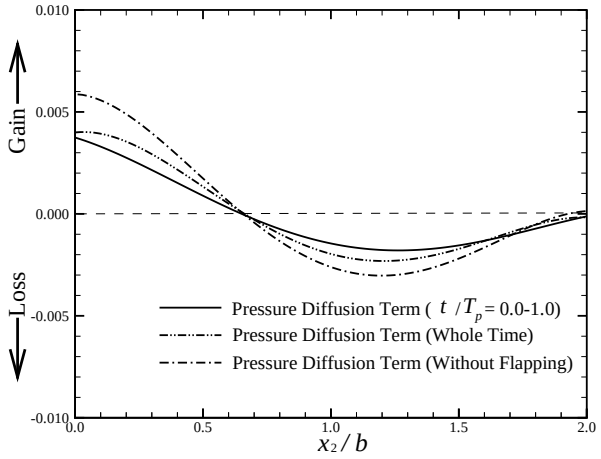

Figure 6.18 Cross-streamwise profiles of pressure diffusion term while flapping motion arising (t/T_p = 0.0 - 1.0).

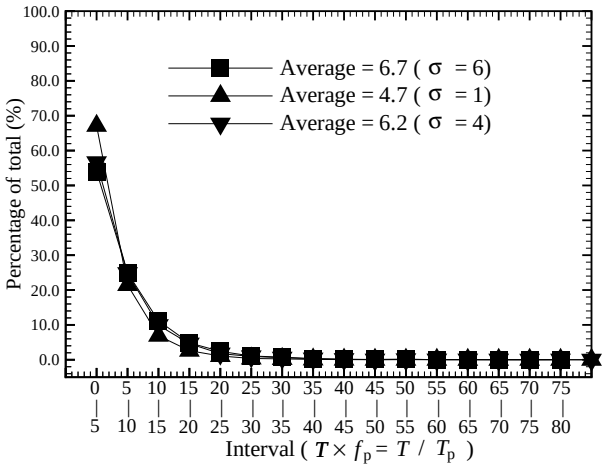

Figure 6.19 Interval time of the flapping motion.

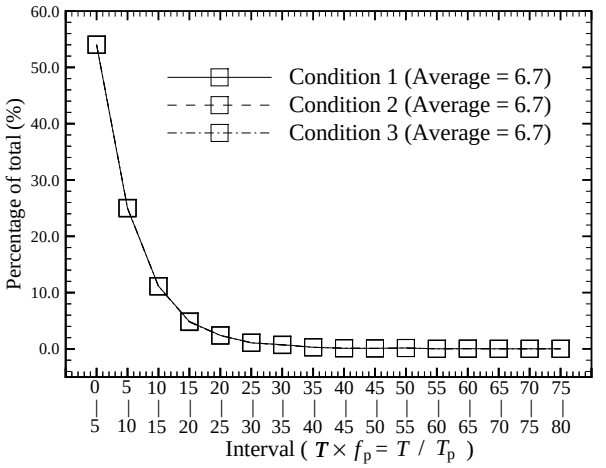

Figure 6.20 Dependence of estimated interval time on the periodicity range. Condition 1, 2, and 3 means 0.35 - 0.65 T_p, 0.40 - 0.60 T_p, and 0.45 - 0.55 T_p, respectively.

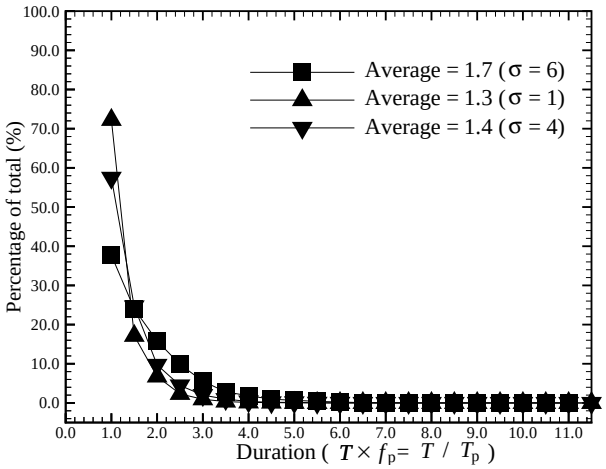

Figure 6.21 Duration time of the flapping motion.

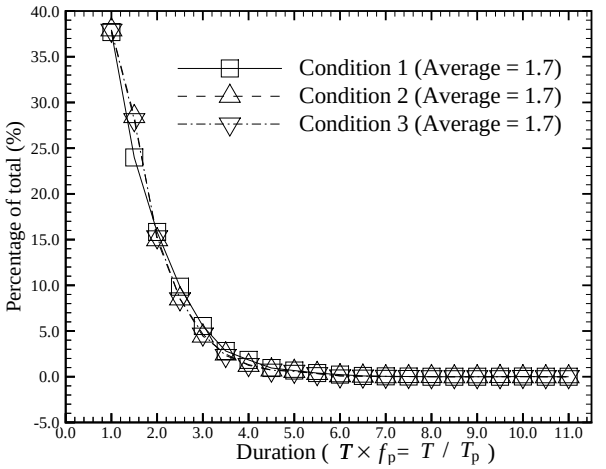

Figure 6.22 Dependence of estimated duration time on the periodicity range. Condition 1, 2, and 3 means 0.35 - 0.65 T_p, 0.40 - 0.60 T_p, and 0.45 - 0.55 T_p, respectively.

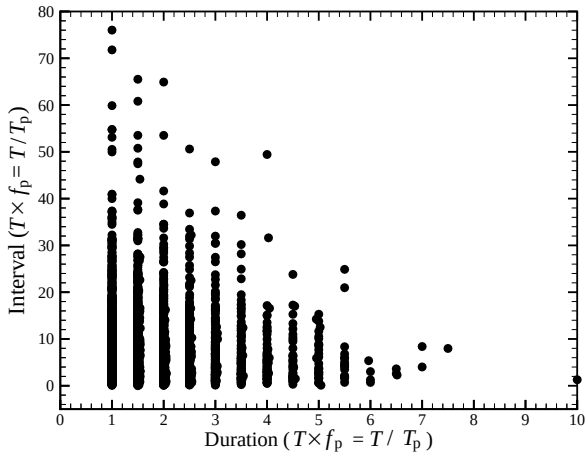

Figure 6.23 Relation between the interval time and duration time.

Chapter 7

Conclusions

In this study, from many turbulent phenomena, mainly three subjects, which can be observed in a turbulent jet and a boundary layer, are focused on and experimentally investigated. They are as follows:

(a) Turbulent/non-turbulent intermittency (Chapters 2 and 3)

(b) Interface between turbulent/non-turbulent region (Chapters 4 and 5)

(c) Large-scale coherent vortex structure (Chapter 6)

The results obtained in this study are summarized in the following.

Chapter 2

In Chapter 2, a new combined probe for measuring instantaneous pressure and two velocity components simultaneously was developed. The combined probe consists of an X-type hot-wire and a newly devised pressure probe. The pressure probe was miniaturized by using a 0.1-inch microphone, and the tip of the pressure probe was shaped into a hemisphere, which is similar to that of the pitot tube. First, we checked the accuracy of the pressure fluctuations in turbulent flows by using the new pressure probe. Then, we carefully examined the effects of the spatial arrangement of the hot-wire probe and the pressure probe on, and investigated the measurement accuracy of the new combined probe in a plane jet. Finally, we estimated the turbulent energy budget and the velocity-pressure cross-correlation coefficient in the intermittent region of the plane jet. The results are summarized as follows.

1. When the newly devised pressure probe was used, the measurement errors of pressure fluctuations were 0 % - 10 % for a uniform flow.

2. No noticeable interference was observed between the signals of the pressure probe and the hot-wire sensor when the lateral distance (cross-streamwise distance) between the hot-wire sensor and the side wall of the pressure probe was set to 0.5 mm and the longitudinal distance (streamwise distance) between the hot-wire sensor and the tip of the pressure probe was set to 2.0 mm. These values correspond to approximately 0.17 times and 0.67 times the Taylor transverse microscale, respectively in the plane jet considered here.

3. The results obtained by using the combined probe and the signal processing system were in good agreement with the reliable results obtained previously. Therefore, we conclude that this newly developed combined probe and the signal processing system were useful for the simultaneous measurements of velocity and pressure.

4. The integral value of the total diffusion term (which should theoretically be equal to zero) was shown to be closer to zero compared with the results reported previously by Bradbury [102]. This is because the proposed combined probe and the signal processing system could measure the pressure diffusion $\overline{vp}$ and the triple correlation $\overline{vw^2}$ more accurately and directly than the probes used in previous studies.

5. The time-variation of the cross-correlation coefficient in the intermittent region supported the vortex structure model suggested from the results of previous studies (Browne et al. [81], Tanaka et al. [104], and Sakai et al. [66]).

Chapter 3

In Chapter 3, by using the combined probe developed in Chapter 2, the simultaneous measurement of velocity and pressure in a plane jet is performed again, and the measured results were discussed from another point of view. Firstly, for more detailed understanding of the flow phenomena in the intermittent region of a plane jet, the conditional ensemble-averaged statistics were investigated on the basis of the intermittency function obtained from the velocity signal by the hot-wire sensor set in the intermittent region of a plane jet. Secondly, the validity of the models for the turbulent and pressure diffusion term such as Daly & Harlow model, Shir model and the model for the rapid/slow term was investigated. The results are summarized as follows.

1. Estimation of the turbulent energy budget based on the turbulent energy transport equation showed that the profiles of the convection term, production term and

diffusion term depended on the flow state in the intermittent region of the jet. When the flow state was turbulent, the convection of the turbulent energy to the inner region of the jet became large, and the region where the turbulent energy producted also became large and extended to the outer region of the jet. Furthermore, the diffusion of the turbulent energy to the outer region of the jet was enhanced.

2. Estimation of the turbulent energy budget based on the turbulent energy transport equation also showed that the profile of the turbulent diffusion term depended on the flow state in the intermittent region, but the pressure diffusion term did not strongly depend on it. Therefore, the dependence of the diffusion process on the flow state was mainly caused by that of the turbulent diffusion process. Further, the pressure diffusion of the turbulent energy to the inner side of the jet observed in the previous studies was not caused by the entrainment/ejection process, which is strongly related to the turbulent intermittency.

3. Daly & Harlow model was adequate for the flow filed where the effect of the pressure diffusion process was weak and the turbulent intermittency was small, while Shir model was adequate for the flow field where the effect of the pressure diffusion process was relatively strong and the turbulent intermittency was small.

4. The pressure diffusion process could not be modeled only by the slow term, and the modeling of the pressure diffusion process by both rapid term and slow term could achieve an improvement of the modeling accuracy.

Chapter 4

In Chapter 4, in order to clarify the structure of the "interfacial layer" between the turbulent and the non-turbulent region, the measurement of velocity and pressure fields near the interface of the turbulent and the non-turbulent region is conducted in a plane jet. The velocity and pressure fields are measured simultaneously using a combined probe comprising an X-type hot-wire and a static pressure tube. The measurement data are analyzed using the conditional sampling technique and an ensemble-averaging technique on the basis of the intermittency function for the turbulent/non-turbulent decision, and the results are discussed. The results are summarized as follows.

1. It is found that there is a thin interfacial layer between the turbulent and the non-turbulent region accompanied by a rapid change in the physical quantities, such as

the streamwise velocity.

2. The thickness of the interfacial layer is 0.08 times the half-widh of the cross-streamwise profile of the mean streamwise velocity and almost the same as Taylor transverse micro scale of the turbulent flow at the measurement location.

3. The velocity and pressure fields near the interfacial layer indicate the existence of vorticities in the middle of the interfacial layer.

4. From the separated estimation of the diffusion term in the transport equation of the turbulent energy, it is found that the turbulent energy is transported from the inner side and the inside of the interfacial layer to the outer non-turbulent region by the pressure diffusion. In addition, this transportation of the turbulent energy is caused by the existence of the interfacial layer.

5. There is a possibility that the existence of the interfacial layer is one of the processes for the transition of the non-turbulent fluid to the turbulent fluid, because the existence of the interfacial layer and the approach of the interfacial layer to the non-turbulent region cause the transportation of turbulent energy to the non-turbulent fluid.

Chapter 5

In Chapter 5, in order to better understand the flow phenomena at the streamwise interfaces between the turbulent and the laminar regions, isolated turbulent regions were periodically generated in a laminar boundary layer by activating a bimorph-type piezoceramic actuator. The results obtained in this study are summarized as follows:

1. Using the piezoceramic actuator, a trapezoidal turbulent region with a large spanwise width could be periodically generated in a boundary layer as intended.

2. The experimental results showed that both the streamwise velocity fluctuations and the intensity of the random component (RMS value of the random component) rapidly changed at the leading end of the turbulent region. On the other hand, the streamwise velocity fluctuations remained high after the intensity of the random component vanishes at the trailing end of the turbulent region.

3. The traveling speed of the trapezoidal turbulent region was almost the same as those of the turbulent spots with an arrow-head shape. Therefore, it was found that

the spanwise interfaces have little influence on the growth of an isolated turbulent region in a laminar boundary layer.

4. From the comparison between the traveling speed of the interface and the local velocity of the same location, it was found that the laminar fluid is entrained into the turbulent region through the interface at the leading interface regardless of the wall-normal position.

5. On the other hand, in the near-wall region with $\eta < 1.3$ at the trailing interface of the turbulent region, it was found that the turbulent fluid was crossing the interface, provoking relaminarization.

6. The critical wall-normal distance of $\eta = 1.3$, which was the limit of the relaminarization process, corresponds to $y^+ = 10.7$ in the wall unit. This result suggests that the relaminarization process was taking place in the viscous sublayer.

Chapter 6

In Chapter 6, the characteristics of the flapping motion are investigated in detail. Firstly, a new method to discriminate the flapping motion and determine the intermittency function about the arising of the flapping motion by using the continuous wavelet transform with Gabor mother wavelet was developed. Secondly, the ensemble-averaged velocity and pressure field on the basis of the intermittency function obtained by the present new method is confirmed. Thirdly, the turbulent energy budget of a plane jet in the flapping motion is estimated. Finally, the interval and the duration of the arising of the flapping motion are estimated. The results are summarized as follows.

1. The new method to extract the flapping motion was developed by using the continuous wavelet transform, and the validity of this new method is confirmed.

2. The phase-averaged pressure field during the flapping motion indicated the existence of a coherent vortex structure, which is interpreted as a combination of flapping and puffing motion in the self-preserving region of the jet.

3. The arising of flapping motion enhances production of the turbulent energy especially in the outer region of the jet and transportation of the turbulent energy to the outer region.

4. Estimation in the transportation of the turbulent energy to the outer region was caused by increase in the transportation of the turbulent energy to the outer region by turbulent diffusion process and decrease in the transportation of the turbulent energy to the inner side by pressure diffusion process.

5. The flapping motion arises at random, and its average interval was about 6.7 times the flapping period.

6. The average duration of a flapping motion was about 1.7 times the flapping period, and the flapping motion that lasts more than 3.0 times the flapping period is very rare.

Acknowledgement

My first thanks goes to Professor Yasuhiko Sakai, who gave me a lot of insights for the physical phenomena and skillful advices to my studies.

I would also like to thank Professor Hiroshi Yamashita, Professor Yoshiaki Nakamura, and Professor Kouji Nagata for joining my thesis committee, participating in the discussions and offering suggestions on my work.

Professor Yu Fukunishi, Professor Seiichiro Izawa (Tohoku University), and Dr. Ayumu Inasawa (Tokyo Metropolitan University) are also acknowledged for the valuable discssuions on a part of my research. I would also like to express my gratitude to Dr. Osamu Suzuki, Dr. Yukinobu Abe, and Mr. Kiyoshi Morita (Hitachi, Ltd.) for helping and encouraging me in the performing of my research. Mr. Yusuke Miki, Mr. Katsuo Kobayashi, Mr. Yuichi Shouji and Mr. Kazuhiro Onishi helped me in conducting my experiments. I would also like to express my thanks to them.

Appendix A

Study on the characteristics of hot-wire anemometer [126]

A constant temperature anemometer (CTA) is a useful instrument for measuring the velocity fluctuations in turbulent flow. The actual frequency response of a typical CTA used in my studies shown in previous chapters is no more than 5 kHz under normal laboratory conditions: for example, the diameter of the hot wire is 5 μm and the free stream velocity is 20 m/s. However, in some cases, a typical CTA is not enough to measure accurately turbulent velocity fluctuations for fine scale structures.

In this Appendix, the details of the design of the CTA and its characteristics are described. Further, a rearranged CTA circuit to obtain a faster frequency response so that in turn fine-scale structures can be more accurately investigated are also shown.

A.1 Introduction

Hot-wire anemometers which use a very thin heated wire as a sensor, are widely used to measure velocity fluctuations in turbulent flows [5]. The advantage of using a hot-wire anemometer is that it has a large dynamic response to the turbulent velocity fluctuation. This large dynamic response is achieved by a very small thermal inertia of hot wire and its compensation by the circuit in the anemometer.

There are several types of hot-wire anemometers which have different operation methods. One of them is a constant temperature anemometer (CTA), which heats up a thin wire and keeps the wire's temperature constant by using a feedback loop in the CTA circuit and automatically compensating for the thermal inertia of the wire. Constant temperature anemometers are widely used to measure velocity fluctuations in turbulent flows because they are easy to handle and they have a higher frequency response to the velocity fluctuations than other types of anemometers. However, the actual frequency

response of a typical CTA is no more than 5 kHz under normal laboratory conditions: for example, the diameter of the hot wire is 5 μm and the free stream velocity is 20 m/s. Therefore, in some cases, a CTA is not accurate enough to correctly measure turbulent velocity fluctuations in fine-scale structures.

To solve this lack of accuracy, we developed, with reference to previous studies [127][128][129], a rearrangement circuit for a CTA that has a faster frequency response than a typical CTA circuit so that fine-scale structures can be better investigated.

A.2 CTA circuit

A.2.1 Typical CTA circuit

An example of a typical CTA circuit is shown in Figure A.1. Hereafter, this circuit is called "Circuit 1." Circuit 1 consists of a Wheatstone bridge circuit and a feedback circuit to compensate for the thermal inertia of the hot wire. The resistance of the thin wire without heating is denoted as R_{w} and the variable resistance is denoted as VR. The bridge resistance ratio R_1/R_2 was set to 10 and the overheat ratio of thin wire was set by adjusting the resistance R_3. The operational amplifier used in the feedback circuit was an OP37 (Analog Devices, Inc.). The gain-bandwidth product of an OP37 is 63 MHz and the slew rate is 17 V/ s.

In Circuit 1, the roll-off frequency ω_0 of the circuit is expressed by Equation (A.1) [3][4].

$$\omega_0^2 \cong \frac{K_0}{M\mu} \tag{A.1}$$

Here, M is the time constant of the hot wire and μ is the time constant of the feedback circuit. In addition, K_0 is expressed by Equation (A.2).

$$K_0 = \frac{2a_{\mathrm{w}}A_0\tilde{R}_{\mathrm{w}}}{\tilde{R}_{\mathrm{w}} + R_1} \tag{A.2}$$

Here, a_{w} is the overheat ratio, A_0 is the amplification factor, $\tilde{R}_{\mathrm{w}}$ is the operating resistance of the hot wire, and R_1 is the resistance in the bridge circuit.

A.2.2 Rearranged CTA circuit

From Equations (A.1) and (A.2) in the previous section, we chose two methods to increase ω_0. One method was to decrease μ by changing the operational amplifier and the other method was to increase K_0 by decreasing the resistance R_1.

Table A.1 Experiment conditions in frequency response test.

Case	CTA circuit	Diameter of the wire (R_w)
1	Circuit 1	5 μm (4.5 Ω)
2	Circuit 2	5 μm (4.5 Ω)
3	Circuit 1	3 μm (7.4 Ω)
4	Circuit 2	3 μm (7.4 Ω)

The rearranged CTA circuit is shown in Figure A.2. Hereafter, this circuit is called "Circuit 2." In Circuit 2, three operational amplifiers are used in the feedback circuit. Two of them were AD797s (Analog Devices, Inc.), which have a gain-bandwidth product of 110 MHz and a slew rate of 20 V/ s. Here, it should be noted that the OP37 in Circuit 2 was used as the final stage amplifier in the feedback circuit to adjust the bridge balance. Further, R_1 was changed from 100 Ω to 10 Ω and the bridge ratio was set to 1.

A.3 Experimental results and discussions

A.3.1 Frequency response test

A frequency response test for Circuit 1 and Circuit 2 was conducted to estimate the roll-off frequency ω_0. The test was conducted at the nozzle exit of a square jet. The size of the nozzle exit of the jet was 80 mm $\times$ 80 mm. The velocity at the nozzle exit was 20 m/s. The estimation was performed by applying a sine-wave heating current to the bridge from the node number 1 in the bridge circuit (see Figures A.1 and A.2) by means of a function-generator. Then, the RMS value of the fluctuating voltage at node 1 (e_1) and that at bridge out (e_0) were measured. In this test, e_1 was set to less than 1 V and the overheat ratio was set at 1.5. Experiment conditions are shown in Table A.1. The length of the hot wire was 1.0 mm in all the experiment conditions.

The results of the frequency response test are shown in Figure A.3. The abscissa shows the frequency of the sine-wave heating current ω and the ordinate shows the relative gain in decibel form RG which is expressed by Equation (A.3) [3][4].

$$RG = \frac{\mid e_0/e_1 \mid}{\mid 1 + j\omega M \mid} \tag{A.3}$$

Here, it should be noted that the time constant M was estimated from the gradient (in actual time scale) of the region where $\mid e_0/e_1 \mid$ increases with the ratio of 20 dB/decade

[3][4]. The meanings of the symbols in Figure A.3 are as follows: $\bigtriangledown$: Case 1, $\bigtriangleup$: Case 2, $\square$: Case 3, and $\bigcirc$: Case 4. Figure A.3 shows that there is a distinct peak at 10 kHz and 14 kHz in Case 1 and Case 3, respectively. It is found that the frequency range where RG equals zero, which means the CTA circuit is accurately responding to the sine-wave heating current, is less than 5 kHz in Case 1 and 6 kHz in Case 3. However, in Case 2 and Case 4, there is no distinct peak and the frequency range where RG equals zero is more than 20 kHz in Case 2 and 40 kHz in Case 4. Therefore, it can be concluded that the frequency response of the CTA can be improved by altering the circuit.

A.3.2 Velocity measurement in a plane jet

Velocity fluctuations in a plane jet were measured using the rearranged CTA circuit. This plane jet was described in previous chapters (See Figure 2.11). The apparatus to create the plane jet consisted of a contraction nozzle, a skimmer, and side walls. The skimmer was placed just after the nozzle exit in order to eliminate the boundary layer, which develops along the wall of the contraction nozzle. The height and width of the skimmer exit were 12 mm and 236 mm, respectively. The velocity U_0 at the skimmer exit was approximately 27.5 m/s and the Reynolds number Re (defined as $U_0 d/\nu$, ν is kinematic viscosity and d is the height of the nozzle exit) was 22,000. Furthermore, the side wall was set vertically in the test section in order to inhibit the entrainment from the side surroundings. By using the skimmer and the side wall, a uniform velocity profile at the skimmer exit and a good two dimensional flow field in the test section was obtained. The coordinate system was as follows: the axial (streamwise) coordinate was x_1, the vertical (cross-streamwise) coordinate was x_2, the spanwise coordinate was x_3, and the origin of the coordinates was set at the center of the nozzle exit.

Figure A.4 shows the power spectrum of streamwise velocity fluctuation at $x_1/d = 20$ and $x_2/b = 1.0$ in Case 1, Case 2, and Case 4. The meanings of ordinate and abscissa are the same as in Figure 2.25. The meanings of the symbols are as follows: $\bigtriangledown$: Case 1, $\bigtriangleup$: Case 2 and $\bigcirc$: Case 4. The long-dashed straight line has a -5/3 slope and the red line indicates the profiles obtained numerically by a LDIA theory which shows an excellent agreement with many measurements of various kinds of real turbulence (See, Kida et al. [130]). Here, it should be noted that the Taylor microscale λ was 3.2 mm and the Tyalor-scale Reynolds number Re_λ was 440 at this measurement point. Figure A.4 shows that the power spectra in Case 2 and Case 4 agree well with the profile by a LDIA theory [130] in the range $\kappa_1 \eta < 0.5$. However, the power spectrum in Case 1 agrees with the profile

by a LDIA theory only in the range $\kappa_1\eta < 0.2$. Therefore, it can be concluded that the high accuracy measurement of velocity fluctuation in a plane turbulent jet is achieved by using the present rearranged CTA circuit.

Velocity fluctuations in a square jet used for the frequency response test mentioned in previous section were measured using the rearranged CTA circuit.

Figure A.5 shows a schematic view of the experimental apparatus and coordinate system of the square jet. The height and width of nozzle exit d was 80 mm. The velocity at the nozzle exit U_0 was 35 m/s and the Reynolds number Re ($= U_0 d/\nu$) was 180,000. The coordinate system was as follows: the axial (streamwise) coordinate was x_1, the vertical (cross-streamwise) coordinate was x_2, the spanwise coordinate was x_3, and the origin of the coordinates was set at the center of the nozzle exit.

Figure A.6 shows the mean streamwise velocity at $x_1/d = 2.0$. The ordinate shows the mean streamwise velocity $\overline{U}$ normalized by $\overline{U_c}$. The abscissa shows x_2/b. Here, b is the half-width of cross-streamwise profile of mean streamwise velocity. Figure A.6 shows that the jet has a potential core at this measurement point.

Figure A.7 shows the RMS value of the streamwise velocity fluctuation at $x_1/d = 2.0$. The ordinate shows u' normalized by u'_c. The abscissa shows x_2/b. Figure A.6 shows that u' has a peak value at $x_2/b = \pm 1.0$.

Figure A.8 shows the power spectrum of streamwise velocity fluctuation at $x_1/d = 2.0$ and $x_2/b = 1.0$ in Case 1, Case 2, and Case 4. The meanings of ordinate and abscissa and the same as in Figure A.4. The meanings of symbols are as follows: $\bigtriangledown$: Case 1, $\bigtriangleup$: Case 2, and $\bigcirc$: Case 4. The long-dashed straight line has -5/3 slope and the red line shows the profile obtained by a LDIA theory [130]. Here, it should be noted that the Taylor microscale λ was 6.3 mm and the Taylor-scale Reynolds number Re_λ was 1,720 at this measurement point. Figure A.8 shows that the power spectrum obeys the profile by the LDIA theory [130] in the range $\kappa_1\eta < 0.08$ (Case 1), $\kappa_1\eta < 0.2$ (Case 2), and $\kappa_1\eta < 0.5$ (Case 4). Further, it can be clearly seen that there is a resonance point at $\kappa_1\eta = 0.3$ (Case 1) and $\kappa_1\eta = 0.5$ (Case 2). Therefore, it is concluded that the frequency response of a CTA can be improved by rearranging the CTA circuit.

A.4 Conclusions

In this appendix, a rearranged CTA circuit is developed. The rearranged CTA circuit has a faster frequency response than a typical CTA circuit. This faster frequency response enables the accurate investigation of fine-scale structures in turbulent flow. The

experimental results are summarized as follows:

1. A rearranged CTA circuit has been proposed. In the circuit, the ratio of the electrical resistance of the Wheatstone bridge is set to 1 and two operational amplifiers, whose gain-bandwidth product and slew rate are 110 MHz and 20 V/ s, respectively, are used in the feedback circuit. The rearranged CTA circuit can respond to velocity fluctuations quickly.

2. The roll-off frequency of the rearranged CTA circuit can be improved from 5 kHz to 20 kHz for a 5 μm hot wire and from 6 kHz to 40 kHz for a 3 μm hot wire when used in a flow with a free stream velocity of 20 m/s.

3. Measurements taken in a plane turbulent jet and square jet using the rearranged CTA circuit show that the power spectrum obeys the reliable numerical profile derived by a LDIA theory over a much wider non-dimensional wave number range in comparison with the results obtained using a typical CTA circuit.

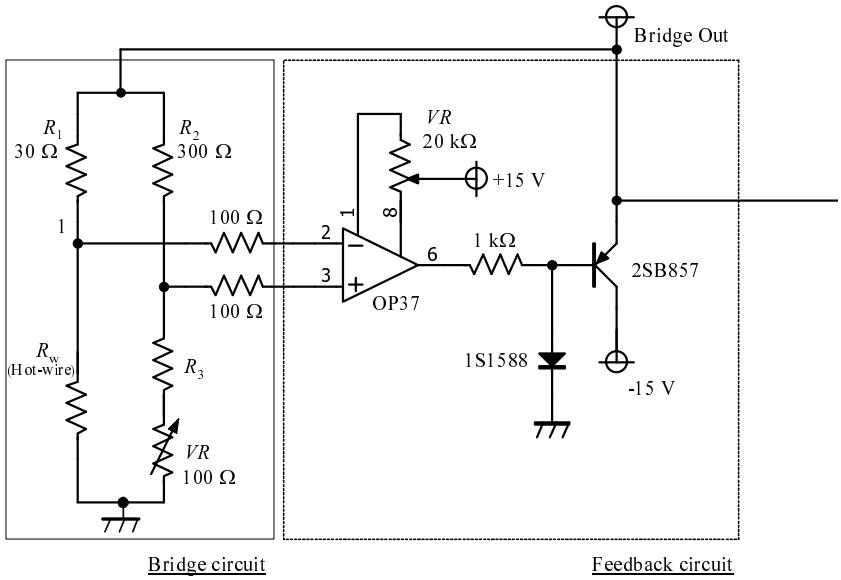

Figure A.1 Block diagram of a typical CTA circuit.

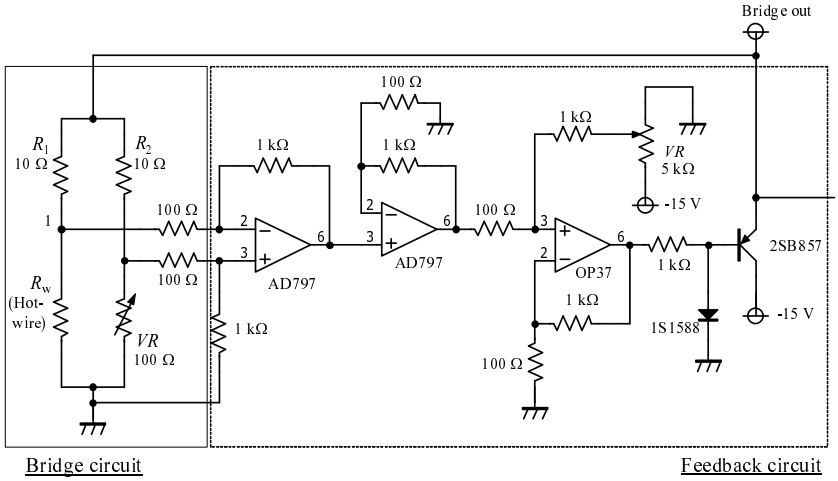

Figure A.2 Block diagram of rearranged CTA circuit.

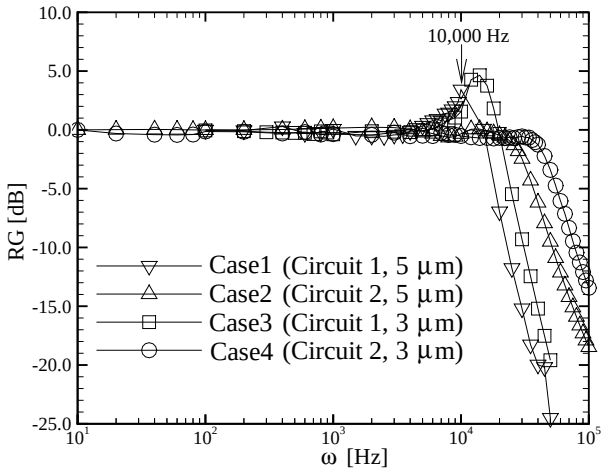

Figure A.3 Results of frequency response test.

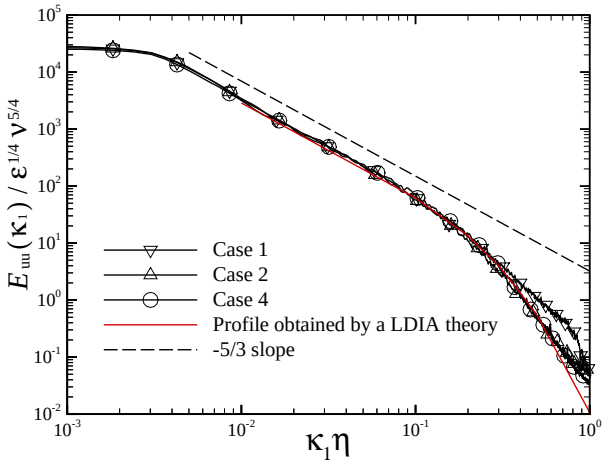

Figure A.4 Power spectra of streamwise velocity fluctuation at $x_1/d = 20$ and $x_2/b = 1.0$.

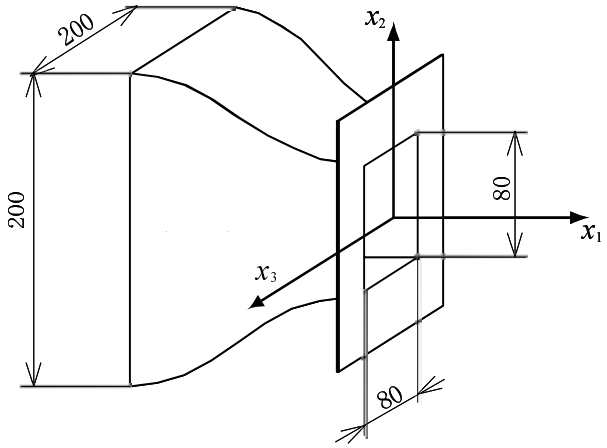

Figure A.5 Schematic view of the apparatus and coordinate system of plane jet.

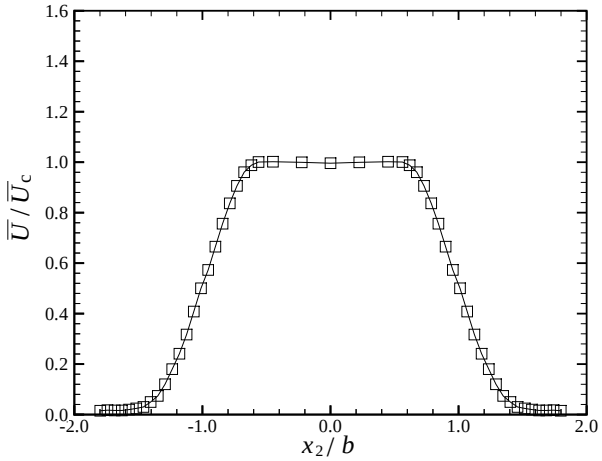

Figure A.6 Cross-streamwise profile of streamwise mean velocity at $x_1/d = 2.0$.

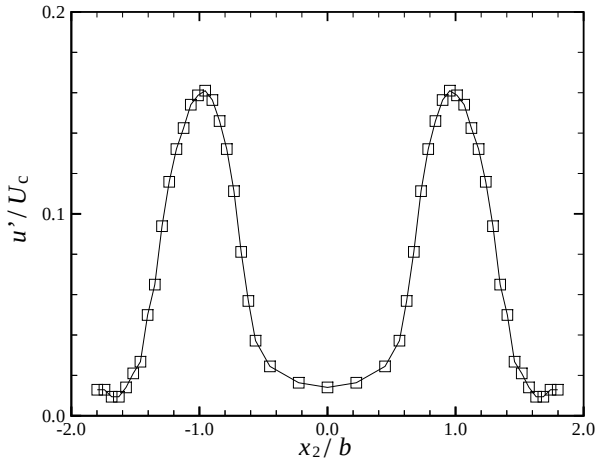

Figure A.7 Cross-streamwise profile of RMS value of streamwise velocity fluctuation at $x_1/d = 2.0$.

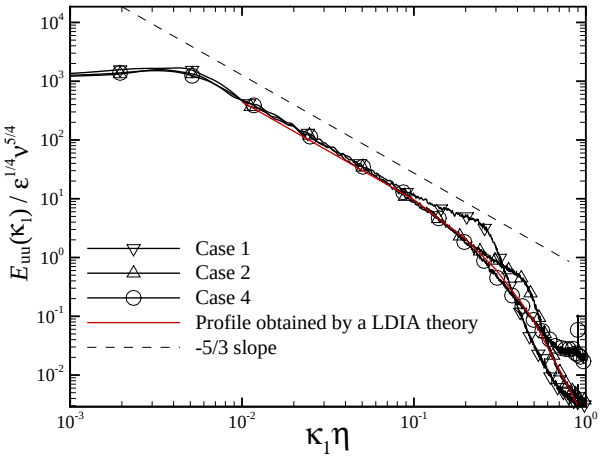

Figure A.8 Power spectra of streamwise velocity fluctuation at $x_1/d = 2.0$ and $x_2/b = 1.0$.

Appendix B

Influence of the cross-flow on the measurement accuracy of pressure probe

In my study described in the previous chapters, the pressure fluctuation in a plane turbulent jet was measured and discussed. However, the pressure probe has a measurement error caused by the cross-flow. Therefore, the estimation of the measurement error caused by cross-flow is important and needed. Based on the background, the measurement error caused by cross-flow is estimated and the results are shown in this appendix.

B.1 Estimation of the measurement error

B.1.1 Estimation based on the time-variation of flow angle

Firstly, the time-variation of flow angle (which determines the cross-flow angle) in present plane jet was investigated and the measurement error was estimated. Experimental apparatus and coordinate system of present plane jet is shown in Figure 2.11. The instantaneous streamwise velocity $U(t)$, cross-streamwise velocity $V(t)$, and spanwise velocity $W(t)$ were measured simultaneously at $x_1/d = 40$ by using two X-type hot-wire probes and one pressure probe shown in Figure B.1. It was confirmed that the measurement error of the probes were little in previous study [131]. Then, the time-variation of flow angle $\phi(t)$ (pitch angle, composed by $U(t)$ and $V(t)$) and $\gamma(t)$ (yaw angle, composed by $U(t)$ and $W(t)$) were estimated.

Figure B.2 shows the cross-streamwise profiles of RMS value of $\phi(t)$ (denoted by ϕ') and $\gamma(t)$ (denoted by γ'). The ordinate shows ϕ' or γ' and the abscissa shows x_2/b. Here, b is the half-width of the cross-streamwise profile of the mean streamwise velocity. The filled

square and filled triangle shows ϕ' and γ', respectively. Figure B.2 indicates that ϕ' is less than 2° and γ' is less than 6° in the range -2.0 < x_2/b < 2.0. Therefore, from Figure 2.7 and 2.8, the measurement error caused by the cross-flow is less than 4 % for the pitch angle ϕ and 8 % for the yaw angle γ. However, as described in Chapter 2, the measurement error caused by the pitch angle $\phi(t)$ is corrected by the instantaneous streamwise velocity U and V measured by X-type hot-wire probe. Therefore, the measurement error caused by the cross-flow is considered to be 8 % in this measurement. Further, by considering the result shown in Figure 2.10 together, the measurement error of the pressure in this experiment is considered to be in the range -8 % - +18 %.

B.1.2 Estimation based on the previous studies

Next, the measurement error caused by the cross-flow was estimated in another point of view based on the previous studies by George et al. [58][132]. In their studies, the measurement error caused by the cross-flow was predicted using the Equation (B.1).

$$[p_{\mathrm{m}} - p] = \rho B \left[\left(v^2 - \overline{v^2} \right) + \left(w^2 - \overline{w^2} \right) \right] \tag{B.1}$$

Here, ρ is the density of fluid, p_{m} is the measured pressure fluctuation by means of pressure probe, p is the true pressure fluctuation (without the pressure probe), v is the cross-streamwise velocity fluctuation, $\overline{v^2}$ is the square of the RMS value of the cross-streamwise velocity fluctuation, w is the spanwise velocity fluctuation, and $\overline{w^2}$ is the square of the RMS value of the spanwise velocity fluctuation. B is the constant determined by the shape and the size of the pressure probe and George et al. showed that this value was -0.15 for their multihole pressure probe [58].

Figure B.3 shows the cross-streamwise profile of RMS value of $[p_{\mathrm{m}} - p]$ denoted by $[p_{\mathrm{m}} - p]$' at $x_1/d = 40$. $[p_{\mathrm{m}} - p]$' is estimated from the RMS value of $\left(v^2 - \overline{v^2} \right) + \left(w^2 - \overline{w^2} \right)$, ρ, and B. Cross-streamwise velocity fluctuation v and spanwise velocity fluctuation w were measured by using the probes shown in Figure B.1. The ordinate is $[p_{\mathrm{m}} - p]$' normalized by the RMS value of the pressure fluctuation on jet center line p_{c}' and the abscissa is x_2/b. In this estimation, B is set equal to -0.15. Figure B.3 indicates that the maximum measurement error is 17 %. Here it should be noted that the constant B is determined by the size of the probe and the present pressure probe (See, Figure 2.1) is much smaller than George's probe. In the present probe, the diameter of the probe was 1/6.35 times and the diameter of the static-pressure hole was approximately 1/5 times of George's probe, respectively. Therefore, in the present probe, the absolute value of B was

considered to be less than 0.15 and the maximum measurement error was less than 17 %.

B.1.3 Estimation based on the predicted value by the inviscid momentum equation

As mentioned in Chapter 2, the measurement error estimated by the ratio of the measured pressure fluctuation and predicted value was in the range 0 - 10 % (See, Figure 2.10). Here, in addition, the measurement error of pressure fluctuation by the pressure probe in the cross-flow was investigated by comparing the predicted value and the measured value when the probe is inclined to the free stream. The measurement apparatus for the experiment is the same as one shown in Figure 2.9. The coordinate system, the origin, and the experiment condition are the same as the experiment shown in section 2.2.2. In this experiment, the pressure probe was installed in the measurement position ($x_1/d_c = 1.80$ and $x_2/d_c = 1.25$, d_c is the diamter of the cylinder) with yaw angles α (0° - 10°) and measured pressure fluctuation. The definition of the yaw angle α was shown in Figure 2.9.

Figure B.4 shows the profiles of p'/p_f' for different yaw angles. The ordinate and abscissa are the same as those in Figure 2.10. The open squares, open triangles, and open downward triangles in Figure B.4 shows the results measured with yaw angle $\alpha = 0°$, 5°, and 10°, respectively. Figure B.4 indicates that the measurement error is in the range $\pm$ 10 % for these yaw angles.

Therefore, from Figures B.2 and B.4, it can be found that there is some measurement error in the measurement of present pressure probe, but it is at most in the range -5 % to +10 %.

B.2 Conclusions

In this appendix, the measurement error of the present pressure probe caused by the cross-flow is estimated by three different ways. The results are summarized as follows:

1. The time-variation of flow angle in the present plane jet and static investigation of the cross-flow error indicated that the measurement error was considered to be 3 %.

2. The estimation of the measurement error with reference to the previous studies showed that the maximum measurement error was less than 17 %.

3. It was found that the measurement error caused by the cross-flow was in the range

-5 % to +10 % from the estimation based on the predicted value by the inviscid momentum equation.

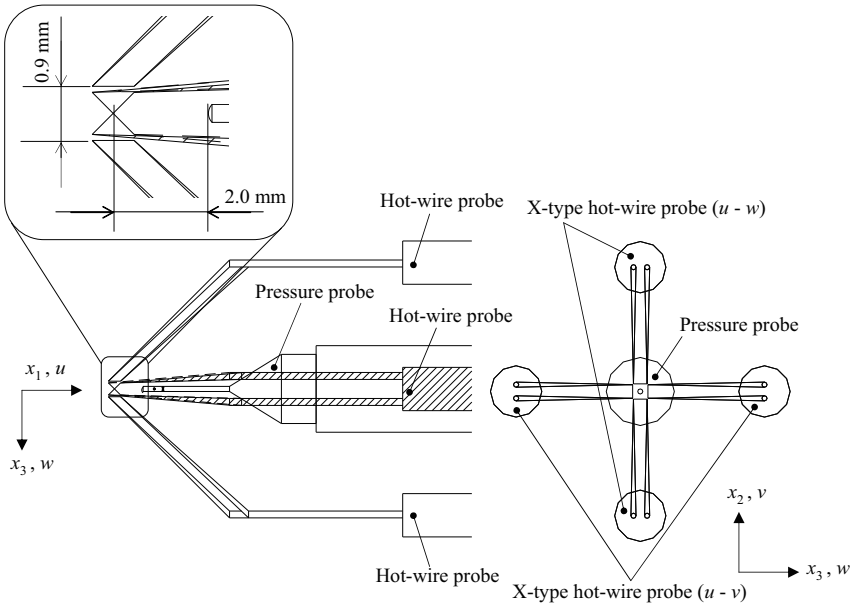

Figure B.1 Schematic view of the probes.

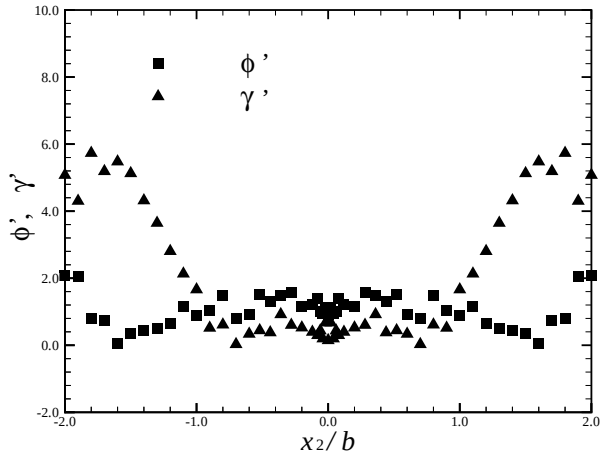

Figure B.2 Cross-streamwise profiles of ϕ' and γ' at $x_1/d = 40$.

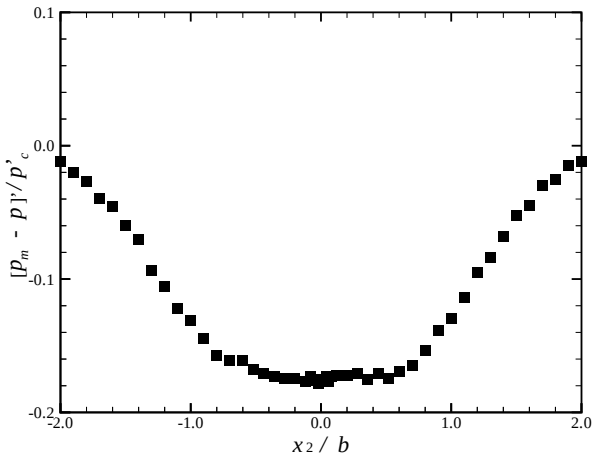

Figure B.3 Cross-streamwise profile of $[p_\mathrm{m} - p]$' at $x_1/d = 40$.

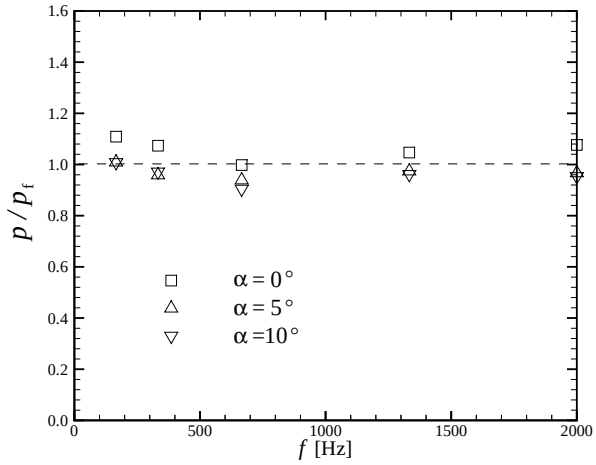

Figure B.4 Ratio of the RMS value of the measured pressure fluctuation p' and that of predicted value p_f' for different yaw angles.

References

[1] EL-G. Mohamd, K. Mori, and Y. Nakamura.
Desensitization of tip clearance effects in axial flow turbines.
Journal of Fluid Science and Technology, Vol. 5, No. 2, pp. 317–330, 2010.

[2] D. Ben, B. Mats, and K. Siniša.
Large eddy simulations of the flow around high-speed trains crusing inside tunnels.
Proceedings of European Congress on Computational Methods in Applied Sciences and Engineering (ECCOMAS 2004), pp. 1–21, 2004.

[3] L.S.G. Kovasznay.
The hot-wire anemometer.
Acta technica Academicae Scientiarum Humgaricae, Vol. 50, pp. 131–151, 1965.

[4] L.S.G. Kovasznay.
In *Applied Mechanics Surveys*, pp. 971–982. Spartan Books, 1966.

[5] C. Geneviève.
In *Experimental Fluid Dynamics*, pp. 229–287. Springer Handbook, 2007.

[6] I.M. Cohen and P.K. Kundu.
In *Fluid Mechanics, Fourth Edition*, pp. 537–611. Academic Press, 2007.

[7] S. Corssin and A.L. Kistler.
Free-stream boundaries of turbulent flows.
NACA TR, No. 1244, pp. 1033–1064, 1955.

[8] S. Komori and H. Ueda.
The large-scale coherent structure in the intermittent region of the self-preserving round free jet.
Journal of Fluid Mechanics, Vol. 152, pp. 337–359, 1985.

[9] A.J. Yule.
Large-scale structure in the mixing layer of a round jet.
Journal of Fluid Mechanics, Vol. 89, pp. 413–432, 1978.

[10] T. Koso and H. Hayami.
Study on the nature of turbulent intermittency in a coflowing turbulent free jet (written in japanese).
The Reports of Institute of Advanced Material Study, Vol. 5, No. 2, pp. 175–188, 1991.

[11] J. Westerweel, T. Hofmann, C. Fukushima, and J.C.R. Hunt.
The turbulent/non turbulent interface at the outer boundary of a self-similar turbulent jet.
Experiments in Fluids, Vol. 33, pp. 873–878, 2002.

[12] D.K. Bisset, J.C.R. Hunt, and M.M. Rogers.
The turbulent/non-turbulent interface bounding a far wake.
Journal of Fluid Mechanics, Vol. 451, pp. 383–410, 2002.

[13] C.B. Silva and J.C.F. Pereira.
Invariants of the velocity-gradient, rate-of-strain, and rate-of-rotation tensors across the turbulent/non turbulent interface in jets.
Physics of Fluids, Vol. 20, pp. 0055101 1–18, 2008.

[14] K. Imaki.
Structure of superlayer in the turbulent boundary layer.
Bulletin of the Institute of Space and Aeronautical Science, University of Tokyo (written in Japanese), Vol. 4, pp. 348–367, 1968.

[15] M. Ichimiya, Y. Nakase, J. Fukutomi, S. Kondou, and I. Tsutsui.
Properties of a turbulence wedge which develops from a single roughness element in a flat plate laminar boundary layer.
Transactions of the Japan Society of Mechanical Engineering, Series B (written in Japanese), Vol. 67, No. 660, pp. 1983–1989, 2001.

[16] A. Inasawa, S. Izawa, A.K. Xiong, and Y. Fukunishi.
Study on the flow structure at the spanwise edge of spreading turbulent region and its control.
Fluid Dynamics Research, Vol. 39, pp. 475–492, 2007.

[17] H.W. Emmons.
The laminar-turbulent transition in a boundary layer.
Journal of Aeronautical Sciences, Vol. 18, pp. 490–498, 1951.

[18] G.B. Schubauer and P.S. Klebanoff.

Contributions on the mechanics of boundary layer transition.
NACA Technical Note, No. 3489, pp. 1–31, 1955.

[19] D. Coles and S.J. Barker.
Some remarks on a synthetic turbulent boundary layer.
Proceedings of the SQUID Work shop, Purdue University, pp. 285–292, 1975.

[20] I. Wygnanski, M. Sokolov, and D. Friedman.
On a turbulent 'spot' in a laminar boundary layer.
Journal of Fluid Mechanics, Vol. 78, pp. 785–819, 1976.

[21] M. Gad-el hak, R.F. Blackwelder, and J.J. Riley.
On the growth of turbulent regions in laminar boundary layer.
Journal of Fluid Mechanics, Vol. 110, pp. 73–95, 1981.

[22] Y. Katz, A. Seifert, and I. Wygnanski.
On the evolution of the turbulent spot in a laminar boundary layer with a favourable pressure gradient.
Journal of Fluid Mechanics, Vol. 221, pp. 1–22, 1981.

[23] A. Seifert and I.J. Wygnanski.
On turbulent spots in a laminar boundary layer subjected to a self-similar adverse pressure gradient.
Journal of Fluid Mechanics, Vol. 296, pp. 185–209, 1995.

[24] E. Gutmark and R.F. Blackwelder.
On the structure of a turbulent spot in a heated laminar boundary layer.
Experiments in Fluids, Vol. 5, pp. 217–229, 1987.

[25] C.R. Smith.
In *Coherent Flow Structures in Open Channels*, pp. 1–39. John Wiley, 1996.

[26] R.A. Antonia, A.J. Chambers, M. Sokolov, and C.W.V. Atta.
Simultaneous temperature and velocity measurements in the plane of symmetry of a transitional turbulent spot.
Experiments in Fluids, Vol. 108, pp. 317–343, 1987.

[27] J.P. Gostelow, G.J. Walker, W.J. Solomon, G. Hong, and N. Melwani.
Investigation of the calmed region behind a turbulent spot.
Journal of Turbomachinery, Vol. 119, No. 4, pp. 802–809, 1997.

[28] T.P. Chong and S. Zhong.

On the momentum and thermal structures of turbulent spots in a favorable pressure gradient.
Journal of Turbomachinery, Vol. 128, pp. 689–698, 2006.

[29] S.N. Brown and F.T. Smith.
Modeling the calmed region behind a spot.
Philosophical Transactions of the Royal Society A, Vol. 363, pp. 1069–1078, 2005.

[30] A. Schröder and J. Kompenhans.
Investigation of a turbulent spot using multi-plain stereo particle image velocimetry.
Experiments in Fluids, Vol. 36, pp. 82–90, 2004.

[31] S.B. Pope.
In *Turbulent flows*, pp. 333–457. CAMBRIDGE University Press, 2000.

[32] B.I. Davidov.
On the statistical dynamics of an incompressible turbulent fluid.
Dokl. Akad. Nauk S.S.S.R., Vol. 136, pp. 47–50, 1961.

[33] F.H. Harlow and P.I. Nakayama.
In *Transport of turbulence energy decay rate*. University of California Report LA-3854, Los Alamos Science Laboratory, 1968.

[34] K. Hanjalić.
In *Two-dimensional Asymmetric Turbulent Flow in Ducts*. Ph.D thesis, University of London, 1970.

[35] B.E. Launder and D.B. Spalding.
In *Mathematical Models of Turbulence*. London: Academic Press, 1972.

[36] W.P. Jones and B.E. Launder.
The prediction of laminarization with a two-equation model turbulence.
International Journal of Heat Mass Transfer, Vol. 15, pp. 301–314, 1972.

[37] B.E. Launder and B.I. Sharma.
Application of the energy-dissipation model of turbulence to the calculation of flow near a spinning disc.
Letter of Heat Mass Transfer, Vol. 11, pp. 131–138, 1974.

[38] Y.F. Yao, F.G. Thomas, N.D. Sandham, and J.J.R. Williams.
Direct numerical simulation of turbulent flow over a rectangular trailing edge.
Theoretical and Computational Fluid Dynamics, Vol. 14, pp. 337–358, 2001.

[39] J.L. Lumley.
Pressure-strain correlation.
Physics of Fluids, Vol. 18, p. 750, 1975.

[40] C.C. Shir.
A preliminary numerical study of atmospheric turbulent flows in the idealized planetary boundary layer.
Journal of the Atmospheric Sciences, Vol. 30, No. 7, pp. 1327–1339, 1973.

[41] P. Bradshaw, D.H. Ferris, and N.P. Atwell.
Calculation of boundary-layer development using the turbulent energy equation.
Journal of Fluid Mechanics, Vol. 28, pp. 593–616, 1967.

[42] B.J. Daly and F.H. Harlow.
Transport equations in turbulence.
Physics of Fluids, Vol. 13, No. 11, pp. 2634–2649, 1970.

[43] C.P. Donaldson.
A computer study of an analytical model of boundary-layer transition.
AIAA Journal, Vol. 7, No. 2, pp. 271–278, 1969.

[44] B.E. Launder.
In *Phenomenological Modelling: Present .... and Future ?*, pp. 439–485. Springer-Verlag, 1989.

[45] J.L. Lumley.
Computational modeling of turbulent flows.
Advances in Applied Mechanics, Vol. 18, pp. 123–176, 1978.

[46] A.O. Demuren, M.M. Rogers, P. Durbin, and S.K. Lele.
In *Studying Turbulence Using Numerical Simulation Databases IV : Proceedings of the 1996 Summer Program*, pp. 63–72. Center for Turbulence Research, Stanford University, 1996.

[47] A.G. Straatman, G.D. Stubley, and G.D. Raithby.
Examination of diffusion modeling using zero-mean-shear turbulence.
AIAA Journal, Vol. 36, No. 6, pp. 929–935, 1998.

[48] A. Yoshizawa.
Statistical analysis of mean-flow effects on the pressure-velocity correlation.
Physics of Fluids, Vol. 14, pp. 1736–1744, 2002.

[49] T. Craft and B.E. Launder.

A reynolds-stress closure designed for complex geometries.
International Journal of Heat and Fluid Flow, Vol. 17, pp. 245–254, 1996.

[50] P. Batten, T.J. Craft, M.A. Leschziner, and H. Loyau.
Reynolds-stress-transport modeling for compressible aerodynamics applications.
AIAA Journal, Vol. 37, pp. 785–797, 1999.

[51] K. Suga.
Modeling the rapid part of the pressure-diffusion process in the reynolds stress transport equation.
ASME Journal of Fluids Engineering, Vol. 126, pp. 634–641, 2004.

[52] Y. Kobashi.
Measurements of pressure fluctuation in the wake of cylinder.
Journal of the Physical Society of Japan, Vol. 12, No. 5, pp. 533–543, 1958.

[53] Y. Kobashi, Y. Kono, and T. Nishi.
Improvement of a pressure pickup for the measurements of turbulence characteristics.
Journal of Aero and Space Science, Vol. 27, pp. 149–151, 1960.

[54] J.A. Elliott.
Microscale pressure fluctuations measured within the lower atmospheric boundary layer.
Journal of Fluid Mechanics, Vol. 53, No. 2, pp. 351–383, 1972.

[55] H.V. Fuchs.
Measurement of pressure fluctuations within subsonic turbulent jets.
Journal of Sound and Vibration, Vol. 22, No. 3, pp. 361–378, 1972.

[56] T.E. Siddon.
On the response of pressure measuring instrumentaion in unsteady flow.
UTIAS Report, 1969.

[57] B.G. Jones, R.J. Adrian, and C.K. Nithianandan.
Spectra of turbulent static pressure fluctuations in jet mixing layers.
AIAA Journal, Vol. 17, No. 5, pp. 449–457, 1979.

[58] W.K. George, P.D. Beuther, and R.E.A. Arndt.
Pressure spectra in turbulent free shear flows.
Journal of Fluid Mechanics, Vol. 148, pp. 155–192, 1984.

[59] K. Toyoda, T. Okamoto, and Y. Shirahama.

Eduction of vortical structures by pressure measurements in noncircular jets.
Applied Scientific Research, Vol. 53, pp. 237–248, 1994.

[60] P. Kupferschmied, P. Köppel, C. Roduner, and G. Gyarmathy.
On the development and application of the fast response aerodynamic probe system in turbomachines part 1:the measurement system.
Journal of Turbomachinery, Vol. 122, pp. 505–516, 2000.

[61] Y. Sakai, T. Kato, Y. Moriguchi, M. Sakai, K. Ito, Y. Mitsuishi, K. Nagata, and T. Kubo.
On static pressure fluctuation between sirocco fan blades in a car air-conditioning system.
Journal of Fluid Science and Technology, Vol. 3, No. 6, pp. 796–804, 2008.

[62] H.S. Ribner.
In *Aerodynamic Sound from Fluid Dilatation*. Institute of Aerophysics Report, University of Tronto, 1962.

[63] H.S. Ribner.
Perspectives on jet noise.
AIAA Journal, Vol. 19, No. 12, pp. 1513–1526, 1985.

[64] Y. Naka, T. Omori, S. Obi, and S. Masuda.
Simultaneous measurements of fluctuating velocity and pressure in a turbulent mixing layer.
International Journal of Heat and Fluid Flow, Vol. 27, pp. 737–746, 2006.

[65] Y. Tsuji, J.H.M. Fransson, P.H. Alfredsson, and A.V. Johansson.
Pressure statistics and their scaling in high-reynolds-number turbulent boundary layers.
Journal of Fluid Mechanics, Vol. 585, pp. 1–40, 2007.

[66] Y. Sakai, Y. Moriguchi, N. Tanaka, M. Yamamoto, T. Kubo, and K. Nagata.
On characteristics of velocity and pressure field in two-dimensional turbulent jet.
Journal of Fluid Science and Technology, Vol. 2, No. 3, pp. 611–622, 2007.

[67] Y. Naka, S. Azegami, T. Kawata, K. Fukagata, and S. Obi.
Simultaneous measurement of velocity and pressure in a wing-tip vortex.
Journal of Fluid Science and Technology, Vol. 4, No. 1, pp. 107–115, 2009.

[68] X. Liu and J. Katz.

Instantaneous pressure and material acceleration measurements using a four-exposure piv system.
Experiments in Fluids, Vol. 41, pp. 227–240, 2006.

[69] S.J. Kline, W.C. Reynolds, F.A. Schraub, and P.W. Runstadler.
The structure of turbulent boundary layers.
Journal of Fluid Mechanics, Vol. 30, No. 4, pp. 741–773, 1967.

[70] I. Wygnanski and H. Fiedler.
Some measurements in the self-preserving jet.
Journal of Fluid Mechanics, Vol. 38, pp. 577–612, 1969.

[71] N. Rajaratnam.
In *Turbulent Jets*. Elsevier Science, 1976.

[72] C.F. Gouldin, R.W. Schefer, Johnson S.C., and W. Kollmann.
Nonreacting turbulent mixing flows.
Progress in Energy and Combustion Science, Vol. 12, pp. 257–303, 1986.

[73] H. Sato.
The stability and transition of a two-dimensional jet.
Journal of Fluid Mechanics, Vol. 7, pp. 53–80, 1960.

[74] D.O. Rockwell and W.O. Niccolls.
Natural breakdown of planar jet.
Transactions of ASME Journal of Basic Engineering, Vol. 94, pp. 720–730, 1972.

[75] F.O. Thomas and V.W. Goldschmidt.
Structural characteristics of a developing turbulent planar jet.
Journal of Fluid Mechanics, Vol. 163, pp. 227–256, 1986.

[76] G.E. Mattingly and W.O. Criminate.
Disturbance characteristics in a plane jet.
Physics of Fluids, Vol. 14, pp. 2258–2264, 1972.

[77] A.K.M.F. Hussain.
Coherent structures and turbulence.
Journal of Fluid Mechanics, Vol. 173, pp. 303–356, 1986.

[78] A.D. Weir, D.H. Wood, and P. Bradshow.
Interacting turbulent shear layers in a plane jet.
Journal of Fluid Mechanics, Vol. 107, No. 2, pp. 237–260, 1981.

[79] R.B. Dean and P. Bradshaw.
Measurements of interacting turbulent shear layers in a duct.
Journal of Fluid Mechanics, Vol. 78, pp. 641–676, 1976.

[80] P. Bradshaw, R.B. Dean, and D.M. McELIGOT.
Calculations of interacting turbulent shear layers.
Transactions of ASME Journal of Fluids Engineering, Vol. 95, pp. 214–220, 1973.

[81] L. W. B. Browne, R. A. Antonia, and A. J. Chambers.
The interaction region of a turbulent plane jet.
Journal of Fluid Mechanics, Vol. 149, pp. 355–373, 1984.

[82] P.E. Dimotakis, R.C. Miake-Lye, and D.A. Papantoniou.
Structure and dynamics of round turbulent jets.
Physics of Fluids, Vol. 26, No. 11, pp. 3185–3192, 1983.

[83] V.W. Goldschmidt and P. Bradshow.
Flapping of a plane jet.
Physics of Fluids, Vol. 16, No. 3, pp. 354–355, 1973.

[84] I. Wygnanski and E. Gutmark.
Lateral motion of the two-dimensional jet boundaries.
Physics of Fluids, Vol. 14, No. 7, pp. 1309–1311, 1971.

[85] K. W. Everitt and A. G. Robins.
The development and structure of turbulent plane jets.
Journal of Fluid Mechanics, Vol. 88, pp. 563–583, 1978.

[86] J. Cervantes de Gortari and V.W. Goldschmidt.
The apparent flapping motion of a turbulent plane jet.
ASME Journal of Fluids Engineering, Vol. 103, No. 1, pp. 119–126, 1981.

[87] J. W. Oler and V. W. Goldschmidt.
A vortex-street model of the flow in the similarity region of a two-dimensional free turbulent plane jet.
Journal of Fluid Mechanics, Vol. 123, pp. 523–535, 1982.

[88] R. A. Antonia, L. W. B. Browne, S. Rajagoplan, and A. J. Chambers.
On the organized structures of a turbulent plane jet.
Journal of Fluid Mechanics, Vol. 134, pp. 49–66, 1983.

[89] J. C. Mumford.

The structure of the large scale eddies in fully developed turbulent shear flows Part 1. the plane jet.
Journal of Fluid Mechanics, Vol. 118, pp. 241–268, 1982.

[90] F.O. Thomas and E.G. Brehob.
An investigation of large-scale structure in the similarity region of a two-dimensional turbulent jet.
Physics of Fluids, Vol. 29, No. 6, pp. 1788–1795, 1986.

[91] S. V. Gordeyev and F. O. Thomas.
Coherent structure in the turbulent planar jet, Part 1. Extraction of proper orthogonal decomposition eigenmodes and their self-similarity.
Journal of Fluid Mechanics, Vol. 414, pp. 145–194, 2000.

[92] Y. Sakai, N. Tanaka, M. Yamamoto, and T. Kushida.
On the development of coherent structure in a plane jet (part 3, multi-point simultaneous measurement of main streamwise velocity).
JSME International Journal Series B, Vol. 49, No. 3, pp. 722–730, 2006.

[93] O. Terashima, Y. Sakai, Y. Shouji, Y. Kojima, K. Nagata, and T. Kubo.
The improvement of the combined probe for the simultaneous measurement of instantaneous static pressure and two velocity components and the estimation of turbulent energy transport in the two-dimensional jet.
Transactions of the Japan Society of Mechanical Engineering, Series B (written in Japanese), Vol. 76, No. 771, pp. 1831–1840, 2010.

[94] O. Terashima, Y. Sakai, Y. Shouji, Y. Kojima, K. Nagata, and T. Kubo.
Development of the innovative probe for the simultaneous measurement of instantaneous pressure and two velocity components.
Proceedings of International Conference on Jets, Wakes and Separated Flows (ICJWSF-2010), 2010.

[95] Y. Shouji, O. Terashima, Y. Sakai, and K. Nagata.
Improvement of the probe for simultaneous measurement of velocity and pressure for high measurement accuracy.
Journal of Japan Society of Experimental Mechanics, Vol. 11, No. 3, pp. 229–234, 2011.

[96] O. Terashima, Y. Sakai, and K. Nagata.
Simultaneous measurement of velocity and pressure in a plane jet.
Experiments in Fluids (DOI 10.1007/s00348-012-1351-z), 2012.

[97] Y. Sakai, K. Nagata, Y. Moriguchi, and T. Kubo.
On the structure of two-dimensional turbulent jet by the simultaneous measurement of instantaneous two velocity components and static pressure : Experimental evaluations of cross-correlation coefficient between velocity and pressure fluctuations and turbulent energy budget(fluids engineering).
Transactions of the Japan Society of Mechanical Engineering, Series B (written in Japanese), Vol. 75, No. 758, pp. 2029–2035, 2009.

[98] Y. Sakai, K. Nagata, Y. Moriguchi, and T. Kubo.
Study on the structure of turbulent plane jet by the simultaneous measurement of instantaneous two velocity components and static pressure.
Proceedings of International Conference on Jets, Wakes and Separated Flows (ICJWSF-2010), 2010.

[99] A.A. Townsend.
The fully developed turbulent wake of a circular cylinder.
Australian Journal of Scientific Research, Sereies A : Physical Sciences, Vol. 2, pp. 451–468, 1949.

[100] Y. Sakai, N. Tanaka, M. Yamamoto, and T. Kushida.
On the development of coherent structure in a plane jet (part 1, characteristics of two-point velocity correlation and analysis of eigenmodes by the kl expansion).
JSME International Journal Series B, Vol. 49, No. 1, pp. 115–124, 2006.

[101] G. Heskestad.
Hot-wire measurements in a plane turbulent jet.
Transactions of the ASME series E (Journal of applied mechanics), Vol. 32, No. 4, pp. 721–734, 1965.

[102] L. J. S. Bradbury.
The structure of a self-preserving turbulent plane jet.
Journal of Fluid Mechanics, Vol. 23, pp. 31–64, 1965.

[103] T.B. Hedley and J.F. Keffer.
Turbulent/non-turbulent decisions in an intermittent flow.
Journal of Fluid Mechanics, Vol. 64, pp. 625–644, 1974.

[104] N. Tanaka, Y. Sakai, M. Yamamoto, and T. Kubo.
On the development of coherent structure in a plane jet (part 4, the multipoint simultaneous measurement of two-component velocities and the simple coherent structure model).

JSME International Journal Series B, Vol. 49, No. 4, pp. 899–905, 2006.

[105] O. Terashima, Y. Sakai, and K. Nagata.
Simultaneous measurement of the velocity and pressure in a plane jet (estimation of conditional averaged value and diffusion term in the intermittent region).
Transactions of the Japan Society of Mechanical Engineering, Series B (written in Japanese), Vol. 78, No. 787, pp. 541–552, 2011.

[106] J. Rotta.
Statistische theorie nichthomogener turbulenz.
Zeitschrift für Physik A Hadrons and Nuclei, Vol. 129, No. 6, pp. 547–572, 1951.

[107] J. Rotta.
Statistische theorie nichthomogener turbulenz.
Zeitschrift für Physik A Hadrons and Nuclei, Vol. 131, No. 1, pp. 51–77, 1951.

[108] O. Terashima, Y. Sakai, K. Nagata, Y. Shouji, and K. Onishi.
Study on the interfacial layer between the turbulent/non-turbulent region in a two-dimensional turbulent jet.
Transactions of the Japan Society of Mechanical Engineering, Series B (written in Japanese), Vol. 78, No. 790, pp. 1235–1247, 2011.

[109] O. Terashima, Y. Sakai, and K. Nagata.
Study on the interfacial layers between the turbulent/non turbulent regions in two dimensional turbulent jet.
Proceedings of ASME - JSME - KSME Joint Fluids Engineering Conference (AJK-2011), No. 21003, 2011.

[110] O. Terashima, S. Izawa, A. Inasawa, and Y. Fukunishi.
Streamwise interface of an isolated turbulent region in a laminar flat-plate boundary layer.
Transactions of the Japan Society of Mechanical Engineering, Series B (written in Japanese), Vol. 77, No. 773, pp. 56–65, 2011.

[111] O. Terashima, S. Izawa, A. Inasawa, and Y. Fukunishi.
Study on the interfaces of an isolated turbu-lent region in a laminar boundary layer.
Proceedings of Thermal and Fluid Engineering Conference 8 (TFEC-8), 2012.

[112] O. Terashima, S. Izawa, A. Inasawa, and Y. Fukunishi.
Streamwise interfaces of an isolated turbulent region in a laminar boundary layer.
Journal of Fluid Science and Technology, Vol. 7, No. 1, pp. 129–144, 2012.

[113] O. Terashima, Y. Miki, S. Izawa, M. Shigeta, and Y. Fukunishi.
Study on laminar/turbulent streamwise interfaces in a boundary layer flow.
JAXA Special Publication, pp. 73–76, 2007.

[114] Y. Fukunishi, S. Izawa, and K. Morita.
Development of a new device to control oblique waves in transitional boundary layers.
Fluid Dynamics Research, Vol. 36, pp. 9–22, 2005.

[115] Zilberman M. Wygnanski, I. and J.H. Haritonidis.
On the spreading of a turbulent spot in the absence of a pressure gradient.
Journal of Fluid Mechanics, Vol. 123, pp. 69–90, 1982.

[116] T.P. Chong and S. Zhong.
On the three-dimensional structure of turbulent spots.
Journal of Turbomachinery, Vol. 127, pp. 545–551, 2005.

[117] Matsubara M. Fransson, J.H.M. and P.H. Alfredsson.
Transition induced by free-stream turbulence.
Journal of Fluid Mechanics, Vol. 527, pp. 1–25, 2005.

[118] S. Zhong, C. Kittichaikan, H.P. Hodson, and P.T. Ireland.
Visualization of turbulent spots under the influence of adverse pressure gradients.
Experiments in Fluids, Vol. 28, pp. 385–393, 2000.

[119] O. Terashima, Y. Sakai, and K. Nagata.
Characteristics of two-dimensional turbulent jet in flapping motion.
Transactions of the Japan Society of Mechanical Engineering, Series B (written in Japanese), Vol. 78, No. 787, pp. 553–565, 2012.

[120] O. Terashima, Y. Sakai, K. Nagata, and Y. Shouji.
Ths statistical evaluation of the flapping motion in a two-dimensional turbulent jet.
Transactions of the Japan Society of Mechanical Engineering, Series B (written in Japanese), Vol. 77, No. 775, pp. 446–455, 2011.

[121] O. Terashima, Y. Sakai, and K. Nagata.
The statistical analysis of flapping phenomenon in a two-dimensional turbulent jet.
Proceedings of the 7th Turbulence and Shear Flow Phenomena, No. 236000, 2011.

[122] Y. Shouji, O. Terashima, Y. Sakai, and K. Nagata.
Effect of pressure fluctuation at nozzle exit on flapping phenomena in a two-dimensional jet.

Proceedings of ASME-JSME-KSME Joint Fluids Engineering Conference 2011 (AJK-2011), No. 16034, 2011.

[123] N. Tanaka, Y. Sakai, and M. Yamamoto.
A study on the vortex structure and estimation of its convective velocity in a turbulent plane jet.
Proceedings of Annual Conference of Japan Society of Mechanical Engineering (writen in Japanese), Vol. 4, No. 1, pp. 497–498, 2004.

[124] Bradshaw. P. and Y.M. Koh.
A note on poisson's equation for pressure in a turbulent flow.
Physics of fluids, Vol. 24, p. 777, 1981.

[125] Y. Shirahama and K. Toyoda.
Development of the probe to measure static-pressure fluctuations : Application to the measurements of jets.
Transactions of the Japan Society of Mechanical Engineering, Series B (written in Japanese), Vol. 59, No. 567, pp. 3381–3387, 1993.

[126] O. Terashima, K. Onishi, Y. Sakai, K. Nagata, and S. Takagi.
Study on the improvement of frequency response of the constant temperature anemometer.
Transactions of the Japan Society of Mechanical Engineering, Series B (written in Japanese), Vol. 78, No. 788, pp. 862–866, 2012.

[127] N.B. Wood.
A method for determination and control of the frequency response of the constant-temperature hot-wire anemometer.
Journal of Fluid Mechanics, Vol. 67, No. 4, pp. 769–786, 1975.

[128] P. Freymuth.
On higher order dynamics of constant constant-temperature hot-wire anemometers.
Measurement Science and Technology, Vol. 9, pp. 534–535, 1997.

[129] J.H. Watmuff.
An investigation of the constant-temperature hot-wire anemometer.
Experimental Thermal and Fluid Science, Vol. 11, pp. 117–134, 1995.

[130] S. Kida and S. Goto.
A lagrangian direct-interaction approximation for homogeneous isotropic turbulence.

Journal of Fluid Mechanics, Vol. 345, pp. 307–345, 1997.

[131] K. Onishi, O. Terashima, Y. Sakai, and K. Nagata.
The development of extremely-compact static pressure probe for the simultaneous measurement of pressure and velocity in turbulent flows.
Proceedings of ASME - JSME - KSME joint fluids Engineering Conference (AJK-2011), No. 31001, 2011.

[132] H.J. Hussein, S.P. Capp, and W.K. George.
Velocity measurements in a high-reynolds-number, momentum-conserving, axisymmetric, turbulent jet.
Journal of Fluid Mechanics, Vol. 258, pp. 31–75, 1994.